

INTERACTION OF A SYNTHETIC JET WITH A FLAT PLATE BOUNDARY  
LAYER



By

PRAKIT RAMPUNGGOON

A DISSERTATION PRESENTED TO THE GRADUATE SCHOOL  
OF THE UNIVERSITY OF FLORIDA IN PARTIAL FULFILLMENT  
OF THE REQUIREMENTS FOR THE DEGREE OF  
DOCTOR OF PHILOSOPHY

UNIVERSITY OF FLORIDA

2001

Copyright 2001

by

Prakit Rampungoon

## ACKNOWLEDGMENTS

I would like to acknowledge the Royal Thai Navy for the complete financial support of my graduate study. I would like to thank my advisor Dr. Rajat Mittal for giving me the opportunity to work under his supervision, for being a good teacher and for helping me throughout my study. I would like to thank Dr. William E. Lear, Dr. Zhuomin Zhang, Dr. Renwei Mei and Dr. Lou Cattafesta III for serving as my committee members, for giving me the opportunity to present my work and for giving me very useful feedback on my research. Finally, I would also like to thank Dr. Udaykumar at the University of Iowa for allowing me to use his FORTRAN code in my study and for always being available to me when I needed advice about the code.

## TABLE OF CONTENTS

	<u>page</u>
ACKNOWLEDGMENTS.....	iii
LIST OF TABLES .....	vi
LIST OF FIGURES.....	vii
NOMENCLATURE.....	x
ABSTRACT .....	xii
1 INTRODUCTION.....	1
1.1 Motivation .....	1
1.2 Overview of Synthetic Jet Actuators.....	3
1.3 Literature Survey.....	4
1.3.1 Characterization of Synthetic Jets.....	8
1.3.2 Application of Synthetic Jets to Separation Control .....	11
1.3.3 Numerical Studies of Synthetic Jets.....	14
1.3.4 Other Applications of Synthetic Jets.....	18
2 OBJECTIVES AND APPROACH .....	20
2.1 Parameter Study .....	20
2.1.1 Flow Configuration .....	20
2.1.2 Jet Characterization and Scaling .....	21
2.1.3 Effect of the Jet on the External Flow: Characterization and Scaling .....	24
3 NUMERICAL METHOD .....	28
3.1 Governing Equations and Flow Configuration .....	29
3.2 Flow Solver with Stationary Immersed Boundaries .....	30
3.3 Flow Solver with Moving Immersed Boundaries .....	36
3.4 Freshly-Cleared Cells.....	41
3.5 Fast Solution of Discretized Equations .....	43
3.6 Overall Solution Procedure .....	45
3.7 Validation of the Solver .....	46



4 RESULTS.....	52
4.1 Computational Aspect.....	52
4.2 Vortex Dynamics.....	56
4.2.1 Quiescent External Flow Cases.....	56
4.2.1.1 Effect of jet Reynolds number .....	56
4.2.1.2 Effect of $h/d$ .....	63
4.2.2 External Crossflow Cases.....	66
4.2.2.1 Effect of jet Reynolds number .....	66
4.2.2.2 Effect of $h/d$ .....	69
4.2.2.3 Effect of crossflow Reynolds number .....	70
5 VELOCITY PROFILES: COMPARISON AND ANALYSIS.....	75
5.1. Comparison of Jet Velocity Profiles .....	75
5.1.1 Quiescent External Flow Cases.....	76
5.1.1.1 Effect of jet Reynolds number .....	76
5.1.1.2 Effect of $h/d$ .....	77
5.1.2. External Crossflow Cases .....	79
5.1.2.1 Effect of jet Reynolds number .....	79
5.1.2.2 Effect of $h/d$ .....	80
5.1.2.3 Effect of crossflow Reynolds number .....	81
5.2 Integral Measures of the Jet .....	83
5.2.1 Jet Momentum Coefficients .....	83
5.2.1.1 Quiescent external flow cases .....	83
5.2.1.2 External crossflow cases .....	85
5.2.2 Energy Flux.....	87
5.2.2.1 Quiescent external flow cases .....	87
5.2.2.2 External crossflow cases .....	87
5.2.3 Skewness Coefficient.....	89
5.3 Modeling of Jet Velocity Profiles .....	91
5.3.1 Candidate Jet Profile .....	93
5.3.2 Comparison of Actual and Modeled Profile .....	95
5.3.2.1 Quiescent external flow cases .....	95
5.3.2.2 External crossflow cases .....	97
6 VIRTUAL AERO-SHAPING EFFECT .....	101
6.1 Effect of Variation in Crossflow Velocity .....	102
6.2 Effect of Variation in Jet Velocity .....	103
6.3 Scaling of the Bubble Size with Flow Parameters .....	105
7 CONCLUSIONS .....	108
LIST OF REFERENCES .....	110
BIOGRAPHICAL SKETCH .....	115

## LIST OF TABLES

<u>Table</u>	<u>Page</u>
1. Simulations and parameters in the current study.....	55
2. Maximum jet velocity, momentum coefficient, skewness, $A$ , $B$ and $m$ . ....	95

## LIST OF FIGURES

<u>Figure</u>	<u>Page</u>
1. Synthetic jet actuators .....	3
2. Synthetic jet actuator with the rectangular chamber and slot simplified to the 2-D model in the current study. ....	4
3. Top view of the experiment setup by James et al.....	8
4. Experimental setup of Smith et al. ....	11
5. Airfoil used in the experiment of Smith et al. ....	12
6. Synthetic jet actuators configuration in the study by Lee & Goldstein. ....	17
7. 2-D synthetic jet configuration used in the current study.....	20
8. Moving boundary cutting through a fixed mesh. ....	30
9. Stencils for evaluation of cell face fluxes.. ....	34
10. Change of material as the immersed boundary traverses the mesh.....	42
11. Nonuniform mesh used in the oscillating cylinder simulations. ....	47
12. Contour plot of spanwise vorticity showing the shedding of vortices for a fixed cylinder. ....	48
13. Comparison of the result from the current study and the result from other studies.. ....	49
14. Series of the vorticity contour plots for a lock-on case.....	50
15. Contour plot of spanwise vorticity showing the shedding of three vortices per shedding cycle.. ....	51
16. Computation domain and boundary conditions.....	52
17. Fixed nonuniform Cartesian grid used in the synthetic jet calculation. ....	53
18. Vorticity contour plots for quiescent external flow, $h/d = 1$ and $Re_d = 63$ .....	57

19. Vorticity contour plots for quiescent external flow, $h/d = 1$ and $Re_d = 125$ .....	59
20. Vorticity contour plots for quiescent external flow, $h/d = 1$ and $Re_d = 187$ .....	60
21. Vorticity contour plots for quiescent external flow, $h/d = 1$ and $Re_d = 250$ .....	61
22. Vorticity contour plots for quiescent external flow, $h/d = 1/3$ and $Re_d = 250$ .....	63
23. Vorticity contour plots for quiescent external flow, $h/d = 3$ and $Re_d = 250$ .....	64
24. Vorticity contour plots for quiescent external flow, $h/d = 5$ and $Re_d = 250$ .....	65
25. Vorticity contour plots for $Re_\delta = 254$ , $h/d = 1$ and $Re_d = 63$ .....	66
26. Vorticity contour plots for $Re_\delta = 254$ , $h/d = 1$ and $Re_d = 125$ . ....	67
27. Vorticity contour plots for $Re_\delta = 254$ , $h/d = 1$ and $Re_d = 187$ .....	68
28. Vorticity contour plots for $Re_\delta = 254$ , $h/d = 1$ and $Re_d = 250$ .....	69
29. Vorticity contour plots for $Re_\delta = 254$ , $h/d = 3$ and $Re_d = 250$ .....	70
30. Vorticity contour plots for $Re_\delta = 400$ , $h/d = 1$ and $Re_d = 250$ .....	71
31. Vorticity contour plots for $Re_\delta = 800$ , $h/d = 1$ and $Re_d = 250$ .....	72
32. Vorticity contour plots for $Re_\delta = 1200$ , $h/d = 1$ and $Re_d = 250$ .....	73
33. Series of the vorticity contour plots for $Re_\delta = 1200$ , $h/d = 1$ and $Re_d = 250$ . ....	73
34. Vorticity contour plots for $Re_\delta = 2600$ , $h/d = 1$ and $Re_d = 250$ .....	74
35. Probe location line along which velocity profiles were extracted.....	75
36. Velocity profiles for quiescent external flow cases with $h/d = 1$ .....	77
37. Velocity profiles for quiescent external flow cases with $Re_d = 250$ . ....	78
38. Velocity profiles for boundary-layer cases with $h/d = 1$ and $Re_\delta = 254$ .. ....	80
39. Velocity profiles for boundary-layer cases with $Re_d = 250$ .. ....	82
40. Velocity profiles for boundary-layer cases with $Re_d = 250$ and $h/d = 1$ . ....	83



41. Momentum coefficient for quiescent external flow cases.....	85
42. Momentum coefficient for boundary-layer cases.....	87
43. Energy flux coefficient for quiescent external flow cases.....	89
44. Energy flux coefficient for boundary-layer cases.....	90
45. Skewness coefficient versus $Re_\delta$ for $Re_d = 63$ and $250$ .....	91
46. Velocity profiles for boundary-layer cases with $Re_d = 63$ and $h/d = 1$ . ....	92
47. Comparison of actual and modeled profiles with $h/d = 1$ . ....	97
48. Comparison of actual and modeled profiles with $Re_d = 250$ .....	98
49. Comparison of actual and modeled profiles for $h/d = 1$ , $\delta / d = 2$ , $Re_\delta = 254$ .....	99
50. Comparison of actual and modeled profiles for $h/d = 1$ , $\delta / d = 2$ , $Re_d = 250$ .....	100
51. Streamline of the mean flow with $\delta / d = 2$ and $Re_d = 250$ . ....	104
52. Streamline of the mean flow with $\delta / d = 2$ and $Re_\delta = 254$ . ....	105
53. Streamline of the mean flow with $\delta / d = 5$ and $Re_\delta = 254$ .....	106
54. Log scale plot of the ratio $L_r / \delta$ with the ratio $V_{ave}^{inv} d / U_\infty \delta$ .....	107
55. Log scale plot of the ratio $L_r / d$ with the ratio $(V_{ave}^{inv})^2 d / U_\infty^2 \delta$ .....	108

## NOMENCLATURE

$A$	=	Deflection amplitude of the diaphragm
$C_{\phi_{12}}^n$	=	$n^{th}$ moment of the jet over the phase interval from $\phi_1$ to $\phi_2$
$H$	=	Cavity height
$L$	=	Length scale
$L_r$	=	Size of the recirculation bubble
$F^+$	=	Non-dimension forcing frequency
$Re$	=	$\frac{U_0 L}{\nu}$ , Reynolds number
$Re_d$	=	$\frac{V_{ave}^{inv} d}{\nu}$ , Jet Reynolds number
$Re_\delta$	=	$\frac{U_\infty \delta}{\nu}$ , Boundary layer thickness Reynolds number
$V_{ave}^{inv}$	=	Mean jet velocity for the expulsion phase
$V_{max}^{inv}$	=	Maximum jet velocity for the expulsion phase
$U_0$	=	Velocity scale
$U_\infty$	=	Freestream velocity
$S$	=	$\sqrt{\frac{\omega d^2}{\nu}}$ , Stokes number

$St$	$=$	$\frac{\omega L}{U_0}$ , Strouhal number
$W$	$=$	Actuator cavity width
$X_{\phi_{12}}$	$=$	Skewness of the velocity profile over the phase interval from $\phi_1$ to $\phi_2$
$d$	$=$	Slot width
$f, f_f$	$=$	Forcing frequency
$f_0$	$=$	Natural vortex shedding frequency
$f_v$	$=$	Vortex shedding frequency
$h$	$=$	Slot height
$l_s$	$=$	Characteristic length of a separation region
$u$	$=$	Velocity component in the x-direction
$v$	$=$	Velocity component in the y-direction
$y_L$	$=$	Entrance length
$\delta$	$=$	Boundary layer thickness
$\delta^*$	$=$	Displacement thickness
$\theta$	$=$	Momentum thickness
$\rho$	$=$	Fluid density
$\nu$	$=$	Fluid kinematic viscosity
$\omega$	$=$	Angular frequency

Abstract of Dissertation Presented to the Graduate School  
of the University of Florida in Partial Fulfillment of the  
Requirements for the Degree of Doctor of Philosophy

INTERACTION OF A SYNTHETIC JET WITH A FLAT PLATE BOUNDARY  
LAYER

By

Prakit Rampunggoon

December 2001

Chairman: Dr. Rajat Mittal

Major Department: Mechanical Engineering

The interaction of a 2-dimensional modeled synthetic jet with a flat plate boundary layer is investigated numerically using an incompressible Navier-Stokes solver. A simple, two-dimensional synthetic jet configuration along with a flat plate, laminar Blasius boundary layer was used in the current study. The oscillating diaphragm of the actuator is modeled in a realistic manner as a moving boundary in an effort to accurately compute the flow inside the jet cavity. The primary focus of the current study is on describing the dynamics of the synthetic jet in the presence of external crossflow. However, in addition, simulations of the jet with quiescent external flow have also been performed. A systematic framework was put forth for characterizing the jet that consists of computing the various moments of the velocity profile along with an integral measure of the profile skewness. A comprehensive parametric study has been carried out where the diaphragm amplitude, external flow Reynolds number, boundary layer thickness, and slot dimensions are varied; and the scaling of the jet characteristics with parameters is



examined. The simulations also allow us to extract some interesting flow physics associated with the vortex dynamics of the jet and to elucidate the effect of external cross flow on jet development. In addition, a low-dimensional model for jet velocity profile is proposed and tested. Finally, the so-called “virtual aero-shaping” effect of synthetic jets is examined and the current simulations indicate a simple scaling of this effect with the dynamical characteristics of the jet and external crossflow.

## CHAPTER 1 INTRODUCTION

### 1.1 Motivation

Techniques that attempt to delay flow separation over wings have been extensively explored in the past. Flow separation can be delayed using passive or active control techniques or both (Gad-el-Hak & Bushnell 1991, Smith 1998). Passive flow control is usually accomplished through proper design of the system and does not require any energy input. However, this form of control is very rigid and not capable of adjusting to instantaneous flow conditions. On the other hand, active flow control is generally used when systems have to operate in off-design conditions or when passive control technique cannot be used due to certain design limits. Furthermore, active control is amenable to on-the-fly adjustments and is therefore capable of providing control over a larger portion of the flight envelope. However, active control devices usually add complexity in design, add cost to the manufacturing process and need power to operate. These factors sometimes prevent the use of active control. For this reason, many researchers have focused on designing better active flow control devices that are easy to manufacture, small in size and require little power to operate.

The advent of MEMS (Micro Electro-Mechanical Systems) technology (Ho & Tai 1996) in the last two decades has provided a new impetus to the field of active control. The MEMS based actuators are easy to mass manufacture; and they provide a unified framework for implementing flow control including actuation, power transmission,

sensing and incorporation of control algorithms. In this context, the synthetic jet has emerged as one of the most useful micro (or meso) fluidic devices with the potential application ranging from thrust vectoring of jet engines (Smith et al. 1997), mixing enhancement (Chen et al. 1999, Davis et al. 1999) to active control of separation and turbulence in boundary layers (Smith et al. 1998, Crook et al. 1999). However, the utility of these devices for controlling flows has mostly been shown in laboratory setups. Many issues must be addressed to transition this technology to practical applications. First, the performance characteristics of a synthetic jet actuator depend on a number of geometrical, structural and flow parameters and little understanding exists as to how performance characteristics scale with these parameters. Secondly, although experiments have shown that for instance, synthetic jets can be used to delay separation (Amitay et al. 1997), our understanding of the physical mechanisms that lead to this effect is quite limited. Both of these issues can be addressed by a systematic parameter study of synthetic jets, and this forms the main objective of the current study.

Although experimental investigations are capable of providing good insight into how a synthetic jet affects the external flow, most experimental studies do not provide a clear picture of the flow behavior inside the cavity of an actuator. However, understanding this behavior is important in the proper design of an actuator because internal cavity flow could severely affect jet performance. Furthermore, a parameter study of this flow configuration through experiment is an expensive proposition. For both of these reasons, analysis through numerical simulation is an attractive alternative and is the approach used in this study.



## 1.2 Overview of Synthetic Jet Actuators

A synthetic jet actuator is a device used to produce an oscillatory jet of fluid. The jet is called a “synthetic” jet because it is synthesized from the external fluid, without net

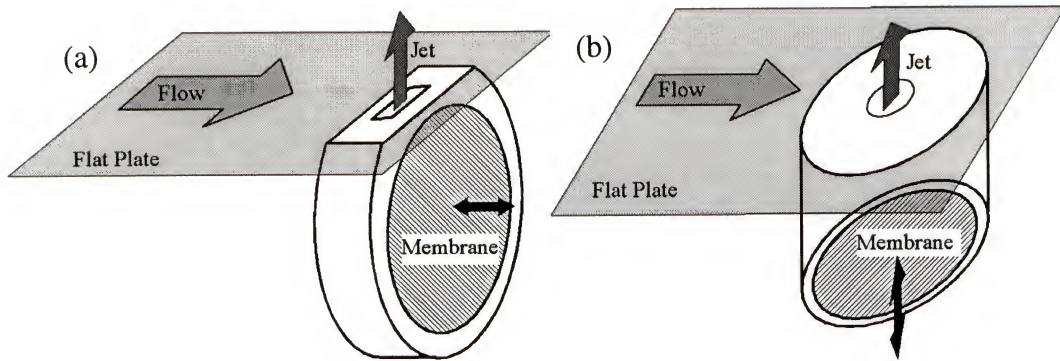


Figure 1. Synthetic jet actuators. a) Rectangular orifice type; b) Circular chamber and orifice type.

mass addition. This is one attractive feature of these devices since no hardware is required to pipe flow from a separate source. There are a number of different designs of synthetic jet actuators but they all share the concept of operating with zero net mass flux. Two typical configurations of these actuators are shown in Figure 1. Consider the actuator in Figure 1(a), this actuator comprises a cavity with the small slot (or orifice) at the top surface. The side of the cavity is an oscillating diaphragm, which is usually driven near its resonant frequency by electrical or mechanical power. Because the diaphragm is usually operated near its resonant frequency, only a small amount of energy is needed to operate the device. To install the device, for example in the case of control of flow over an airfoil, the top part of the actuator is flush mounted underneath the top surface of the airfoil so that its orifice is open to the external fluid (Seifert et al. 1998a). When the diaphragm moves out, it ingests external fluid into the cavity. When the diaphragm moves in, it expels fluid out of the cavity through the orifice. In the case

where there is no external flow, this creates a pair of counter-rotating vortices. This pair of vortices is removed from the surface by its own momentum before the diaphragm moves out to entrain the ambient fluid into the cavity. This way the actuator can generate periodic excitation to the flow without net mass addition. These actuators can be designed to have different shape. Two examples of actuators are shown in Figure 1.

Also, different types of jet exit shapes are possible. The two most popular ones are a circular orifice and a rectangular slot (Seifert et al. 1993, Amitay et al. 1999). We focus our study on a 2-dimensional actuator, which can be viewed as a rectangular actuator with a long slot in the spanwise direction, as shown in Figure 2.

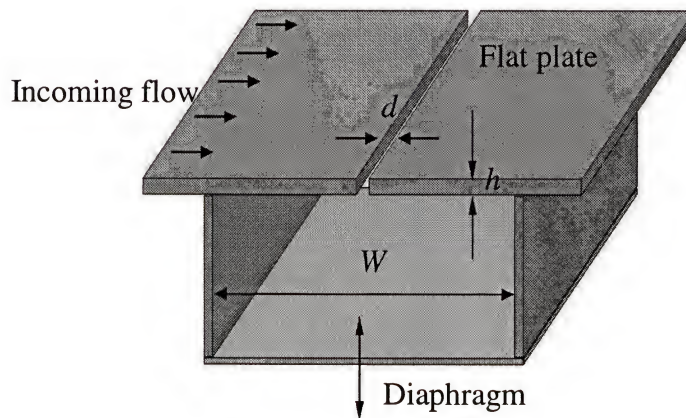


Figure 2. Synthetic jet actuator with the rectangular chamber and slot simplified to the 2-D model in the current study.

### 1.3 Literature Survey

Blowing and/or suction are well-established techniques in the arena of separation control (Schlichting & Gersten 1996, Gad-el-Hak & Bushnell 1991). Since the flow produced by the synthetic jet can be considered as a specialized application of the blowing/suction technique, it is worthwhile to provide some background regarding this technique. Separation of a boundary layer on a solid surface is primarily caused by



deceleration of flow due to an adverse pressure gradient. The flow adjacent to the boundary, which has the lowest momentum, eventually becomes stagnant. Mass conservation then dictates that the flow has to separate from the surface. All separation control techniques therefore aim to inhibit deceleration of flow in the boundary layer. The simple suction technique attempts to delay separation by removing the low momentum fluid. Tangential blowing (Seifert et al. 1993) can be considered the opposite of this where the objective is to directly add streamwise momentum to the boundary layer and thus delay separation. The use of trailing edge flaps in aircraft is actually motivated by similar consideration.

A somewhat different separation control approach comes from noting that turbulent boundary layers are more resistant to separation (Schlichting & Gersten 1996) than laminar boundary layers. Turbulent fluctuations tend to bring high-momentum external fluid into the boundary layer, thereby increasing the streamwise momentum of the flow adjacent to the boundary. This higher-momentum fluid is able to withstand the deceleration effect of the adverse pressure gradient over a large distance, and this leads to a reduction in separation. Thus, separation can be delayed by promoting earlier transition or by increasing the mixing in the boundary. This forms the motivation for a number of active separation-control techniques. Blowing/suction has also been used in this context by a number of researchers (Williams et al. 1991, Seifert et al. 1993) where, typically, a periodic excitation is provided in the boundary layer by a time-varying jet. Jet location, frequency and amplitude are key parameters in implementing this technique. Current debate exists on what is the most effective range of forcing frequencies. If  $l_s$  is the characteristic length of the separation region (which is often of the same order of

magnitude as the wing chord) then the non-dimension forcing frequency can be defined as

$$F^+ = \frac{fl_s}{U_\infty}$$

where  $f$  is forcing frequency and  $U_\infty$  is the freestream velocity.

A number of studies found that the most effective frequency for separation control corresponds to  $F^+ = O(1)$  (Seifert et al. 1993). Other studies (Hsiao et al. 1990, Huang et al. 1987, Smith 1998) found that  $F^+ \gg 1$  (of  $O(10^2)$ ) is also effective in reducing separation. The physical mechanisms that these two frequency ranges tend to promote are very different. Low frequency ( $F^+ = O(1)$ ) tends to increase mixing by promoting the formation of large-scale vortical structures in the separated shear layer. On the other hand, high-frequency ( $F^+ \gg 1$ ) perturbation attempts to induce bypass transition (Seifert et al. 1999) in the boundary layer and thereby increase mixing through early transition to turbulence. Nonetheless, there is no conceptual conflict associated with the presence of these two disparate optimal frequency ranges. Which frequency range will be more effective in separation control depends on condition of the boundary layer. Obviously, if the separation occurs post-transition then only low-frequency perturbations are expected to be effective. However, if the separation occurs in a laminar boundary layer, then either technique may, in principle, be used effectively.

Returning to the blowing/suction technique, one set of experiment that is especially relevant to the current study are those of Seifert et al. (1993, 1996). Seifert et al. (1993, 1996) investigated the effects of oscillatory blowing as a tool to delay separation. Their experiments were carried out on a hollow, flapped NACA 0015 airfoil

equipped with a two-dimensional slot over the hinge of the flap. The flap extended over 25% of the chord and was deflected at angles as high as 40 degrees. Air was blown through the slot to provide perturbation to the boundary layer. The air jet comprised steady and oscillatory flow components. The steady blowing momentum coefficients could be varied independently of the amplitudes and frequencies of the superimposed oscillations. The steady flow was provided by compressed air, and the oscillatory flow was provided by a small blower regulated by a rotary valve. The frequency of the oscillatory flow could be controlled by the rate of rotation of the valve and the amplitude could be controlled by the pressure supplied to the blower. With the proper magnitude and frequency, the oscillatory blowing was found to increase the lift and reduce the drag of the airfoil quite appreciably. For this type of configuration, Seifert et al. (1999) also developed a simple scaling between the pressure fluctuation ( $P'$ ) inside the cavity and the velocity fluctuation ( $u'$ ) produced at the jet exit. According to this scaling,  $u' \propto P'$  for low amplitude blowing and  $u' \propto \sqrt{P'}$  for high amplitude.

Another experiment on oscillatory blowing was performed by Seifert et al. (1998a) on a small-unmanned air vehicle (UAV) whose wing was replaced by a wing based on the Eppler 214 airfoil of a larger span. The blowing mechanism was somewhat different from the previous experiments. In this study, the blowing was provided by an axial fan mounted inside the fuselage of the UAV. The air was blown to the slot located on the flap shoulder through an internal duct, and the oscillatory excitation was provided by redirecting the steady fan-flow from one wing to another. The Reynolds number base on the flap chord was about  $0.27 \times 10^6$  and, in this range of Re, it was found that the most



effective frequency for separation reduction and lift enhancement was about 50–70 Hz, which corresponds to  $F^+$  of 0.7 where  $F^+ = fc_f / U_\infty$ , and  $c_f$  was the flap chord.

### 1.3.1 Characterization of Synthetic Jets

James et al. (1994, 1996) studied the characteristics of the water jet generated by a resonantly driven piezoceramic actuator. The actuator used in this experiment was a circular type. This actuator was placed in the water tank as shown in Figure 3. Distribution of the streamwise and radial velocity components of the jet were measured using a single-component, frequency biased Laser Doppler Anemometer (LDA). The actuator surface velocity was also measured by the LDA. A sequence of photographs was recorded to study the formation of cavitation bubbles near the actuator surface.

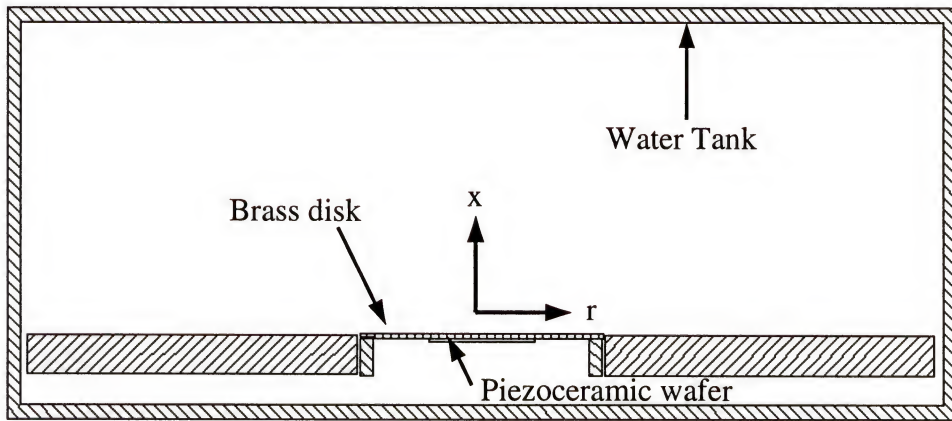


Figure 3. Top view of the experiment setup by James et al. (1996).

This study also explained the formation of cavitation bubbles using a simple potential flow model. The results of the experiments showed that the jet was present only when the excitation level of the actuator exceeds a given threshold, above which the mean fluid velocity on the jet centerlines increased linearly with input voltage even though the amplitude of diaphragm velocity remains nearly constant. It was also observed that above this threshold, minima of the pressure fluctuations associated with

the surface oscillations were sufficiently low to induce time-periodic formation of a small cluster of cavitation bubbles near the center of the actuator. The bubbles appeared, then apparently collapsed, and disappeared during each cycle of surface oscillation. Because the growth and collapse of the cavitation bubbles occurred on extremely small length and time scales, the mechanism of jet formation could not be completely resolved. It was conjectured that the jet was synthesized by a train of vortex ring clusters formed during each cycle of the surface oscillation due to secondary flow induced by the presence of the cavitation bubbles. Two mechanisms for the formation of these vortex ring clusters were proposed. The first was based on flow separation around each cavitation bubble when the instantaneous centerline velocity was directed toward the actuator. The second mechanism was connected with the formation of strong momentary jets during the collapse of cavitation bubbles near solid surfaces.

An important observation in this study was that even though the synthetic jet resulted from a strong time harmonic motion near the surface of the actuator, its mean flow became self-preserving farther downstream and was similar to that of a conventional round turbulent jet. Specifically, the width and inverse of the centerline velocity of the synthetic jet were found to be linear functions of the distance from the actuator, whereas the streamwise entrainment rate was invariant. The presence of strong spectral components at the excitation frequency and its higher harmonics in the streamwise velocity throughout the domain of measurements suggested that once the jet was formed, the evolution of the mean flow was superimposed on but decoupled from the time-periodic motion induced by the actuator.

Smith et al. (1999a) studied the formation, evolution and interactions of adjacent synthetic jets, which were placed side-by-side along the long dimensions of their orifice. In this experiment, the air jet generator comprised two adjacent cavities that were driven independently by piezoelectric disks. The velocity field of the synthetic jet was measured using particle image velocimetry (PIV). This experiment compared a single jet with a pair of adjacent jets operating in phase. Results of this study suggested that the combined flow of adjacent jets transported more fluid, that the entrainment of ambient fluid toward the jet orifice was stronger, and that the combined jet spreads faster with streamwise distance. It was also observed that when the vortices moved slowly, they were completely sucked back into the orifice. The faster-moving vortices were slowed down and remained essentially motionless during the suction cycle. This effect of the suction cycle decreased as the velocity at the orifice increased. Vectoring of adjacent jets was investigated by varying the phase angles of the driving signals of the two actuators. It was found that when the phase angle was increased, the combined jet began to vector toward the jet that was leading in phase. In this study, the effect of difference in phase angle could be divided into three primary domains. For the phase angle below 60 degrees, the combined vectored jet remained above the surface of the orifice plate. When the phase angle was between 70 and 100 degrees, the vectored jet formed recirculating flow bubbles near the surface, and the jet farther downstream was attached to the surface. When the phase angle exceeded 110 (but below 180), the recirculating bubble disappeared and the jet was completely attached to the surface.

Smith et al. (1999b) investigated the interaction of a synthetic jet actuator array with a thick turbulent boundary layer. The actuator array composed of three synthetic



jets, which consisted of two configurations. In the first configuration, the centerlines of the three actuator orifices were coincident and oriented perpendicular to the crossflow direction. In the second configuration, the three actuators were stacked together and oriented such that the centerlines of the orifices were parallel to each other and parallel to the crossflow direction. Due to the limited measurements, the structure of the boundary and wake downstream of the jet were difficult to fully understand from this study. However, this study showed that the orientation of the actuator strongly influenced the size of the wake.

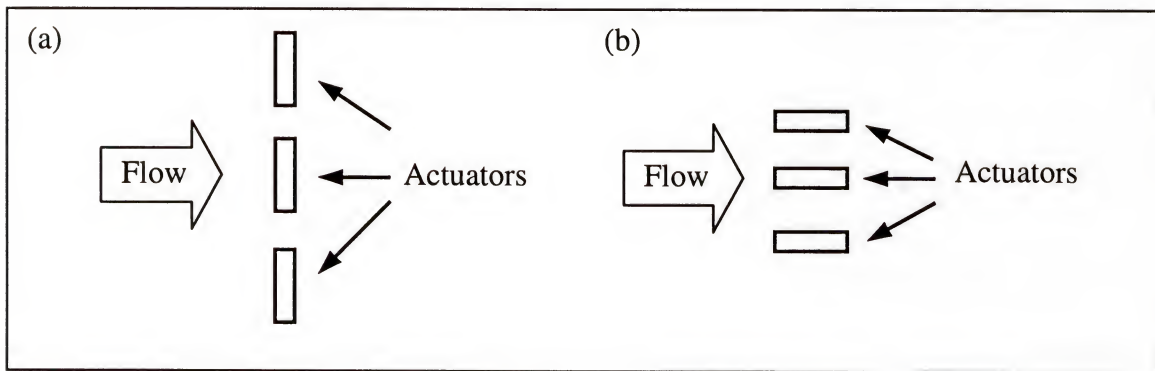


Figure 4. Experimental setup of Smith et al. (1999b). a) First configuration; b) Second configuration.

### 1.3.2 Application of Synthetic Jets to Separation Control

The application of synthetic jets to control separation was first studied by Amitay et al. (1997). In their experiments, a two-dimensional cylinder, which was modified to have a spanwise pair of synthetic jet actuators, was tested in the wind tunnel. The cylinder could be rotated about its centerline so that the angle between the actuator and the freestream could be varied continuously. It was hypothesized that the interaction of the jet and the main flow would lead to the formation of closed recirculation region and to the apparent modification of the flow on scales that were one or two orders of

magnitude larger than the characteristic length scale of the jets themselves. The modification of the flow was investigated at Reynolds number (based on the diameter of the cylinder) about 4000 using smoke visualization. The smoke visualization suggested that the interaction of the jets with the cross flow led to the formation of a closed flow region near the surface, which resulted in local deformation of streaklines. It was apparent that the separation point on the cylinder moved downstream and these global changes were accompanied by variation in azimuthal distribution of the static pressure on the surface of the cylinder. The improvement in lift and drag performance was also shown. This study also showed that the lift force could be manipulated by changing the location of the actuators.

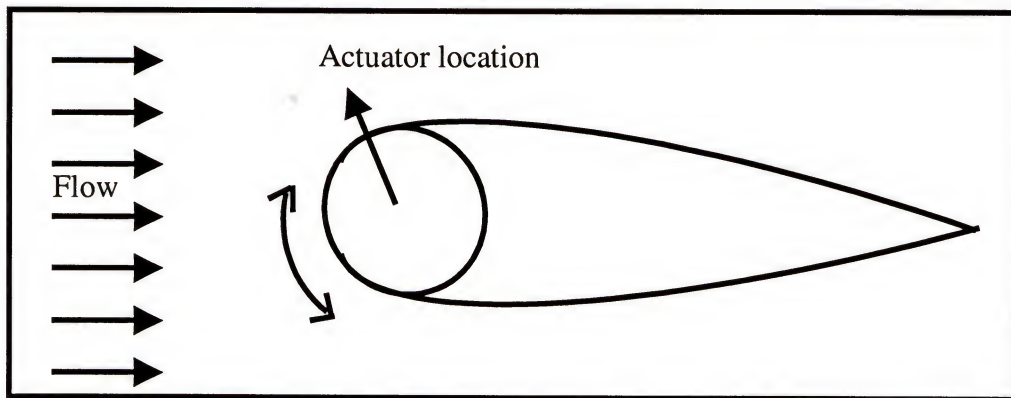


Figure 5. Airfoil used in the experiment of Smith et al. (1998)

The above study was extended by Smith et al. (1998) where an unconventional airfoil was used instead of the cylinder. Their experimental setup is shown in Figure 5. In their experiment, a symmetric airfoil based on the aft portion of a NACA four digit series airfoil with a cylindrical leading edge was used. The cylinder in the front portion of the airfoil could be rotated independently from the faring. This cylinder was equipped with two synthetic jet actuators, and by rotating the cylinder, the angle between the slots

and the oncoming flow can be adjusted. The angle of attack of the airfoil was varied between  $-10$  and  $25$  degrees. Without the control, airfoil was found to stall at angle-of-attack greater than  $5$  degrees. With control, the airfoil was found to stall at angle-of-attack greater than  $15$  degrees and the lift and drag performance was significantly improved. Both the location and the strength of the control input were found to affect the extent of the reattached flow.

A similar experiment of flow over a cylinder equipped with a synthetic jet actuator was performed by Crook et al. (1999) at higher Reynolds number ( $Re_\delta = 555,000$ ) compared to  $Re_\delta$  about  $4,000$  and  $75,000$  of Amitay et al. (1997). In this study, experiments as well as an analytical model were used. Optimized values of actuator parameters were estimated from the analytical model using genetic algorithms and then tested in the experiments. The experimental testing focused on obtaining the maximum jet velocity using different cavity height, orifice and slit depths, orifice diameters, and slit width/lengths and different membrane thickness and piezoceramic actuators. The results from the experiment were compared with those predicted by the model and it was found that the analytical model did not successfully predict the maximum jet velocity at the orifice. This study suggested that viscous effects dominate the flow for small values of the orifice diameter, so the inviscid model fails to provide a good result.

Seifert et al. (1998b) showed that the actuators mounted on the upper surface of an airfoil were effective as well as energy efficient. An airfoil was machined on its upper surface and ten actuators were installed along the span of the airfoil. The actuators were operated in two modes: a two-dimensional mode where all actuators were operated at identical amplitude and phase and a three-dimension mode, where the amplitude were



identical but the phase of alternate actuators was reversed. When all actuator operated in two-dimensional mode, two-dimensional vortices were created and more complicated vortices were created in the three-dimensional mode operation. One conclusion of this study was that the 2-D mode was appropriate for take-off whereas the 3-D mode had better power efficiency.

### 1.3.3 Numerical Studies of Synthetic Jets

To date, most studies of synthetic jets have been accomplished in experiments. However, there are three numerical studies of synthetic jet that should be addressed here.

Kral et al. (1997) performed two-dimensional, incompressible simulations of a synthetic jet with a quiescent external flow. In this study, the actuator was not included in the calculation. Instead, a modeled velocity profile at the jet exit was prescribed as a portion of the boundary condition. This velocity profiles had the form

$$\bar{u}_n(\eta, t) = U_0 f(\eta) \sin(\omega t)$$

where  $\eta$  denoted the cross-stream direction

$U_0$  was the amplitude of velocity, and

$f(\eta)$  was the function of spatial variation of velocity

$$f(\eta) = \begin{cases} 1 \\ \sin(\pi\eta) \\ \sin^2(\pi\eta) \end{cases}$$

Using this profile eliminated the need to calculate flow inside the cavity. Since this distribution was a simple sinusoidal function, it creates a symmetric velocity profile for the expulsion and the suction stage. As will be shown later, an actual synthetic jet exhibits a very different type of spatial and temporal variation.

In this study (Kral et al. 1997), both laminar and turbulent jets were investigated using two different solvers. Initially the laminar jet calculation was performed to understand the ability of the synthetic jet to entrain the surrounding fluid and create the jet. The turbulent jet calculations were then performed to explore the behavior of the jet that might not be captured by the laminar jet model. In both parts of the study, the steady jet was used as the baseline case to compare the performance of the synthetic jets.

It was found that the synthetic jet could create a non-zero mean streamwise velocity even though the actuator operated with zero net mass flux. However, the velocity induced by the synthetic jet was found to be smaller than the velocity of the steady jet due to the suction portion of the synthetic jet cycle. It was also observed that the laminar jet did not capture the breakdown of the vortex train that had been observed experimentally while the turbulent model showed that the counter-rotating vortices dissipate quickly. This study suggested that the modeled boundary condition could capture some of the features of the jet without the simulation of the flow inside the actuator cavity.

A second numerical study was performed by Rizzetta et al. (1998). This study used DNS to solve the compressible Navier-Stokes equations. The Reynolds number (based on the jet velocity at the slot and the slot width) ranged from 750 to 1500 and the jet mach number was 0.065. Unlike the previous study by Kral et al. (1997), both the interior of the actuator cavity and the external flowfield were calculated. The flow inside the cavity was simulated by prescribing the oscillating boundary condition at the lower boundary of the cavity. Since periodic behavior of velocity at the jet exit was observed after several cycles of cavity boundary, the recorded profiles of the jet exit velocity were



used as the boundary condition for the exterior domain. By using this decoupling technique, the calculation of the exterior flow could be performed without simultaneous simulation of the flow inside the actuator cavity at the same time. In order to reduce the computational cost, the planes of symmetry were forced at the jet centerline and at the mid-span location so only a quarter of the real actuator was simulated.

The results of 2-D and 3-D simulations were compared with the experimental results. The 2-D simulation shows that the geometry of the actuator strongly affects the jet exit velocity profiles. These velocity profiles were periodic in time and it was possible to obtain the temporal statistics over several cycles of oscillation, whereas the period of repetitive behavior of the 3-D simulation was longer. It was also found that the 2-D simulation could not capture the breakdown of the vortices as a result of the spanwise instabilities, whereas this phenomenon was observed in both experiment and in 3-D simulations.

Recently Lee & Goldstein (2001) have studied the interaction of 3-D synthetic jets with a turbulent boundary layer. Their studies used direct numerical simulation to solve incompressible Navier-Stokes equations. The diagram of the simulation configuration is shown on Figure 6. The setup was composed of two pairs of long slots arranged side by side with their length aligned with the main flow direction. The jets were created by the horizontal movement of the vertical walls underneath the virtual surface. Since each moving wall controlled two synthetic jets, the jets in the same pair operated 180 degrees out of phase. The virtual surface and the moving walls in the diagram were represented using the virtual force method. This method imposed a localized body force along desired points in the computational mesh to bring the fluid

there to a specified velocity so that the force had the same effect as a solid boundary. By controlling the phase difference of the two moving walls, the jets could be operated in different modes. The main flow over the virtual surface had a  $Re = 2200$ , based on the channel half height and a centerline velocity.

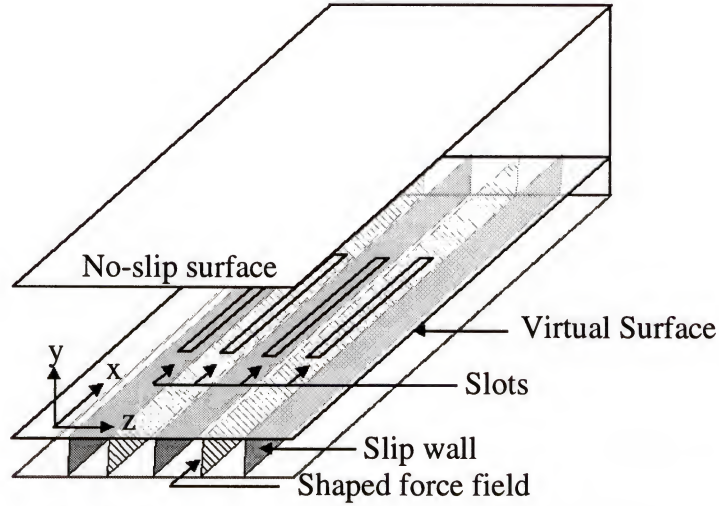


Figure 6. Synthetic jet actuators configuration in the study by Lee & Goldstein (2001).

Their study was divided into four stages. The first stage was to study the effect of the inactive actuators. It was found that the presence of the slots did not show any mean effect to the main flow. The second part of this study was to operate the actuators with the quiescent external flow. The jet Reynolds number, based on the average maximum jet velocity ( $u_{peak}$ ) and half width of the jet ( $h_{1/2}$ ), was equal to 34 and the Strouhal number, defined as  $St_{jet} = 2\pi f h_{1/2} / u_{peak}$ , was equal to 0.13. In this part, it was observed that the adjacent jets repelled each other. If the actuators were operated in a mode that created suction and blowing, the jet tended to move toward the suction slot. The third part of the study was the quasi-steady actuation. This part of study included the turbulent external flow with a quasi-steady jet. It was observed that the fluid ingested in to the

cavity retained some of its momentum while the fluid ejected had very small streamwise momentum. Thus, there was a noticeable difference between the ingestion and expulsion stage. The final stage of this study was to operate the actuators with a full period of oscillation in the turbulent external main flow. The movement of the vertical wall (membrane) was control by a sinusoidal function. The Strouhal number and the jet Reynolds number were 0.33 and 13.6, respectively. It was found that the average drag over the time interval was about 10 percent higher than that of the fixed wall. A comparable increase in drag was also observed when the actuator was operated in the other mode. This study suggested that the drag increase might be independent of the mode of operation but dependent on the particular type of the actuator.

#### **1.3.4 Other Applications of Synthetic Jets**

In addition to the applications of active flow control, synthetic jets are also used in other applications such as thrust vectoring and mixing enhancement. Since these applications are not directly related to the current study, only a brief review of the applicable literature is provided here.

Smith et al. (1999a) performed an experiment using two synthetic jet actuators placed along the side of the rectangular conduit of the primary jet. Each actuator had two modes of operation depending on direction of the synthetic jet to the primary jet. It was demonstrated that the primary jet could be vectored at different angles by operating only one or both actuators in different modes. A maximum vector angle exceeding 80 degrees could be achieved.

Chen et al. (1999) demonstrated the use of synthetic jets to enhance mixing in a gas turbine combustor. They simulated the mixing by using two streams of hot and cold gas and measured the temperature distribution downstream of the synthetic jet to



determine the effectiveness of the mixing. Their experiment showed that synthetic jets could improve mixing in a turbine jet engine without using additional cold dilution air.

Davis et al. (1999) investigated the utility of synthetic jet actuators for the modification and control of small-scale motions and mixing processes. This experiment used an array of synthetic jet actuators placed around the perimeter of the primary jet. These actuators had a different configuration from the jets in Figure 1 but also operated with zero net mass flux. It was demonstrated that the synthetic jets made the shear layer of the primary jet spread faster with downstream distance, and the centerline velocity decreased faster in the streamwise direction. The synthetic jets also increased velocity fluctuations in the flowfield near the centerline.

## CHAPTER 2 OBJECTIVES AND APPROACH

### 2.1 Parameter Study

#### 2.1.1 Flow Configuration

Consider the synthetic jet device in Figure 7, which is attached beneath a flat plate on which develops a laminar Blasius boundary layer. The synthetic jet is created at the slot by the oscillation of a diaphragm attached to the bottom of the jet cavity and the diaphragm deflection is characterized by the deflection amplitude ( $A$ ) and angular frequency ( $\omega$ ). The rectangular cavity is defined by the cavity width ( $W$ ) and the cavity height ( $H$ ). A slot type exit is chosen for the jet and this orifice is characterized by a height ( $h$ ) and width ( $d$ ). The exterior flow, which consists of a laminar Blasius boundary layer, is characterized by a freestream velocity ( $U_\infty$ ), boundary layer thickness ( $\delta$ ), displacement thickness ( $\delta^*$ ) and momentum thickness ( $\theta$ ). Finally, the fluid is characterized by its kinematic viscosity ( $\nu$ ) and density ( $\rho$ ).

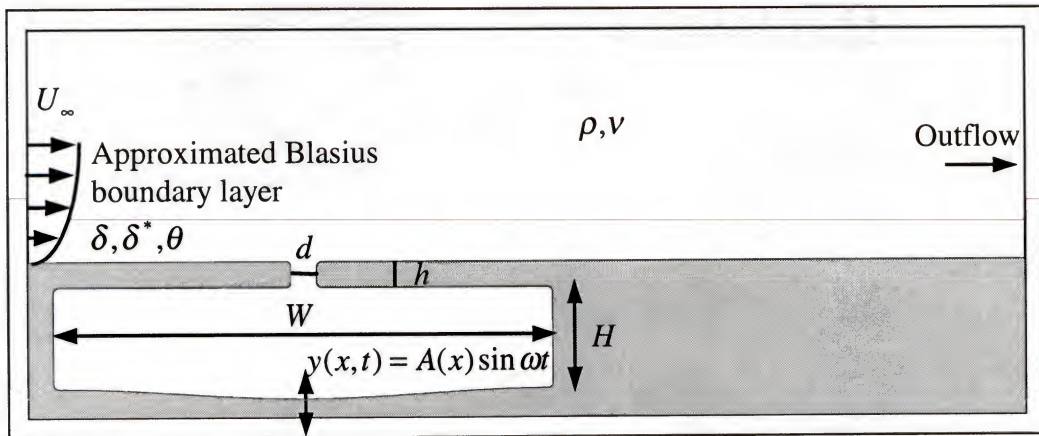


Figure 7. 2-D synthetic jet configuration used in the current study.

Additional parameters need to be considered in the situation where compressibility effects inside the cavity become significant. However, from the point of view of device efficiency, it might be advantageous to operate in the incompressible flow regime and this can be easily accomplished by detuning the diaphragm frequency from the acoustic resonance frequency of the cavity. Therefore, with the underlying assumption that actual devices will be designed to operate in the incompressible flow regime, in the current study we will also focus only on this regime.

### 2.1.2 Jet Characterization and Scaling

The flow emerging from the slot is in principle a function of all the parameters described in the paragraph above. The exit flow, which is both a function of space and time, can be characterized through a number of different parameters. In many previous studies, a parameter considered key to characterizing the jet is the momentum coefficient (Amitay et al. 1997, Seifert et al. 1996) which is the net momentum imparted by the jet over one cycle non-dimensionalized by a suitable quantity. However, it is by no means obvious that the momentum imparted by the jet is the primary agent that affects the external flow. For instance, the velocity inside the orifice/slot is expected to scale with the peak jet velocity, which may indicate the importance of this parameter. Similarly, other parameters like the net energy flux, mass flux during expulsion, etc. might also be important. Thus, even the choice of parameters that are key to characterizing the jet in the presence of external flow is an open question.

A more general approach to characterizing the velocity field is through its successive moments as follows: The  $n^{\text{th}}$  moment of the jet over the phase interval from  $\phi_1$  to  $\phi_2$  is defined as  $C_{\phi_{12}}^n$



$$C_{\phi_{12}}^n = \frac{1}{\phi_2 - \phi_1} \frac{1}{d} \int_{\phi_1}^{\phi_2} \int_{-d/2}^{d/2} [V_j(x, \phi)]^n dx d\phi \quad (1)$$

where  $V_j$  is the jet velocity normalized by a suitable velocity scale (freestream velocity or average inviscid orifice velocity given by  $V_{ave}^{inv} = AW\omega / \pi d$ ).

The preliminary simulations indicated that the jet flow is significantly different during the ingestion and expulsion phases, and characterizing this difference is one key aspect to understanding the physics of this flow. Thus, it is natural to define the moment separately for the ingestion and expulsion phases and these are denoted by  $C_{in}^n$  and  $C_{ex}^n$  respectively. This hierarchical characterization in terms of the moments of the velocity profile is extremely useful since it provides a systematic framework for the development of scaling laws. Furthermore, this type of characterization is not simply for mathematical convenience since a number of these moments have direct physical significance. For instance  $\rho(C_{in}^1 + C_{ex}^1)$  corresponds to the jet mass flux (which is identically equal to zero for a synthetic jet) whereas  $\rho(C_{in}^2 + C_{ex}^2)$  and  $\rho(C_{in}^3 + C_{ex}^3)/2$  correspond to the momentum and kinetic energy flux of the jet. Note that the kinetic energy flux is also a measure of the difference in the profile during ingestion and expulsion phases. Finally for  $n = \infty$ ,  $(C_{ex}^n)^{1/n}$  represents the maximum jet exit velocity. In addition to the moments, the skewness of the velocity profile about the slot center, which early simulations indicated might be another key feature of the jet, can be estimated as

$$X_{\phi_{12}} = \left[ \frac{1}{\phi_2 - \phi_1} \frac{1}{d} \int_{\phi_1}^{\phi_2} \int_0^{d/2} [V_j(x, \phi) - V_j(-x, \phi)]^2 dx d\phi \right]^{1/2} \quad (2)$$

With the jet characteristic parameters chosen in this manner, the question now is to determine their dependence on the flow and geometrical parameters of this configuration. Using the Buckingham Pi theorem (Buckingham 1915), this functional dependence can be written in terms of non-dimensional parameters as:

$$(C_{\phi_{12}}^n; X_{\phi_{12}}) = fn\left(\frac{W}{H}, \frac{A}{H}, \frac{h}{d}, \frac{d}{W}, \sqrt{\frac{\omega d^2}{\nu}}, \frac{U_{\infty} \delta}{\nu}, \frac{\delta}{d}\right) \quad (3)$$

where  $W/H$  : Cavity width to height ratio of cavity

$A/H$  : Stroke length to cavity height ratio

$h/d$  : Orifice height to width ratio

$d/W$  : Aspect ratio of slot

$\sqrt{\omega d^2 / \nu} = S$  : Stokes number

$U_{\infty} \delta / \nu = Re_{\delta}$  : Boundary layer thickness Reynolds number

$\delta / d$  : Ratio of boundary layer thickness to slot width

It is worth noting that the first five parameters on the RHS of Equation (3) depend only on the synthetic jet device, whereas the last two parameters depend on the outer boundary layer. The first objective of a scaling analysis would then be to investigate the functional dependence denoted in Equation (3). From previous studies, it is clear that the moment coefficients will depend on the jet and slot parameters. However, it is not clear what effect the exterior flow parameters have on the jet flow. This requires an investigation of the two-way coupling of the exterior and interior flow, which is an objective of this study.



### 2.1.3 Effect of the Jet on the External Flow: Characterization and Scaling

In the current study, we propose a two-step approach to the scaling analysis. The first step has been described above where we investigate the dependence in Equation (3). Once this has been accomplished, we will answer the next question: How does the effect of the synthetic jet on the exterior flow depend on the jet? However, the analysis of the effect of the jet on the external flow is limited here by the assumption of two-dimensionality. Due to this restriction, important effects such as bypass transition and/or enhanced mixing due to 3-D vortex structures cannot be explored. Instead, the focus will primarily be the investigation of the so-called “virtual aero-shaping” effect of synthetic jets to create large mean recirculation bubbles which can modify the effective shape of the body. This effect has been alluded to in the past (Amitay et al. 1997, Chatlynne et al. 2001), but little is known regarding the scaling of this effect on the jet parameters. In the current study, we denote the length of the mean recirculation bubble by  $L_r$  and investigate the scaling of this with the jet parameters.

In general, we may assume that the length of the mean recirculation bubble will have the following dependence for a synthetic jet with fixed geometry

$$(L_r; \dots) = fn\left(C_{ex}^n, S, \frac{\delta}{d}, Re_\delta\right) \quad (4)$$

The objective here is to obtain a precise characterization of this functional dependence.

Clearly, the parameter space of this flow configuration is enormous and difficult to cover in any single investigation. Therefore, the focus will be on the parameters expected to have strong influence on the characteristic of the flow. The internal jet parameters to be varied in the current study are the diaphragm amplitude ( $A/H$ ) and the orifice height to width ratio ( $h/d$ ). Both external parameters (i.e.,  $Re_\delta$  and  $\delta/d$ ) will also

be varied. These parameters are chosen because preliminary simulations indicated that the jet exhibits significant variation with these parameters, and it was felt that good insight into the physics of this flow could be gained by varying these parameters. Note that the geometry of the jet cavity is not varied here. We expect to investigate the effect of geometric variations in a future study. Some idea regarding the potential effect of these parameters can be obtained by considering the inviscid limit of the jet flow. Given that the diaphragm deformation is prescribed as

$$y = y_0 + a(x) \sin(\omega t) \quad (5)$$

where

$$a(x) = \frac{A}{2} \left[ 1 - \cos \left( 2\pi \frac{x - x_1}{W} \right) \right]$$

and  $x_1$  is the  $x$ -location of the left end of the diaphragm, it can be shown easily that the maximum inviscid velocity at the orifice is

$$V_{\max}^{inv} = \frac{AW\omega}{2d} \quad (6)$$

Thus the normalized maximum inviscid jet velocity depends on the parameters indicated by Equation (5) and can therefore be controlled by varying these parameter.

$$\frac{V_{\max}^{inv}}{U_{\infty}} = \frac{1}{2} \left( \frac{W}{d} \right)^2 \frac{A}{H} \frac{H}{W} \frac{S^2}{\text{Re}_{\delta}} \frac{\delta}{d} \quad (7)$$

The average of the inviscid velocity in the expulsion stroke is

$$V_{ave}^{inv} = \frac{2}{\pi} V_{\max}^{inv} \quad (8)$$

and can be rewritten as

$$\frac{V_{ave}^{inv}}{U_{\infty}} = \frac{1}{\pi} \left( \frac{W}{d} \right)^2 \frac{A}{H} \frac{H}{W} \frac{S^2}{Re_{\delta}} \frac{\delta}{d} \quad (9)$$

The average of the inviscid velocity of the ingestion stroke has the same magnitude but different sign. Note that this average inviscid jet velocity is also the average velocity of the jet in the viscous case due to mass conservation.

The flow inside the jet slot can be considered to be governed by the following parameters:  $S$ ,  $Re_d = V_{ave}^{inv} d / \nu$  and  $h/d$ . Since in the current study the geometry of the jet cavity ( $W/H$ ) is not changed, the flow through the slot can be related directly to the above three parameters. Thus, a change in  $A/H$  can effectively be viewed as change in the slot flow Reynolds number ( $Re_d$ ). This viewpoint is very useful since it decouples the jet from the details of the flow inside the cavity.

The parameter  $h/d$  also has a significant impact on the jet flow. If we consider fluid flow through the actuator slot as an oscillatory channel flow, we can have different velocity profiles at the exit of the slot depending on whether the flow in the slot is fully developed or not. If the length of the slot ( $h$ ) is longer than the entrance length, we expect a fully developed velocity profile. If the length of the slot ( $h$ ) is shorter than the entrance region length, we expect more of a plug type flow profile. The connection between the ratio  $h/d$  and the entrance length ( $y_L$ ) can be examined by considering experimental correlation for the entrance length ( $y_L$ ) given by Wood (1999)

$$\frac{y_L}{d} = \frac{\gamma Re_d}{S^2} \quad (10)$$

where  $Re_d$  is the Reynolds number based on the channel width and a suitable velocity scale characterizing the channel and  $\gamma$  is a constant. In estimating this for the current

flow, an inviscid jet velocity is an appropriate velocity scale.  $Re_d$  can be written in term of non-dimensional parameters as

$$Re_d = \frac{1}{\pi} \left( \frac{A}{H} \right) \left( \frac{H}{W} \right) \left( \frac{W}{d} \right)^2 S^2 \quad (11)$$

In order to have fully developed flow at the jet exit,

$$\frac{y_L}{h} < 1$$

$$\text{or} \quad \frac{y_L}{h} = \frac{\gamma}{\pi} \left( \frac{d}{h} \right) \left( \frac{A}{H} \right) \left( \frac{H}{W} \right) \left( \frac{W}{d} \right)^2 < 1 \quad (12)$$

Thus by varying the slot height to slot width ratio ( $h/d$ ), different velocity profiles are expected at the jet.

Finally, boundary layer thickness Reynolds number ( $Re_\delta$ ) is expected to have a strong effect on the velocity profile both during the ingestion and expulsion phases and the effect of this parameter will also be studied through systematic parametric variation.

The range of values chosen for the various parameter is shown in Table 1 in Chapter 4. Each simulation is carried out until the flow reaches a stationary state. The simulation is then continued for a few more cycles and the flow statistics are recorded over this time interval. In particular, the jet velocity profiles are recorded and subsequently analyzed to obtain various statistical measures of the jet profile.



### CHAPTER 3

#### NUMERICAL METHOD

In the current study, a previously developed Cartesian grid solver (Udaykumar et al. 1999; Ye et al. 1999; Udaykumar et al. 2000) is used. This solver allows simulation of unsteady viscous incompressible flows with complex immersed moving boundaries on Cartesian grids. Thus, the grid does not need to conform to the complex moving boundaries and this simplifies the gridding of the flow domain. The solver uses a second-order accurate central-difference scheme for spatial discretization and a mixed explicit-implicit fractional step scheme for time advancement. An efficient multigrid algorithm is used for the solving the pressure Poisson equation.

The key advantage of this solver for the current investigation is that the entire geometry of the synthetic jet including the oscillating diaphragm is modeled on a stationary Cartesian mesh. As the diaphragm moves over the underlying Cartesian mesh, the discretization in the cells cut by the solid boundary is modified to account for the presence of the solid boundary. In addition, suitable boundary conditions also need to be prescribed for the external flow. For the quiescent external flow case, a soft velocity boundary condition (corresponding to a homogeneous Neumann condition) is applied on the external boundaries. In the simulations with an external crossflow, an approximated Blasius boundary layer profile is prescribed on the incoming boundary and a soft velocity boundary condition is prescribed on the upper boundary, which is located more than  $40d$  away from the slot. On the east boundary, a soft boundary condition is applied which

allows vortex structures to convect out of the domain with minimal distortion and reflections. Details of the solution procedure are described in the following sections.

The key aspects of the algorithm include the following:

- A fractional-step scheme (Chorin 1968, Ferziger & Peric 1996) that results in a fast solution of unsteady flows.
- Adoption of a compact interpolation scheme (Ye et al. 1999) near the moving immersed boundaries that allows us to retain second-order accuracy and conservation property of the solver.
- A full approximation storage (FAS) multigrid technique (Alcouffe 1981) with line-SOR smoothing, that substantially accelerates the convergence of the pressure Poisson equation (PPE) with/without immersed boundaries in the domain.

These aspects are described in detail in the following sections.

### 3.1 Governing Equations and Flow Configuration

The schematic in Figure 8 shows a solid with a curved boundary moving through a fluid, which illustrates the typical flow problem of interest here. The equations solved are the incompressible Navier-Stokes equations. The non-dimensionalized, integral form of these equations is given by:

$$\int_S \vec{u} \cdot \hat{n} dS = 0 \quad (13)$$

$$St \frac{\partial}{\partial t} \int_V \vec{u} dV + \int_S \vec{u} (\vec{u} \cdot \hat{n}) dS = - \int_S p \hat{n} dS + \frac{1}{Re} \int_S \nabla \vec{u} \cdot \hat{n} dS \quad (14)$$

where  $\vec{u}$  and  $p$  are the non-dimensional velocity and pressure respectively,  $St$  and  $Re$  are the Strouhal number and Reynolds number respectively which are defined as  $St = \omega L / U_o$  and  $Re = U_o L / \nu$ , where  $\omega$  is an imposed frequency,  $L$  the length scale,  $U_o$  the velocity scale and  $\nu$  the kinematic viscosity. In the above equations, subscripts  $V$  and  $S$  denote the volume and surface of the control volume respectively, and  $\hat{n}$  is a unit vector normal to

the surface of the control volume. The above equations are to be solved with  $\vec{u}(\vec{x}, t) = \vec{u}_0(\vec{x}, t)$  on the boundary of the flow domain where  $\vec{u}_0(\vec{x}, t)$  is the prescribed boundary velocity, including that at the moving immersed boundary. The above equations with the moving immersed boundary are to be discretized and solved on a Cartesian mesh shown in Figure 8. The discretization of the above equations in the context of a stationary immersed boundary is described first. With this as the basis, the discretization scheme in the presence of moving boundaries is described subsequently.

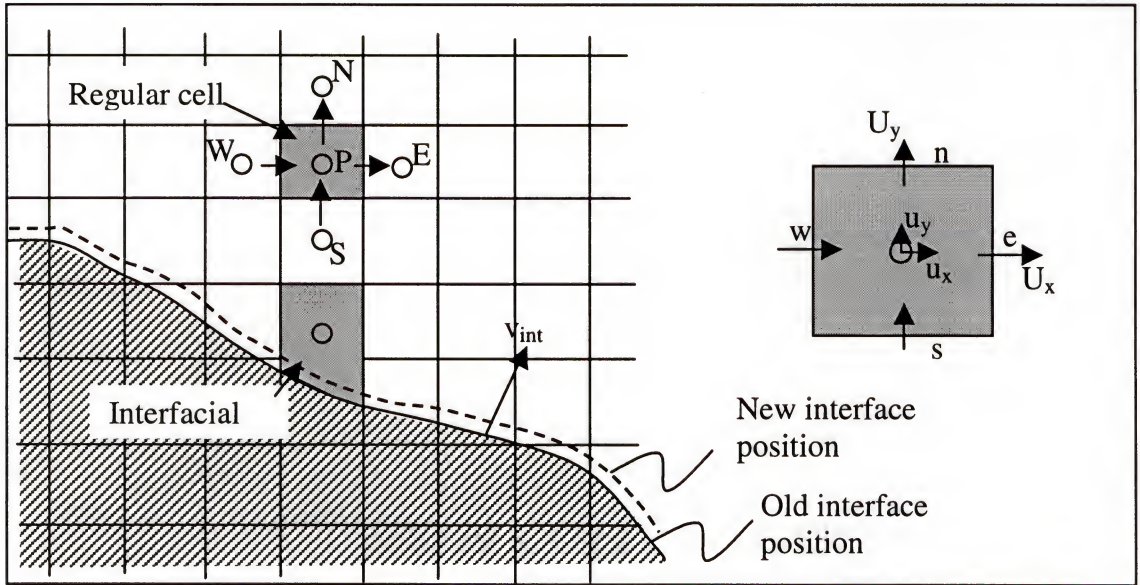


Figure 8. Moving boundary cutting through a fixed mesh.

### 3.2 Flow Solver with Stationary Immersed Boundaries

As the first step, the curved immersed boundary is represented using marker particles which are connected by piecewise quadratic curves parameterized with respect to the arc length ( $s$ ). Details regarding interface representation, evaluation of derivatives along the interface to obtain normals, curvatures etc. can be found in the papers by Udaykumar et al. (1999) and by Ye et al. (1999). Also described in those papers are



details regarding the projection of the immersed boundary onto the underlying fixed Cartesian mesh. This includes determining the intersection of the boundary with the mesh, identifying the phase (solid or fluid) of each cell, and procedures for obtaining a mosaic of control volumes, which are clearly demarcated by the immersed boundary. This results in the formation of control-volumes adjacent to the immersed boundary that are trapezoidal in shape as shown in Figure 8. Depending on the location and local orientation of the immersed boundary, trapezoidal cells of varying aspect ratio are formed. It should be pointed out that due to the cell merging operation (Ye et al. 1999), the nominal aspect ratio of the trapezoidal cells is limited to a range between 0.5 and 1.5, which is advantageous from the point of view of conditioning of the discrete operators. With the boundary-adjacent grid cells reconstructed in this manner, we now turn to the discretization of the governing equations (13) and (14) on this grid.

A two-step, mixed explicit-implicit fractional step scheme (Mittal & Balachandar 1996) is used for advancing the solution of the above equations in time. The Navier-Stokes equations are discretized using a cell-centered, colocated (non-staggered) arrangement (Rhie & Chow 1983, Zang et al. 1994) of the primitive variables  $(\vec{u}, p)$ . In addition to the cell-center velocities, which are denoted by  $\vec{u}$ , face-center velocities  $\vec{U}$  are also computed. In a manner similar to a fully staggered arrangement, only the component normal to the cell-face is computed and stored (see Figure 8). The face-center velocity is used for computing the volume flux from each cell in the current finite-volume discretization scheme. The advantage of separately computing the face-center velocities was discussed in the context of the current method in Ye et al. (1999). The solution is advanced from time level  $t$  to  $t + \Delta t$  through an intermediate advection-



diffusion step where the momentum equations without the pressure gradient terms are first advanced in time. A second-order Adams-Bashforth scheme is used for the convective terms and the diffusion terms are discretized using an implicit Crank-Nicolson scheme. This eliminates the viscous stability constraint, which can be quite severe in simulation of viscous flows. The discretized form of the advection-diffusion equation for each cell shown in Figure 8 can therefore be written as follows:

$$\text{St} \frac{\vec{u}^* - \vec{u}^t}{\Delta t} \Delta V = -\frac{1}{2} \sum_f \left[ 3\vec{u}^t (\vec{U}^t \cdot \hat{n}_f) - \vec{u}^{t-\Delta t} (\vec{U}^{t-\Delta t} \cdot \hat{n}_f) \right] \Delta S_f + \frac{1}{2 \text{Re}} \sum_f \left[ \nabla u^* + \nabla u^t \right] \hat{n}_f \Delta S_f \quad (15)$$

where  $\vec{u}^*$  is the intermediate cell-center velocity and subscript  $f$  denotes one face of the control volume. This equation is solved with the final velocity imposed as the boundary condition, i.e.  $\vec{u}_0^*(\vec{x}) = \vec{u}_0(\vec{x}, t + \Delta t)$ . The intermediate face-center velocities  $\vec{U}^*$  are obtained at this point by interpolating the intermediate cell-center velocities  $\vec{u}^*$ .

The advection-diffusion step is followed by the pressure-correction step in which the following integral equation is discretized:

$$\text{St} \int_V \frac{\vec{u}^{t+\Delta t} - \vec{u}^*}{\Delta t} dV = - \int_V \nabla p^{t+\Delta t} dV \quad (16)$$

By requiring a divergence-free velocity field at the end of the time-step the following elliptic equation for pressure is obtained:

$$\sum_f \nabla p^{t+\Delta t} \cdot \hat{n}_f \Delta S_f = \frac{\text{St}}{\Delta t} \sum_f \vec{U}^* \cdot \hat{n}_f \Delta S_f \quad (17)$$

With stationary, non-porous boundaries, a homogeneous Neumann boundary condition for pressure results in a consistent approximation of the Navier-Stokes equations (Temam 1991). Once the pressure is obtained by solving Equation (17), both the cell-center and

face-center velocities,  $\vec{u}$  and  $\vec{U}$  are updated separately as follows:

$$\vec{u}^{t+\Delta t} = \vec{u}^t - \Delta t (\nabla p^{t+\Delta t})_{cc} \quad (18)$$

$$\vec{U}^{t+\Delta t} = \vec{U}^t - \Delta t (\nabla p^{t+\Delta t})_{fc} \quad (19)$$

where subscripts  $cc$  and  $fc$  indicate evaluation at the cell center and face center locations respectively. Further discussion regarding the adoption of cell-center and face-center velocities can be found in Zang et al. (1994) and in the context of the present method in Ye et al. (1999).

The key element in the finite-volume discretization of the Equations (15)-(17) in the context of the current method is the evaluation of fluxes and derivatives at the faces of each control volume. These include momentum, mass and diffusive fluxes and gradients of pressure. A detailed discussion of this aspect, including validation of the accuracy of the solution procedure was presented in Ye et al. (1999). For the regular Cartesian cells away from the immersed boundary, the fluxes and pressure gradients on the face-centers can be computed to second-order accuracy by assuming a linear variation between adjoining cell-centers. This is not the case for a trapezoidal boundary cell since the center of some of the faces of such a cell may not lie halfway between neighboring cell-centers. This is seen from Figure 9(b) and Figure 9(c) where the locations where fluxes are evaluated are indicated by the filled arrows. A linear approximation would not provide a second-order accurate estimate of the gradients. Furthermore, some of the neighboring cell-centers do not even lie on the same side of the immersed boundary and therefore cannot be used in the differencing procedure. Thus, a different approach is needed in order to discretize the equations in these cells.

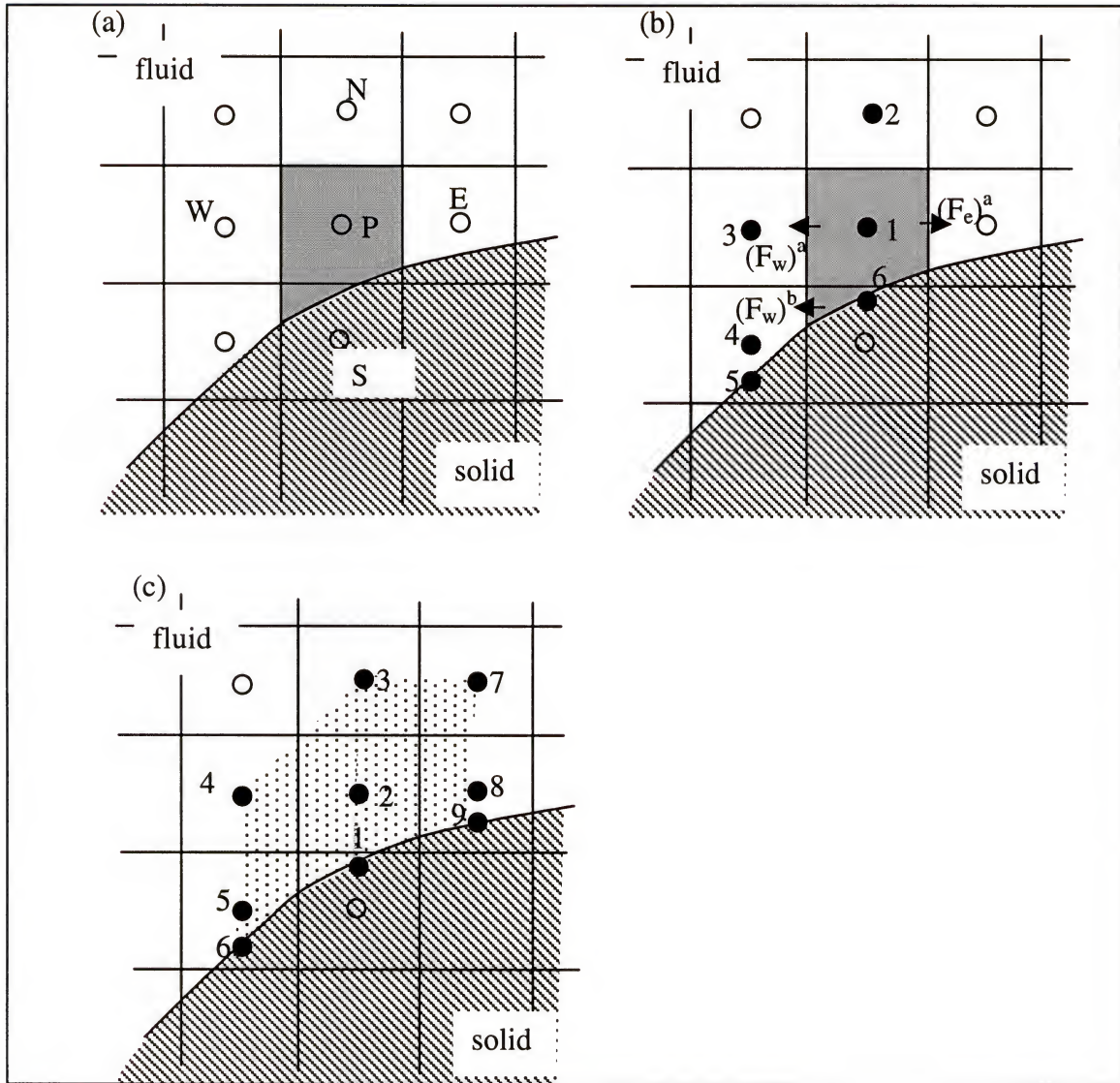


Figure 9. Stencils for evaluation of cell face fluxes. a) Interfacial cell nomenclature showing flux components required in the discrete form of the conservation laws.  $F$  represents the flux (convective/diffusive) at each cell face; b) Stencil points for linear-quadratic interpolation to obtain the flux  $F_w$  and  $F_e$ ; c) All the stencil points used to calculate fluxes for the control volume  $P$ .

To maintain second-order accurate discretization in the boundary cells (Ye et al. 1999), we use a compact two-dimensional polynomial interpolating function which allows us to obtain the fluxes and gradients on the cell faces of the trapezoidal to second-



order accuracy. For instance, for a typical trapezoidal cell shown in Figure 9(a) the interpolating function for a generic variable  $\phi$  has the form

$$\phi = c_1xy^2 + c_2y^2 + c_3xy + c_4y + c_5x + c_6 \quad (20)$$

The unknown coefficients in this interpolant can be expressed in terms of surrounding nodal and boundary values. Using this, the fluxes and gradients on the cell faces can also be expressed in terms of the neighboring nodal and boundary values. For instance, for the lower portion of the west face of the trapezoidal boundary cell shown in Figure 9(b), the value and gradient of  $\phi$  at the face center can be expressed

$$\phi_w^b = \sum_{j=1}^6 \alpha_j \phi_j \quad \text{and} \quad \left( \frac{\partial \phi}{\partial x} \right)_w^b = \sum_{j=1}^6 \beta_j \phi_j \quad (21)$$

where the coefficients  $\alpha$  and  $\beta$  depend on the geometry of the cell and couple the value at the face center to four nodal and two boundary values. Similar expressions can be constructed for the fluxes on the other faces of the trapezoidal boundary cells. These expressions are incorporated into the discrete representation of Equation (15)-(17) and the final discrete equation for any given cell  $P$  is of the form as:

$$\sum_M A_M^P \phi_M = R^P \quad (22)$$

where  $\phi$  is the variable under consideration (velocity or pressure),  $R$  is the source term for the corresponding equation,  $M$  is the size of the stencil and the  $A$ s are the known coefficients that depend on the geometry of the cell and other flow parameters. For a regular, Cartesian cell,  $M = 5$ , whereas for a trapezoidal boundary cell,  $M = 9$ . A typical 9-point stencil for a boundary cell is shown in Figure 9(c). Furthermore, as the stencil in Figure 9(c) indicates, the boundary conditions are directly incorporated into the flux calculation procedure. Cells that lie inside the solid are treated within the framework of



Equation (22) simply by putting  $R^P \equiv 0$  and zeroing out all the coefficients on the left-hand-side of Equation (22) that couple the value of cell  $P$  with the neighboring values.

This interpolation scheme coupled with the finite-volume formulation guarantees that the accuracy and conservation property of the underlying algorithm is retained even in the presence of arbitrary-shaped immersed boundaries. For example, the manner in which the convective and diffusive fluxes are computed at the contiguous faces of adjacent control volumes strictly enforces conservation at these faces (Ye et al. 1999). As pointed out earlier, in convection-dominated flows relatively thin boundary layers are expected to be generated in the vicinity of the immersed boundary. These boundary layers are not only regions of high gradients but are often the most important features of the flow field. Therefore, accurate representation of the conservation laws is especially important in this region. The combination of a finite-volume approach and a locally second-order discretization that is used here is therefore well suited for such flows. This method has now been extended to include moving boundaries and the modifications and additions required in the algorithm to accomplish this are described in the following sections.

### 3.3 Flow Solver with Moving Immersed Boundaries

The objective in the following sections is to describe the Cartesian grid methodology in the presence of moving solid boundaries. The first element in such cases is the determination of the boundary motion and the procedure for coupling the boundary motion with the fluid flow. As mentioned before, the immersed boundary is defined by “marker particles” which are distributed on the boundary surface with a spacing, which is of the same order of magnitude as the grid spacing. Boundary motion is produced by

translating each marker particle with a prescribed velocity. Subsequently, at any time instant, for a given location of these marker particles, a smooth representation of the entire boundary can be constructed by fitting piecewise quadratic polynomials through these particles.

As in the stationary immersed boundary case, a mixed-explicit scheme is used for time-advancement of the governing equations where the convection terms are treated explicitly and the viscous terms implicitly. In cases where there is a two-way interaction between the flow and the moving boundary, a choice also needs to be made regarding the treatment of this coupling. One choice is explicit treatment where the boundary motion and the time-advancement of the flow equations is carried out in a sequential manner. The alternative is implicit treatment wherein the boundary and flow are advanced in time simultaneously in a fully coupled manner. The primary advantage of the implicit approach is that it removes any stability constraints associated with the boundary motion (Tu & Peskin 1992, Hou et al. 1997). This can be crucial in problems where the boundary motion is highly sensitive and closely coupled to the flowfield such as in curvature-driven solidification and capillarity-driven flows. In fact, in the previous work of Udaykumar et al. (1999) which focused on using a Cartesian grid method for solving diffusion controlled dendritic growth, implicit coupling was used and this resulted in a robust solution technique. Implicit coupling however provides no significant advantage when the boundary motion is prescribed independent of the flow field since in this case, the boundary motion is not subject to errors that can grow in time. In fluid-structure interaction problems, where the boundary motion depends on the flow (as for instance in flow-induced vibrations), explicit coupling results in a convective-type stability

constraint on the boundary motion which can be relieved by employing an implicit treatment of the boundary motion. However, since an explicit scheme is being used here for the convective terms in the transport equations, there is no significant advantage to using implicit coupling between the boundary motion and the fluid flow. In the current methodology, an explicit boundary update is therefore used. However, as shown in Udaykumar et al. (1999), if needed, a predictor-corrector approach can be used to implement an implicit coupling in a straightforward manner.

The first step in the time-advancement procedure is to update the location of the boundary. At any given time  $t$ , the immersed boundary is denoted by  $\vec{x} = \vec{\psi}(s, t)$  where  $s$  is the arc length along the boundary measured from a reference point. This is accomplished by advecting the marker particle with the prescribed velocity as follows:

$$\vec{X}_i(t + \Delta t) = \vec{X}_i(t) + \Delta t \vec{u}_i(t + \Delta t) \quad (23)$$

where  $i$  corresponds to the index of the marker particle and  $\vec{u}_i$  is the velocity of this marker particle. The updated position of the marker particles is then used to reconstruct the boundary at time  $(t + \Delta t)$ . Note that in advancing the boundary, the boundary velocity at  $(t + \Delta t)$  is used. As will be pointed out later, this allows for consistency between the boundary velocity and the velocity boundary condition for the fluid.

With the boundary location at  $(t + \Delta t)$  now known, the discretized advection-diffusion equation, Equation (15) can be rewritten as

$$\begin{aligned} \text{St} \left( \frac{\vec{u}^* - \vec{u}^{t+\Delta t}}{\Delta t} \right) \Delta V^{t+\Delta t} = & - \sum_f \frac{1}{2} [3 \vec{u}^t (\vec{U}^t \cdot \hat{n}^{t+\Delta t}) - \vec{u}^{t-\Delta t} (\vec{U}^{t-\Delta t} \cdot \hat{n}^{t+\Delta t})]_f \Delta S_f^{t+\Delta t} \\ & + \frac{1}{2 \text{Re}} \sum_f [(\nabla \vec{u}^t + \nabla \vec{u}^{t+\Delta t}) \cdot \hat{n}^{t+\Delta t}]_f dS_f^{t+\Delta t} \end{aligned} \quad (24)$$

where the superscript  $t + \Delta t$  on the cell volume  $(\Delta V)$ , surface areas  $(\Delta S)$  and normals



$(\hat{n})$  indicates that the values corresponding to the boundary location at time level  $t + \Delta t$ , i.e.  $\vec{x} = \vec{\psi}(s, t + \Delta t)$ , are used in advancing the advection-diffusion equation from  $t$  to  $t + \Delta t$ . Equation (17) for the pressure is reformulated as:

$$\sum_f [\nabla p^{t+\Delta t} \cdot \vec{n}^{t+\Delta t}]_f \Delta S_f^{t+\Delta t} = \frac{St}{\Delta t} \sum_f [\vec{U}^* \cdot \hat{n}^{t+\Delta t}]_f \Delta S_f^{t+\Delta t} \quad (25)$$

As before, the summations in the above equations run over the sides of the given computational cell. Subsequently, the pressure correction is added to the intermediate velocity as shown in Equation (18) and (19).

In keeping with the stationary boundary algorithm, the advection-diffusion Equation (21) is solved with the boundary condition corresponding to the final velocity, i.e.  $\vec{u}_\partial(\psi(s, t + \Delta t), t + \Delta t)$ . This boundary condition is consistent with the boundary motion since the boundary is also moving at this same velocity as shown in Equation (23). Therefore, the no-slip, no-penetration condition is properly imposed at every time step even in the moving boundary case.

The pressure boundary condition also needs to be reformulated for the moving boundary case. For stationary immersed boundaries  $\partial p / \partial n = 0$ , is applied on the immersed boundary. This boundary condition is consistent with the inviscid nature of the pressure correction step and is found to work adequately in most cases. In the moving boundary case, the corresponding pressure boundary condition can be obtained from projecting the inviscid momentum equation in a direction normal to the boundary. This

gives  $\frac{\partial p}{\partial n} = - \left( St \frac{\partial \vec{u}}{\partial t} + \vec{u} \cdot \nabla \vec{u} \right) \hat{n}$  as the boundary condition for pressure. A convenient

means of implementing this boundary condition in the current solver comes from



recognizing that the boundary condition can be recast as  $\frac{\partial p}{\partial n} = -St \frac{D\tilde{u}}{Dt} \cdot \hat{n}$ . The material acceleration (denoted by  $D/Dt$ ) can then be approximated directly from the known boundary velocity and this obviates the approximation of the convective term. For small boundary acceleration, which corresponds to  $St \ll 1$ , this term causes little deviation from the homogeneous Neumann condition for pressure.

It is worth pointing out that the form of Equations (24) and (25) is virtually identical to (15) and (17). The primary difference is that for the trapezoidal boundary cells, the cell volume, surface area and directions of the surface normals are now functions of time. Furthermore, the boundary conditions have to be reformulated in order to account for the time-dependant motion of the immersed boundary. However, unlike Lagrangian methods, time derivatives of the cell volume and surface area do not appear in the equation. In this respect, the simplicity of the Eulerian approach is retained. In the context of the current method, this implies that the discretization of the Equation (24) and (25) at any given time step is virtually identical to the stationary boundary case. Thus, the spatial discretization methodology described in section 3.2 can be used even with moving boundaries. The primary difficulty in the moving boundary algorithm comes from the appearance of “freshly-cleared” cells and this issue is discussed in the next section.

In the present framework, when stationary solid boundaries are embedded in the domain, as with any pressure correction methodology, explicit mass conservation is enforced over the domain boundaries. When deformable solid boundaries are present inside the computational domain, the mass conservation enforced at the domain boundaries should take account of the net mass flux at the moving boundaries caused by

the boundary deformation. The net mass flux arising at the moving interfaces is given by:

$$\dot{m}_{\text{int}} = \sum_{j=1}^{nb} \int_{S_j} \rho \vec{u}_{\partial} \cdot \hat{n} dS \quad (26)$$

where  $nb$  is the number of immersed boundaries and the integral is performed over the surface of the immersed boundary. At each step, the mass deficit over the domain boundaries is evaluated as follows:

$$\dot{m}_{\text{deficit}} = \sum_{j=1}^{ninlets} \dot{m}_j - \sum_{j=1}^{noutlets} \dot{m}_j - \dot{m}_{\text{int}} \quad (27)$$

This mass deficit is distributed evenly at the designated outflow boundary through adjustment of the intermediate velocity boundary condition. In the context of the current study, this deficit correction is applied in the oscillating diaphragm of the synthetic jet actuator. In the case of the oscillating cylinder problem in Section 3.7, no net efflux of mass results at the moving boundary and hence the moving boundary does not have any impact on global mass conservation.

### 3.4 Freshly-Cleared Cells

In sharp interface methods, such as the present one or those presented by Bayyuk et al. (1993) and Leveque and coworkers (Beyer & Leveque 1992, Leveque & Li 1994), the issue of change of material needs to be addressed. This arises when a computational point (as in Figure 10), which was in the solid at one time-step, emerges into the fluid at the next time-step. In Leveque and Li (1994), the issue of a discontinuity in time at cross-over is dealt with by applying a jump condition in time to the time-derivative term on the LHS of equations such as Equation (24). For certain problems, this temporal jump

condition is physically clear. For instance, in solidification problems, the temporal jump condition for the enthalpy in a given control volume is simply the latent heat released within that volume. In the present fluid-structure interaction problem, such a physics-based jump condition is not available for the velocity field. Since the cell  $P$  was previously in the solid, it had no history in the fluid phase and there is no physically realizable value of  $\vec{u}_{i,j}^t$ . Thus, Equation (24) is not applicable for such cells.

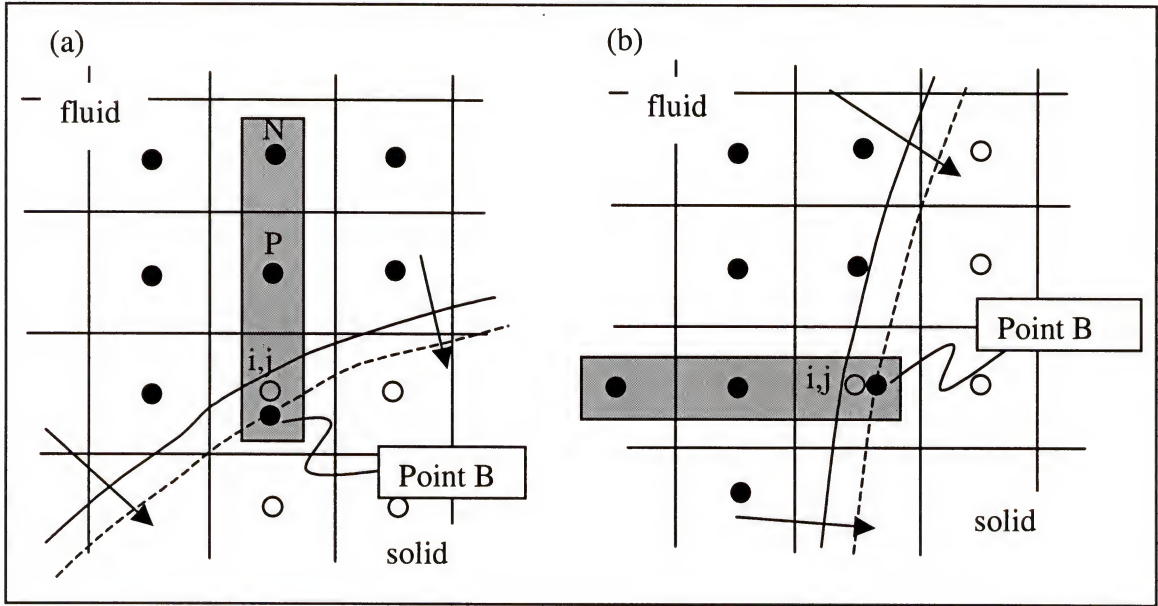


Figure 10. Change of material as the immersed boundary traverses the mesh. a) Configuration in which the interface is nearly horizontal; b) Configuration in which the interface is nearly vertical.

In the current method an approach which is similar to that used in the finite-difference method of Udaykumar et al. (1999) is used. This consists of temporarily merging the freshly cleared cell with a neighboring cell and is analogous to the approach taken in moving grid formulations when a new cell is inserted following mesh refinement. In the current finite-volume based methodology, this cell-merging is realized through a simple one-dimensional interpolation operation and this can be explained here



for the particular freshly-cleared cell shown in Figure 10. For this cell, the following interpolant is used:

$$u^*(y) = a_0 + a_1 y + a_2 y^2 \quad (28)$$

where, the coefficients  $a_0$ ,  $a_1$  and  $a_2$  are coefficients that depend on the value of  $\vec{u}^*$  at  $P$ ,  $N$  and the boundary location  $B$ , and the corresponding locations of these points. A similar procedure can be followed for the situation illustrated in Figure 10(b). The above dependance can therefore be recast in the following form:

$$\sum_M B_M^P u_M^* = 0 \quad (29)$$

and for this cell, Equation (29) replaces the discretized advection-diffusion Equation (24). Note that Equation (29) is applied only at the instant when there is a cross-over. Following that instant, Equation (24) is again used to time-step the  $\vec{u}^*$  field. Note that since pressure depends only on the  $\vec{u}^*$  field, Equation (25) is still valid for these cells as long as  $\vec{u}^*$  can be computed through some appropriate means, such as Equation (29).

### 3.5 Fast Solution of Discretized Equations

The general form of the discretized equations to be solved at each time-step is given in Equation (24). The term on the left-hand side of this equation represents a discretized Helmholtz operator in the case of the advection-diffusion equation and a Laplacian operator in the case of the pressure Poisson equation. The standard alternating-direction line successive-overrelaxation (SOR) proves extremely effective for the solution of the discretized advection-diffusion equation and the residual can be reduced to acceptable levels within a few iterations. However, the discretized pressure Poisson equation (PPE) exhibits significantly slower convergence. In fact, due to its slow



convergence, the solution of the discretized pressure equation is usually the most time-consuming part of a fractional-step algorithm. In the presence of immersed boundaries this behavior of the pressure equation can be further exacerbated since the discrete operator for the trapezoidal cells requires a stencil, which leads to significant dependence on neighbors, which are not included in the line-SOR, sweeps. For example, in Figure 9(c) the coupling of cell with its northeast and southwest neighbor is not included directly in any of the line-sweeps. Furthermore, discretization in the irregularly shaped boundary cells results in weaker diagonal dominance than in the regular cells and this has a deleterious effect on the convergence of any iterative scheme.

In Ye et al. (1999), a line-SOR preconditioned BiCGSTAB iterative method was used and it was found to be significantly faster than a simple line-SOR algorithm. Furthermore, for the stationary boundary problems that were simulated there, it was found that this iterative method allowed us to obtain the solution of most problems in a reasonable amount of time. However, BiCGSTAB is found to be inadequate when applied to moving boundary problems. As the boundaries move, the geometry of the domain changes and the elliptic nature of the PPE induce global readjustments of the pressure field. Thus, changes in the pressure field for moving boundary problems can be more significant than for the stationary boundary cases. Thus, the pressure from the previous time step is a much poorer guess for boundary cells in the moving boundary case than it is in the stationary boundary case. Consequently, the starting residual for the PPE in the boundary cells is generally higher in the moving boundary case and considerable effort is therefore required to reduce these to acceptable levels. This solver

employs multigrid method (Wesseling 1992) to solve PPE. The employment of multigrid was proved to increase the performance of this solver.

### 3.6 Overall Solution Procedure

Given the velocity and pressure field and interface position at time  $t$ , the overall solution procedure to advance the solution to  $t + \Delta t$  is as follows:

- 1) Advance the immersed boundary to its position at  $t + \Delta t$  as described in section 3.3.
- 2) Determine the intersection of the updated immersed boundary with the Cartesian mesh and using this information, reshape the trapezoidal boundary cells.
- 3) Update the discrete expressions corresponding to Equation (24) for the boundary cells including freshly cleared cells.
- 4) Advance the discretized equations in time:
  - a. Solve for intermediate velocity field  $\vec{u}^*$ .
  - b. Solve for pressure from Equation (27) using the multigrid technique.
  - c. Correct the velocity field as in Equation (18)-(19) to obtain velocity field at  $t + \Delta t$ .

This completes the description of the current simulation methodology. It should be pointed out that although the methodology has been described only in the context of 2-D geometries, the approach developed here can be extended to three-dimensions. The key aspects to be addressed in extending this methodology to 3-D are efficient methods for representing curved 3-D interfaces and reconstructing boundary cells (Jayaraman et al. 1997, Khanna 2000). Apart from these aspects, the discretization procedure described here carries over into 3D in a straightforward way. In the following sections the focus is on examining the performance of the multigrid algorithm, validating the solution

methodology by comparing computed results with experiments and demonstrating the capabilities of the method for simulating flows with complex immersed moving solid boundaries.

### 3.7 Validation of the Solver

The solver used in our simulation has been developed recently. Thus, it was felt necessary to validate the solver for a moving boundary case before using it in our study. Here we have validated the solver by simulating flow past a transversely oscillating cylinder and the associated phenomenon of vortex shedding “lock-on”. Vortex shedding “lock-on” is a classical phenomenon that is observed in the wake of bluff bodies and refers to the situation where the frequency of vortex shedding in the wake synchronizes or locks on to the frequency of an imposed perturbation. The perturbation could be imposed through pulsation of the incoming flow (Griffin & Hall 1995) or by free (Mittal & Kumar 1999) or forced vibration (Koopmann 1967) of the bluff body immersed in a steady oncoming flow. In particular, vortex-shedding lock-on past a transversely oscillating cylinder has been studied extensively and is a good benchmark case to validate the current methodology. Here we have simulated flow past a cylinder at  $Re = 200$  undergoing sinusoidal transverse oscillation over a range of amplitudes and frequencies and direct comparison of the computed results is made with the experiments of Koopmann (1967) and simulations of Meningini and Bearman (1993).

The computational domain and grid used for the current simulations is shown in Figure 11. All lengths here have been normalized by the cylinder diameter  $D$ . As can be seen in the Figure 11, a relatively large computational domain of size of  $30 \times 30$  is used for the current simulation and the mean location of the cylinder center  $(x_0, y_0)$  is (10,15)



relative to the left bottom corner of the domain. A uniform free stream velocity ( $U_\infty$ ) is prescribed on the inflow (left), top and bottom boundaries and a convective boundary condition is used at the exit (right) boundary. The cylinder is oscillated sinusoidally such that the location of its center ( $x_c, y_c$ ) is given by

$$x_c(t) = x_o; \quad y_c(t) = y_o + A \sin(2\pi f_f t)$$

where  $t$  is the time non-dimensionalized by  $D/U_\infty$  and  $A$  and  $f_f$  are the non-dimensional amplitude and frequency of the oscillation respectively. As shown in Figure 11, a nonuniform mesh is used in the simulation wherein enhanced resolution is provided in the cylinder vicinity and in the wake. In the vertical direction, enhanced resolution is provided up to three diameters on either side of the nominal cylinder location, which is adequate to cover the near wake for all the oscillation amplitudes studied here. The cylinder is immersed and oscillates through the fixed, nonuniform, Cartesian mesh.

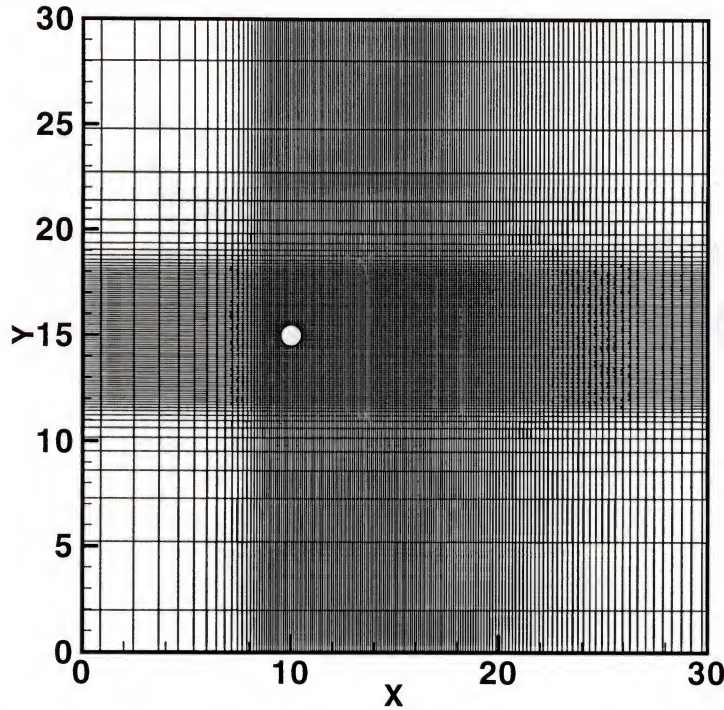


Figure 11. Nonuniform mesh used in the oscillating cylinder simulations. Only every other grid line is shown in both directions.

As a first step, flow past a stationary circular cylinder at  $Re = 200$  has been simulated. The flow at this Reynolds number exhibits classical Karman vortex shedding and the current simulation has been continued for about 40 shedding cycles beyond the point where it reaches a stationary state. The vortex-shedding frequency was computed from the variation of the velocity components in the near wake and based on this, a non-dimensional vortex shedding frequency of (or Strouhal number)  $f_0 = 0.198$  was obtained. This value matches well with the experiments of Williamson (1996) who obtained a Strouhal number of 0.197. Furthermore, the average value of computed drag coefficient was 1.38 and this matches well with the numerically calculated value in Braza et al. (1986). The flow field from this stationary cylinder simulation was used as the initial condition for all oscillating cylinder simulations.

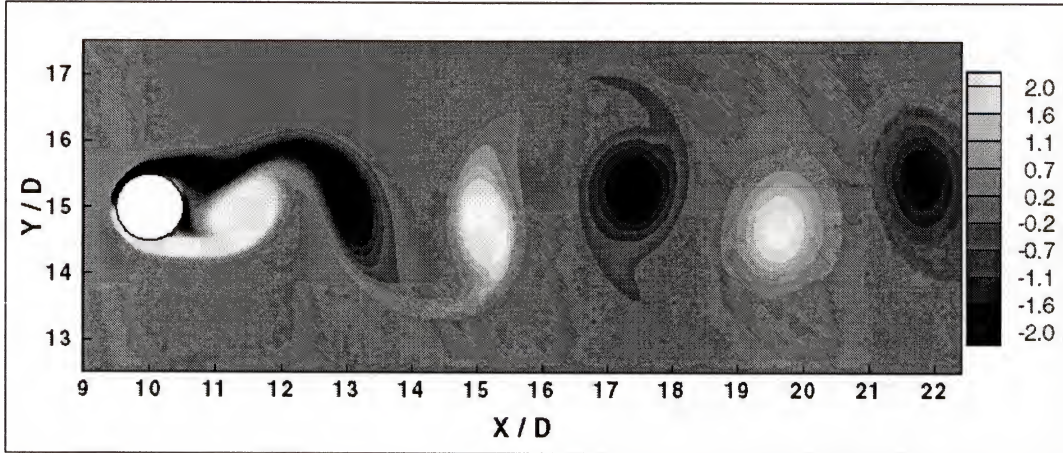


Figure 12. Contour plot of spanwise vorticity showing the shedding of vortices for a fixed cylinder.

In the current study, two sequences of simulations have been carried out at fixed amplitudes ( $A/D$ ) of 0.1 and 0.2 and the frequency varied systematically over a range around the natural vortex shedding frequency ( $f_0$ ). Each of these simulations is integrated in time for about 200 nondimensional time units, which is sufficient to reach a



stationary state. Subsequently, the equations are integrated further for about  $200D/U_\infty$  and the vortex shedding frequency is determined by computing the frequency spectra of the velocity fluctuation in the near wake over this period of time. The solid line in Figure 13(a) shows the vortex shedding lock-on region in the space defined by the oscillation frequency (x-axis) and amplitude (y-axis), as determined experimentally by Koopmann (1967) for  $Re = 200$ . According to this figure, lock-on is observed for amplitudes higher than 0.05 and the frequency range over which lock-on occurs increases with oscillation amplitude.

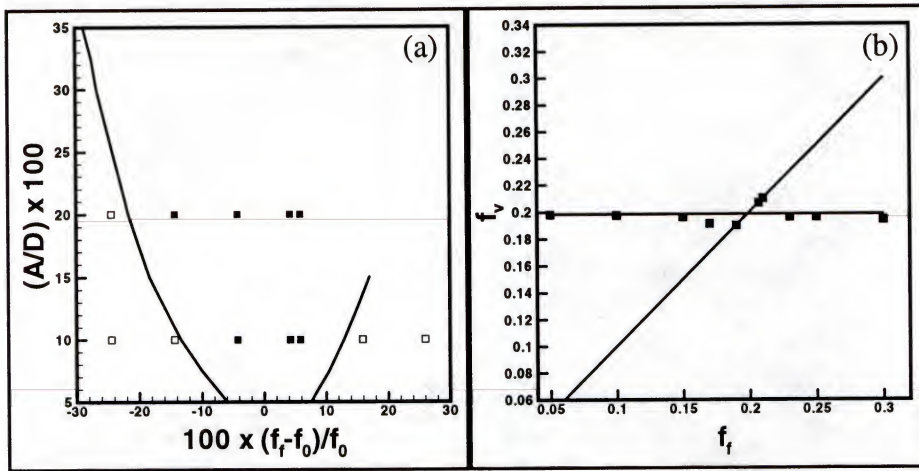


Figure 13. Comparison of the result from the current study and the result from other studies. a) Lock-in range determined by Koopmann (1967) shown by the solid lines. Results from current simulations are in squares. Filled squares indicate lock-on; b) Variation of vortex shedding frequency with forcing frequency for  $A = 0.10$ .

Figure 13(b) shows the variation of the vortex shedding frequency in the wake of the cylinder for  $A/D = 0.1$  for a range of cylinder oscillation frequencies. The horizontal line in the plot corresponds to the natural shedding frequency and the 45 degree inclined line represents the situation of lock-on where the shedding frequency matches the oscillation frequency. Our simulations indicate that vortex shedding lock-on occurs for



oscillation frequencies of  $0.95 f_0$  and  $1.05 f_0$ . As the oscillation frequency is decreased below  $0.95 f_0$ , the vortex shedding decreases monotonically and approaches the natural shedding frequency. A somewhat different behavior is observed as the frequency is increased beyond  $1.05 f_0$ . We observe that as the frequency is increased, the vortex shedding frequency rapidly drops to a value below the natural shedding frequency and then approaches this value as the oscillation frequency is increased further. A similar behavior in the frequency has been observed by Moretti (1993) and Stansby (1976). The results of our simulations are superposed on the plot in Figure 13(a) and we find that the lock-on behavior predicted in our simulations is in-line with the experiments of Koopmann (1967). Four simulations have also been carried out with  $A/D = 0.2$ . The results of these simulations have also been plotted in Figure 13(a) and are found to be in-line with the experiments. Figure 14 shows a series of vorticity contour plots for one of the lock-on cases. This case has the amplitude ratio ( $A/D$ ) of 0.2 and the forcing frequency of  $1.05 f_0$ .

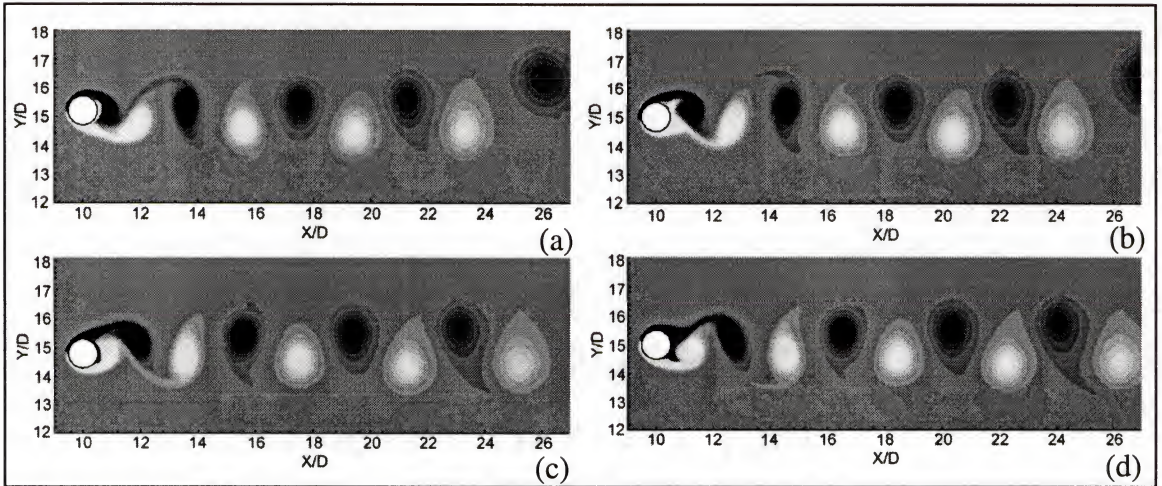


Figure 14. Series of the vorticity contour plots for a lock-on case with  $A/D = 0.2$  and  $f_f = 1.05 f_0$ .

Finally, one simulation has been carried out with  $A/D = 0.33$  and a forcing frequency of 0.15872. Meningini and Bearman (1993) have simulated this flow using a vortex method and have found that for these parameters, three vortices are shed in the wake for each shedding cycle. Figure 15 shows a contour plot of the spanwise vorticity obtained from our simulation at one time instant and we also observe two clockwise and one anti-clockwise vortices being shed per cycle of the cylinder oscillation. Thus, the current simulations confirm the experimental observations of Koopmann (1967) and also match the computational results of Meningini and Bearman (1993) thereby providing further validation of the current simulation methodology.

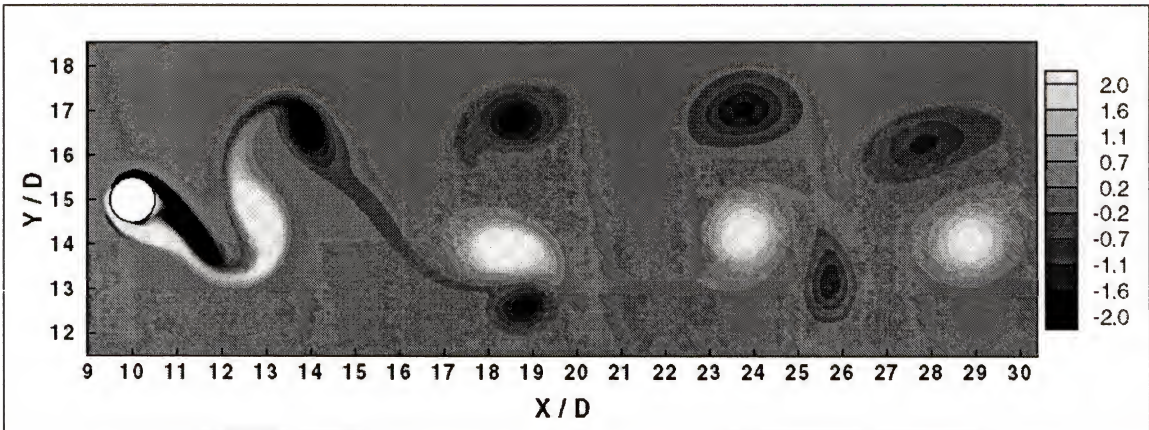


Figure 15. Contour plot of spanwise vorticity showing the shedding of three vortices per shedding cycle for  $A = 0.33$  and a forcing frequency of 0.15872.



## CHAPTER 4 RESULTS

### 4.1 Computational Aspect

Figure 16 shows the computation domains used in the current study. Figure 16(a) is for cases with the quiescent external flow case and Figure 16(b) is for cases with external flow. In both configurations, the actuator cavity is at the bottom part of the domain. In the boundary-layer cases, the boundary condition on the left side of the domain is the inlet prescribed by an approximated form of Blasius boundary layer over the flat plate.

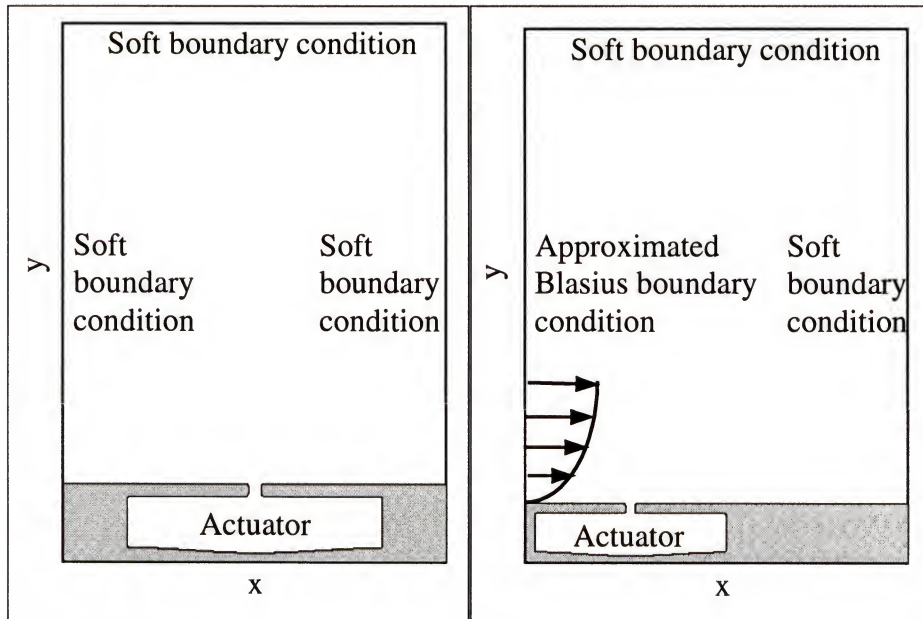


Figure 16. Computation domain and boundary conditions. a) Quiescent external flowcases; b) Blasius boundary-layer cases.

For  $y < \delta$ , velocity is prescribed as



$$\frac{u}{U_{\infty}} = f\left(\frac{y}{\delta}\right) = f(\eta) = \frac{3}{2}\eta - \frac{1}{2}\eta^3 \quad (30)$$

For  $y > \delta$ , velocity is simply the freestream velocity  $U_{\infty}$ . The top boundary of the domain is prescribed to have

$$\frac{\partial u}{\partial y} = \frac{\partial v}{\partial y} = 0$$

The right side of the domain is the outlet with the zero velocity gradient. Boundary conditions for the external quiescent flow cases are all prescribed as the soft boundary so the direction of the flow depends on the actuator.

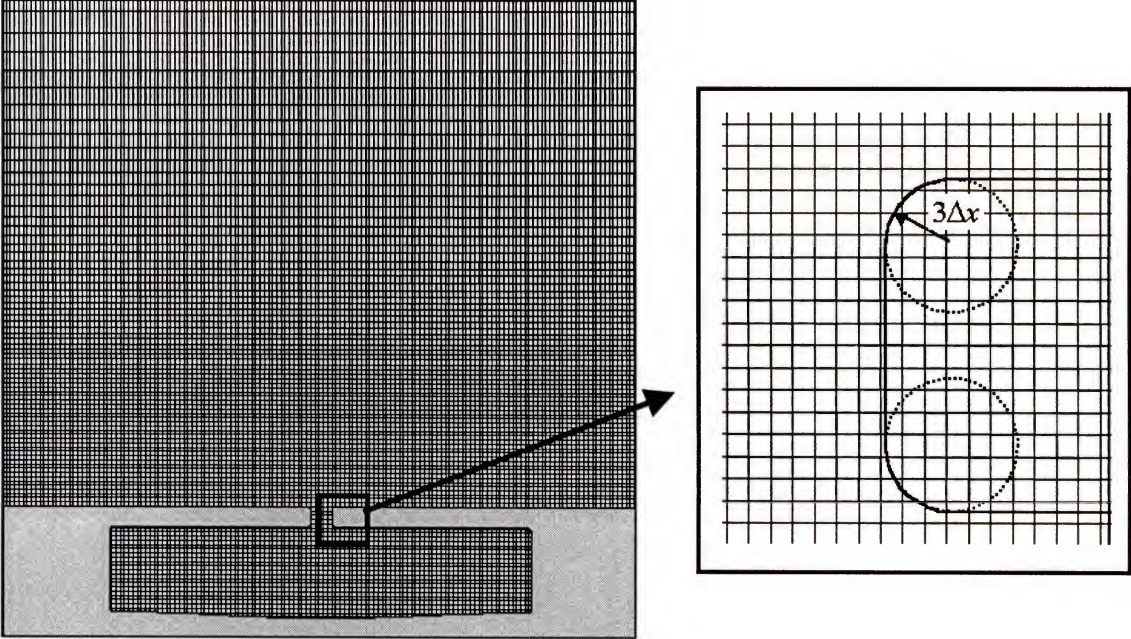


Figure 17. Fixed nonuniform Cartesian grid used in the synthetic jet calculation. Only every third grid points is shown.

Figure 17 shows a close up in the cavity region of a grid used in the simulations. The grid is uniform in the x-direction. In the y-direction, the uniform area covers the bottom part of the calculation domain and extends to about one cavity height above the flat plate. The grid is non-uniform for the rest of the domain in the y-direction. We use

different stretching ratios between the quiescent external flow case and the boundary-layer case. In the quiescent flow case, the stretching ratio is small because the jet generated by the actuator travels in the vertical direction, so the flow features in this direction must be represented with enough resolution. In the external boundary-layer cases, we can use higher stretching ratio because the jet generated by the actuator is convected downstream of the orifice. The flow well outside boundary layer remains almost the same. This allows us to save grid points in the y-direction. For some external flow cases in which the size of recirculation bubble is relatively large compared to the size of the cavity, the grid in the x-direction is uniform to cover the cavity region and it is stretched out slowly downstream of the cavity. The location of the cavity is also different between the quiescent flow cases and boundary-layer cases. Since the flow is symmetric in quiescent flow cases, we place the actuator at the center of the bottom domain. In the boundary-layer cases, the actuator is placed closed to the left side of the domain so that the outflow is located about  $30d$  downstream of the slot. Typically, the number of grid points in the x- and y-directions is about  $600 \times 220$ , and the number of grid point across the actuator slot is about 16. All edges in the synthetic jet actuator are rounded off as shown in Figure 17 since sharp corners cannot be correctly resolved by solvers. The fillet radius of these rounded off edges is equal to three times the grid spacing in the vicinity of the slot. Table 1 shows all the cases and parameters of simulations performed in the current study. The other parameters are fixed at the following values.

$$W/H : \quad \text{width to height ratio of cavity} \quad = 5$$

$$W/d : \quad \text{cavity width to slot width ratio} \quad = 20$$

$$S : \quad \text{Stokes number} \quad = 10$$



Table 1. Simulations and parameters in the current study.

Case	$A/H$	$h/d$	$Re_\delta$	$\delta/d$	$Re_d$	$V_{ave}^{inv}/U_\infty$	$V_{ave}^{inv}d/U_\infty\delta$
1	0.025	1/3	0	NA	63	NA	NA
2	0.050	1/3	0	NA	125	NA	NA
3	0.075	1/3	0	NA	187	NA	NA
4	0.100	1/3	0	NA	250	NA	NA
5	0.025	1	0	NA	63	NA	NA
6	0.050	1	0	NA	125	NA	NA
7	0.075	1	0	NA	187	NA	NA
8	0.100	1	0	NA	250	NA	NA
9	0.025	3	0	NA	63	NA	NA
10	0.050	3	0	NA	125	NA	NA
11	0.075	3	0	NA	187	NA	NA
12	0.100	3	0	NA	250	NA	NA
13	0.025	5	0	NA	63	NA	NA
14	0.050	5	0	NA	125	NA	NA
15	0.075	5	0	NA	187	NA	NA
16	0.100	5	0	NA	250	NA	NA
17	0.025	1	254	5	63	1.25	0.25
18	0.050	1	254	5	125	2.50	0.50
19	0.075	1	254	5	187	3.75	0.75
20	0.100	1	254	5	250	5.0	1.0
21 (wide)	0.100	1	254	5	250	5.0	1.0
22	0.025	1	254	2	63	0.5	0.25
23	0.050	1	254	2	125	1.0	0.50
24	0.075	1	254	2	187	1.50	0.75
25	0.100	1	254	2	250	2.0	1.0
26	0.100	3	254	2	250	2.0	1.0
27	0.100	1	400	2	250	1.25	0.625
28	0.100	1	800	2	250	0.625	0.3125
29	0.025	1	1200	2	63	0.105	0.0525
30	0.375	1	1200	2	94	0.157	0.0783
31	0.050	1	1200	2	125	0.2084	0.1042
32	0.0625	1	1200	2	156	0.26	0.130
33	0.075	1	1200	2	187	0.31	0.155
34	0.100	1	1200	2	250	0.416	0.208
35	0.025	1	2600	2	63	0.048	0.024
36	0.375	1	2600	2	94	0.072	0.036
37	0.050	1	2600	2	125	0.096	0.048
38	0.0625	1	2600	2	156	0.120	0.060
39	0.075	1	2600	2	187	0.142	0.071
40	0.100	1	2600	2	250	0.192	0.096



## 4.2 Vortex Dynamics

In this subsection, we provide a description and comparison of some selected cases. These cases are selected to highlight the effect of key parameters on the jet flow. The discussion in this section is mainly qualitative in nature. More quantitative analysis of the jet will be undertaken in subsequent sections and chapters.

### 4.2.1 Quiescent External Flow Cases

First, we describe the vortex dynamics of the quiescent external flow cases. Such configuration was studied in the past by other groups (James et al. 1994, 1996, Kral et al. 1997, Rizzetta et al. 1998). Our objectives in describing these cases are twofold. First, we intend to systematically examine the effects of various parameters on the jet and this has not been done in past studies. Second, the quiescent flow case forms a good baseline for future discussion of jets in external cross flow. In these cases, the jet flow is expected to be strongly dependent on  $Re_d$ ,  $h/d$  and  $S$ . Here we fix the value of  $S$  to 10 and examine the effect of varying  $Re_d$  and  $h/d$  on the vortex dynamics of the resultant jet.

#### 4.2.1.1 Effect of jet Reynolds number

In this subsection, we compare the effect of jet Reynolds number on the vortex dynamic. The jet Reynolds number is varied by changing the diaphragm amplitude, while the  $h/d$  for all the cases in this subsection is equal to unity. Figure 18 shows a series of spanwise vorticity contour plots for the smallest jet Reynolds number ( $Re_d = 63$ ) in the current study and this corresponds to  $A/H = 0.025$ . For all cases, we show a sequence of four vorticity plots. The first is at the maximum expulsion stage where the diaphragm is in the neutral position and moving up. The second is the minimum volume case where the diaphragm is at the top most position. This results in the minimum

volume of the actuator cavity. The third plot is the maximum ingestion where the diaphragm is in the neutral position and moving down. The last stage is the maximum volume where the diaphragm is in the bottom most position thus the actuator cavity volume reaches its maximum.

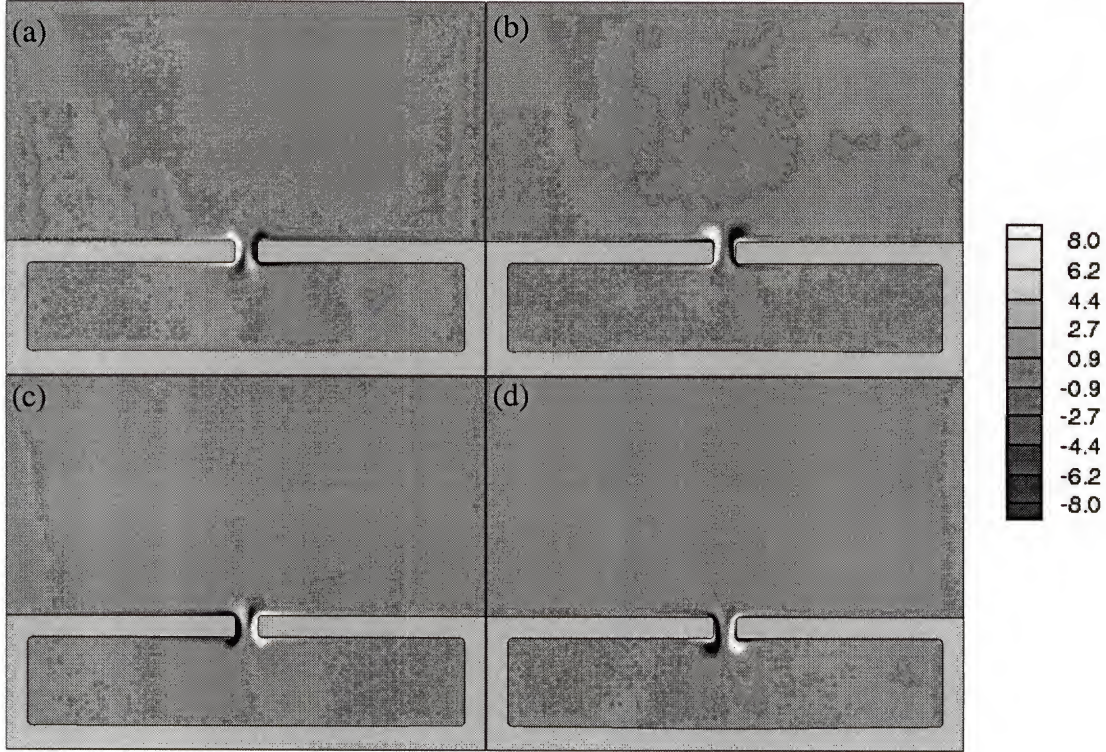


Figure 18. Vorticity contour plots for quiescent external flow,  $h/d = 1$  and  $Re_d = 63$  ( $A/H = 0.025$ ). a) Maximum expulsion; b) Minimum volume; c) Maximum ingestion; d) Maximum volume.

At the maximum expulsion stage, we observe that the boundary layer that forms on the inside walls of the slot curls around the lip of the slot and show some indication of rolling up into vortices. At the minimum volume stage, the separated vorticity layer has rolled up into small but distinct vortices, which are still attached to the vorticity layer. Furthermore, the boundary layer separates at the lower lip of the slot and detaches from the inner walls of the slot. The ingestion stage starts beyond this and by the time the



maximum ingestion stage is reached (Figure 18(c)) a vortex pair similar to that seen in Figure 18(a) is now seen forming in the inside cavity at the lip of the slot. Furthermore, the two vortices that rolled up outside the slot are ingested back through the slot. During this ingestion process, the mean shear field is such as to lead to cancellation of vorticity and a rapid decrease in the strength of the vortices. By the maximum volume stage, the two vortices that form inside the cavity look the same as the one outside in Figure 18(b). Furthermore, the ingested vortices have been completely cancelled out. Note that the inside vortices are later expelled out and these also are cancelled out as they pass through the slot and this can be seen in Figure 18(a).

Figure 19 shows the result for the next case for which  $Re_d = 125$  ( $A/H = 0.05$ ). This slot flow Reynolds number is twice that of the previous cases and with this increase in jet Reynolds number, a significantly different jet formation process is observed. As the diaphragm reaches the maximum expulsion stage, the slot wall boundary layer is again observed to separate from the lip of the slot and rolls up into two vortices. This process is qualitatively similar to the previous case. However, at the next stage (i.e., minimum volume) the two vortices are found to have grown to a larger size and have also separated from the slot wall vorticity layer. We hypothesize that the vortex pair, because of its higher strength produce a larger self-induced velocity that convects the vortex pair slightly away from the lip of the slot. Thereafter, the ingestion flow, which moves along the flat plate wall into the slot, acts to separate these vortices from the slot wall vorticity layer. As the cycle continues, the motion of the separated vortex pair is governed by the competition between the self-induced velocity, which is in the positive  $y$ -direction, and the slot flow, which is in the negative  $y$ -direction. At this particular jet Reynolds number,



the self-induced velocity is marginally dominant and the vortex pair does exhibit a net convection in the positive  $y$ -direction. However, the vortex pair is still close enough to the slot that it is immersed in the shear flow created by the ingestion and this tends to rapidly diminish the strength of the vortex pair. The vortex pair thus is found to move vertically upward and dissipate rapidly. Also worth noting is the fact that the vortices formed inside the cavity are stronger and convect down and impact on the diaphragm thereby creating vortical flow in the cavity.

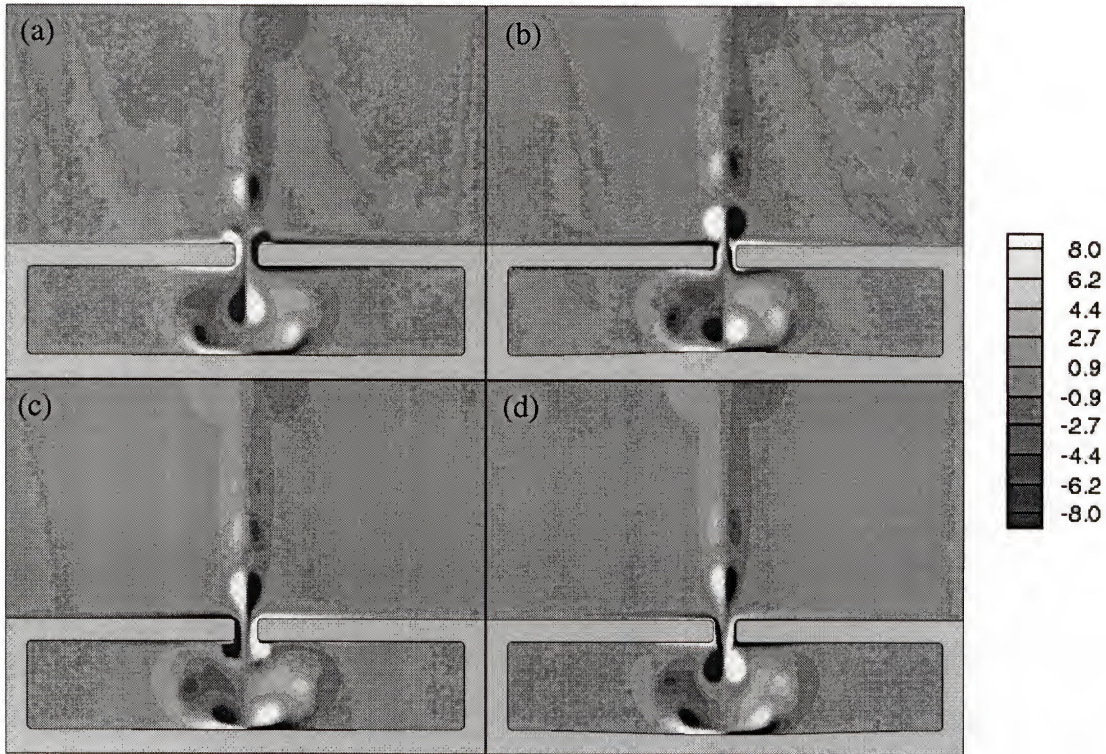


Figure 19. Vorticity contour plots for quiescent external flow,  $h/d = 1$  and  $Re_d = 125$  ( $A/H = 0.05$ ). a) Maximum expulsion; b) Minimum volume; c) Maximum ingestion; d) Maximum volume.

The next case for which the plots are shown in Figure 20 has  $Re_d = 187$  ( $A/H = 0.075$ ). Thus, the mean jet exit velocity is three times that of the first case. This is the first case for which we observe a well-developed jet comprising a train of vortex pairs.



With the higher jet velocity, the strength of the vortices is also higher and by the minimum volume stage, the vortices formed outside the slot are large and have moved a larger distance away from the slot. By the time the ingestion phase begins, the vortices are more than one slot width away from the slot and are not affected as much by the flow set up by the ingestion process. The vortex pair continues to convect in the vertical direction due to self-induced velocity, and the strength of the vortices diminishes slowly due to viscous effects. Inside the cavity, the vortices from each cycle impact the diaphragm and form a complex system of vortices. However, it should be noted that the pattern inside the cavity remains symmetric about the vertical centerline.

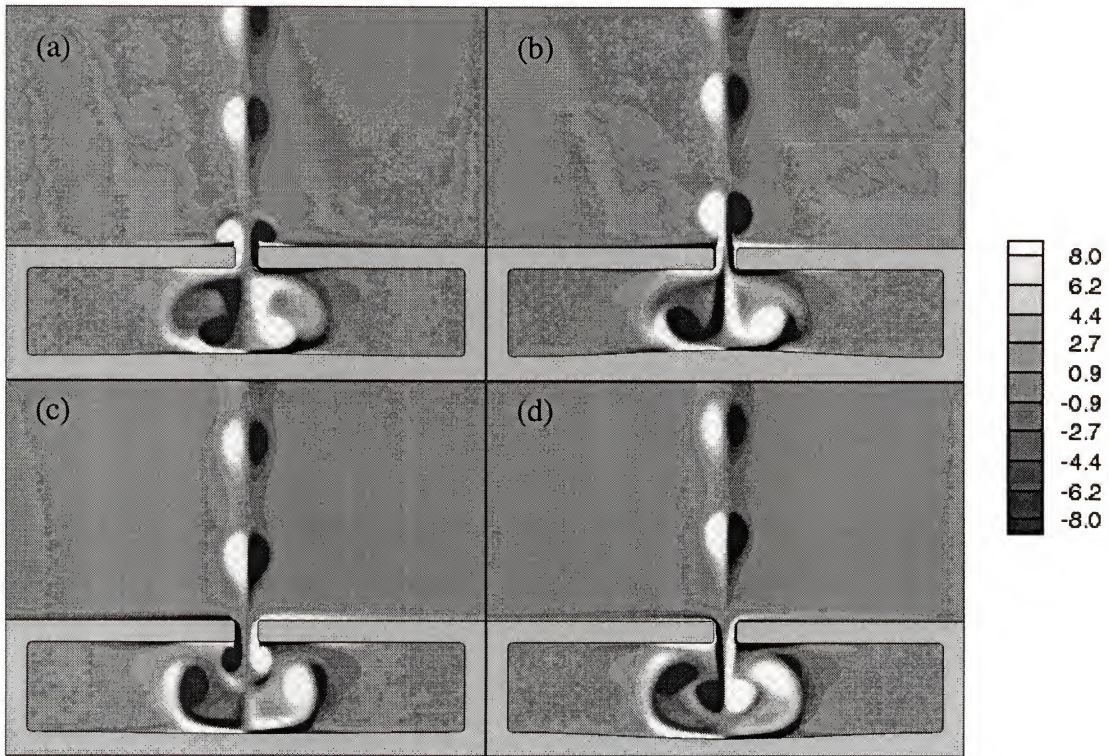


Figure 20. Vorticity contour plots for quiescent external flow,  $h/d = 1$  and  $Re_d = 187$  ( $A/H = 0.075$ ). a) Maximum expulsion; b) Minimum volume; c) Maximum ingestion; d) Maximum volume.



The final case in this subsection corresponds to  $Re_d = 250$  ( $A/H = 0.1$ ), which is the highest, jet Reynolds number case simulated in this study. Vorticity contour plots for this case are shown in Figure 21. The flow looks qualitatively similar to the previous case although the vortices in this case are larger in size and strength. A complex but symmetric flow is set up inside the cavity and it is interesting to note that despite the large magnitude, a large portion of the cavity remains virtually unaffected by the vortex structure. The regions that are adjacent to the two side walls of the cavity contain almost stagnant fluid and do not seem to play an active role in the jet formation process.

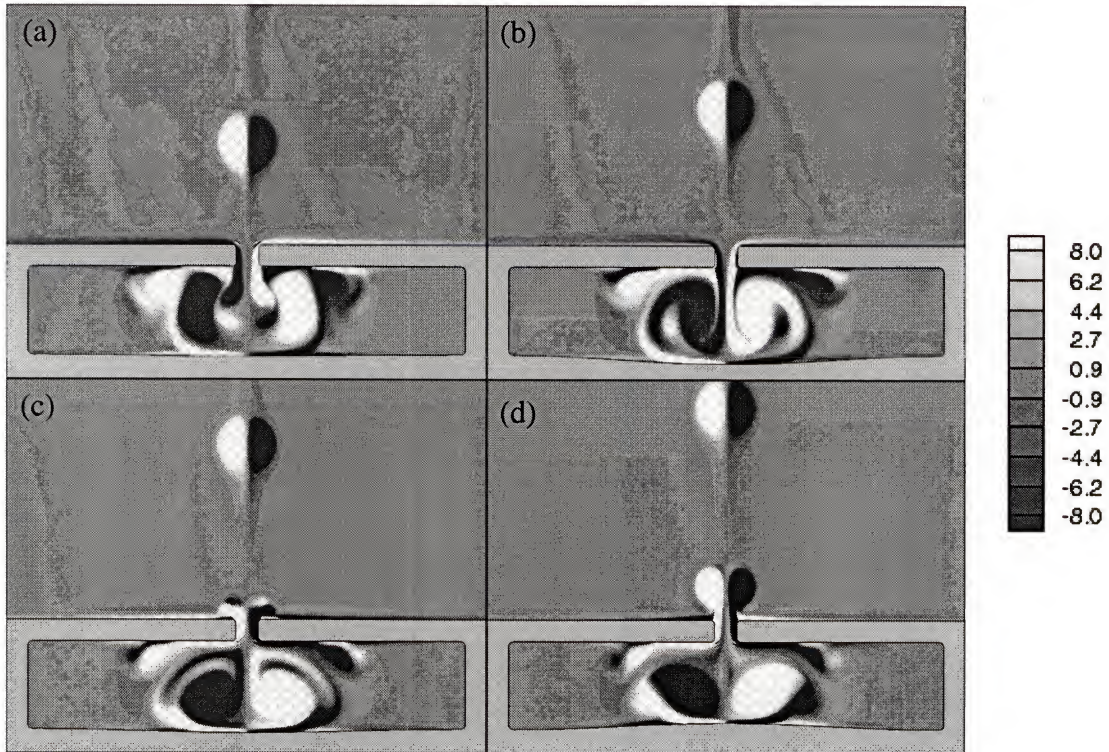


Figure 21. Vorticity contour plots for quiescent external flow,  $h/d = 1$  and  $Re_d = 250$  ( $A/H = 0.1$ ). a) Maximum expulsion; b) Minimum volume; c) Maximum ingestion; d) Maximum volume

As we can see in this section, the formation of the vortex train is observed only in cases, in which the jet velocity (and therefore  $Re_d$ ) is sufficiently large. However, it



cannot be construed from this that  $Re_d$  is the sole parameter that determines whether a jet will be synthesized. Our observations indicate that the jet formation depends on the induced velocity of the vortex pair that rolls up near the slot. High induced velocity convects the vortices away from the slot before they are trapped by the ingestion cycle. Since the induced velocity of a vortex pair depends on the strength of the individual vortices, it therefore stands to reason that the vortex strength will play an important role in the formation of the jet. Now the vortex strength can be related directly to the flux of vorticity by the slot flow over the expulsion stroke. If  $\Omega_v$  denotes the vortex strength then

$$\Omega_v \sim \int_0^{T/2} \int_0^{\delta_s} \omega_z v_J dx dt$$

where  $\delta_s$  is the boundary layer thickness of the flow through the slot, and  $v_J$  is the jet velocity. The vorticity in the slot boundary layer can further be estimated as

$$\omega_z \sim \frac{V_{ave}^{inv}}{\delta_s},$$

and therefore  $\Omega_v$  can be estimated as

$$\Omega_v \sim \frac{V_{ave}^{inv}}{\delta_s} V_{ave}^{inv} \delta_s \frac{1}{\omega},$$

Now assuming that  $V_{ave}^{inv}$  is the characteristic jet velocity, the above expression can be rearranged to give

$$\frac{\Omega_v}{V_{ave}^{inv} d} \sim \frac{Re_d}{S^2}$$

This final equation suggests that the vortex strength generated through the jet slot might scale with  $Re_d/S^2$ . However, since the variation of  $S$  is not covered in the current study, we cannot verify this hypothesis. We suggest that the validation of this hypothesis be undertaken in the future.

#### 4.2.1.2 Effect of $h/d$

In this section, we examine the effect of the parameter  $h/d$  on the vortex dynamics of the jet. For this, we have chosen to compare the cases with  $h/d = 1/3, 1, 3$  and  $5$  all of which compared to  $Re_d = 250$  ( $A/H = 0.1$ ), which is the highest amplitude simulated here.

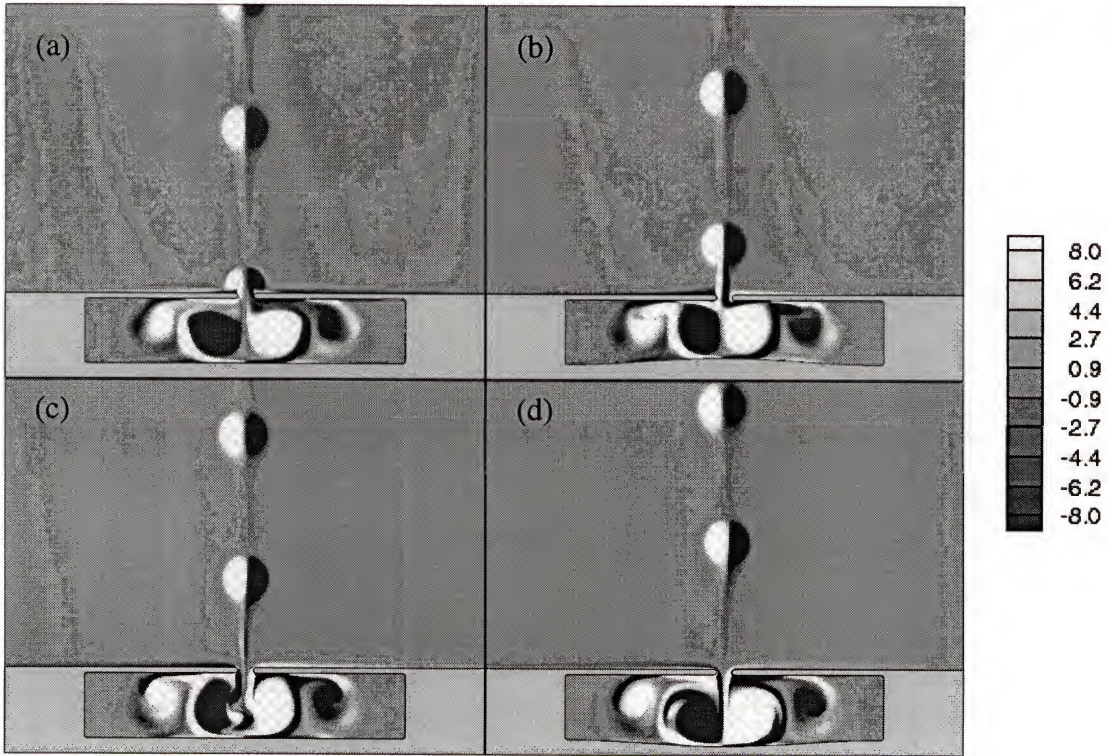


Figure 22. Vorticity contour plots for quiescent external flow,  $h/d = 1/3$  and  $Re_d = 250$  ( $A/H = 0.1$ ). a) Maximum expulsion; b) Minimum volume; c) Maximum ingestion; d) Maximum volume.

Note that in a practical separation control application,  $h/d$  will depend on how the synthetic jet is embedded into the wing and on factors such as the thickness of the



skin of the wing. Therefore, it is relevant to examine how this parameter affects the jet flow and in the current study, we have investigated the affect over a 15 fold range of this parameter.

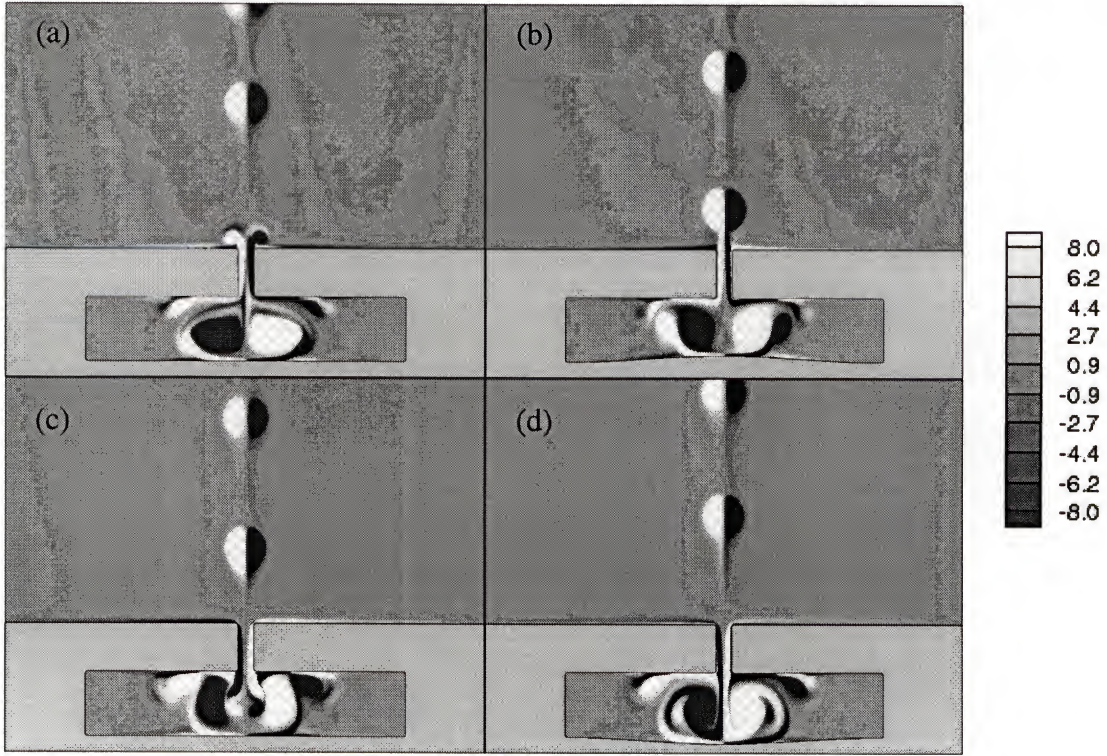


Figure 23. Vorticity contour plots for quiescent external flow,  $h/d = 3$  and  $Re_d = 250$  ( $A/H = 0.1$ ). a) Maximum expulsion; b) Minimum volume; c) Maximum ingestion; d) Maximum volume.

In Figure 22, Figure 23 and Figure 24 are presented the sequence of vorticity plot for  $h/d = 1/3$ , 3 and 5, and the plot of  $h/d = 1$  is shown in Figure 21 in the previous subsection. It can be observed that overall the vortex structure both inside and outside the slot are quite similar for all cases. The key different that is noted is for the  $h/d = 1/3$  case which seems to exhibit noticeable asymmetry about the vertical centerline both outside and inside. The meandering of the vortex pairs in the outside jet is quite visible in Figure 22(d) and small asymmetries are also visible in the flow inside the cavity. The



simulation has been thoroughly checked to ensure that no asymmetry is introduced due to the numerical aspect of the simulation. Thus, this asymmetry in the flow seems to be intrinsic to this particular case. Although the precise mechanism that causes this asymmetry is not clear, one may be hypothesized as follows. The flow inside is susceptible to some instability, and this results in a small asymmetry in the flow that feeds into the slot during the expulsion stage. However, the passage of flow through the slot tends to diminish this asymmetry such that for larger  $h/d$ , the flow emerging from the slot is an almost perfectly symmetric jet. For the lowest  $h/d$  case ( $h/d = 1/3$ ) the slot is not long enough to mitigate the asymmetry thereby leading to a noticeable asymmetric jet.

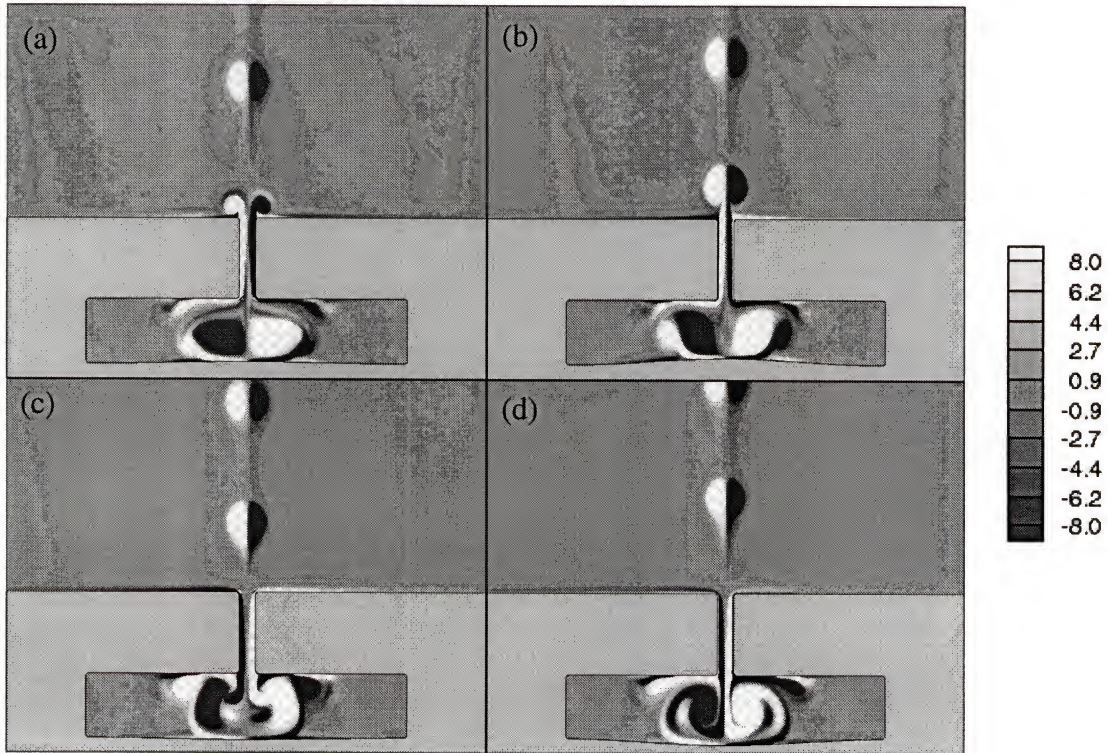


Figure 24. Vorticity contour plots for quiescent external flow,  $h/d = 5$  and  $Re_d = 250$  ( $A/H = 0.1$ ). a) Maximum expulsion; b) Minimum volume; c) Maximum ingestion; d) Maximum volume.



### 4.2.2 External Crossflow Cases

In this subsection, we examine the vortex dynamics for cases with external crossflow. For this configuration, in addition to the effect of  $Re_\delta$  and  $h/d$ , it is also of interest to examine what effect the parameter  $(V_{ave}^{inv}/U_\infty)$  has on the jet flow and the external boundary. All the cases presented here have  $\delta/d = 2$  and  $S = 10$ .

#### 4.2.2.1 Effect of jet Reynolds number

As before, we first examine the effect of increasing the jet Reynolds number on the vortex dynamics of the flow. The boundary layer Reynolds number ( $Re_\delta$ ) is equal to 254 for this sequence and the jet Reynolds number varies over the same range as the quiescent flow cases. The first case in this series corresponds to  $Re_d = 63$  ( $A/H = 0.025$ ). The ratio of mean jet expulsion velocity to crossflow velocity ( $V_{ave}^{inv}/U_\infty$ ) is equal to 0.5. The vorticity contour plot for this case is shown in Figure 25. For this case, we observe that the vortex formation process at the lip of the slot is disrupted completely by the

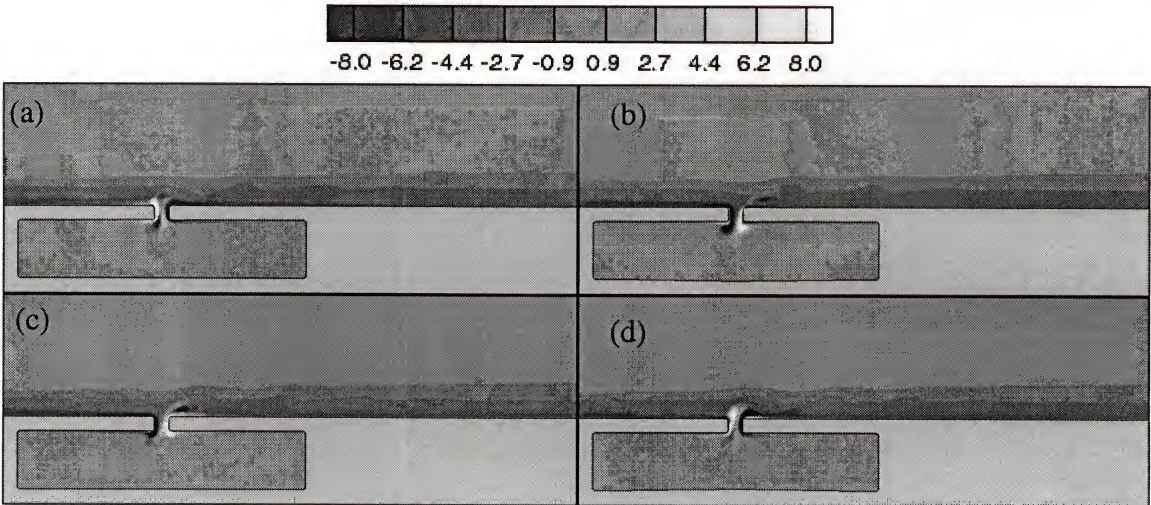


Figure 25. Vorticity contour plots for  $Re_\delta = 254$ ,  $h/d = 1$  and  $Re_d = 63$  ( $A/H = 0.025$ ). a) Maximum expulsion; b) Minimum volume; c) Maximum ingestion; d) Maximum volume.

crossflow. In particular the counterclockwise (CCW) rotation vortex that was seen to develop on the left lip of the slot in quiescent flow cases is quickly cancelled out by the clockwise (CW) vorticity in the crossflow boundary layer. In contrast, a distinct clockwise rotating vortex is observed to form but this also decays rapidly as it convects downstream.

The second case is with  $Re_d = 125$  ( $A/H = 0.05$ ) and the vorticity contour plot for this case is shown in Figure 26. The jet velocity to crossflow velocity ratio ( $V_{ave}^{inv}/U_\infty$ ) for this case is 1.0. For this higher jet velocity, we find that both vortices form at the lip of the slot. However, they immediately start convecting downstream due to the crossflow. Furthermore, due to vorticity cancellation, the CCW vortex diminishes in strength rapidly such that by about  $10d$  downstream of the slot only the CW vortex is visible.

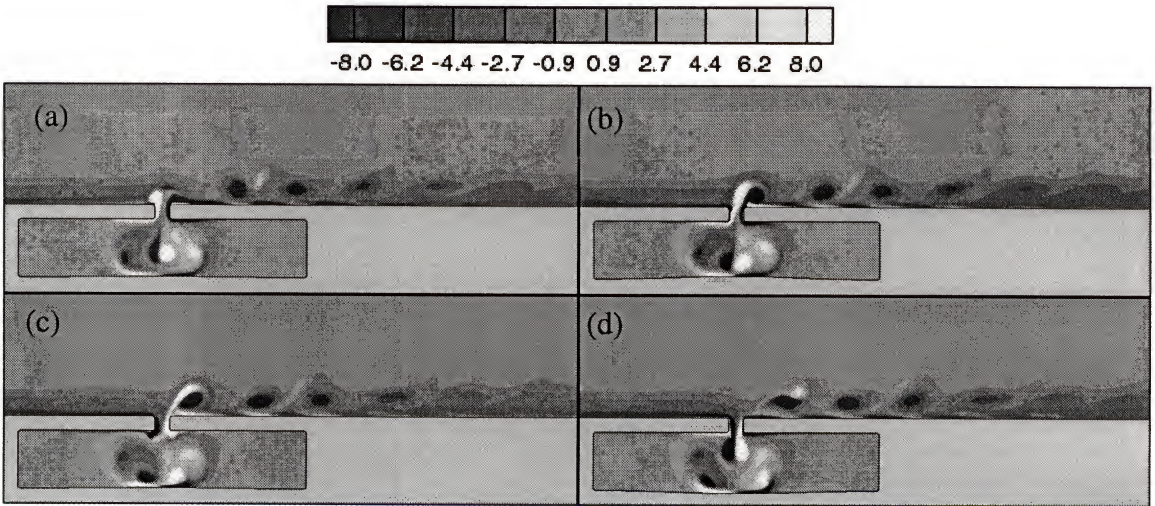


Figure 26. Vorticity contour plots for  $Re_g = 254$ ,  $h/d = 1$  and  $Re_d = 125$  ( $A/H = 0.05$ ). a) Maximum expulsion; b) Minimum volume; c) Maximum ingestion; d) Maximum volume.



Figure 27 shows a sequence of vorticity contour plots for the next case which has  $Re_d = 187$  and  $A/H = 0.075$ . The ratio  $V_{ave}^{inv}/U_\infty$  is equal to 1.5 for this case. It is observed that as in the case of quiescent external flow, a vortex pair forms at the jet lip during the expulsion stroke. However, this vortex pair immediately comes under the influence of the crossflow and begins to convect downstream. As the axis of the vortex-pair rotates clockwise, the CW vortex (that formed from the right lip of the slot) moves toward the wall and consequently slows down. On the other hand, the CCW vortex, which is exposed to a higher speed flow, convects downstream rapidly and approaches the clockwise vortex formed in the previous cycle. These two vortices now form a pair, which moves vertically due to self-induction while continuously being convected downstream. Note also that the vortices completely penetrate through the boundary layer and emerge into the freestream and this primarily due to the relative high jet velocity and the thin boundary layer. In actual separation control application, it is unlikely that such a

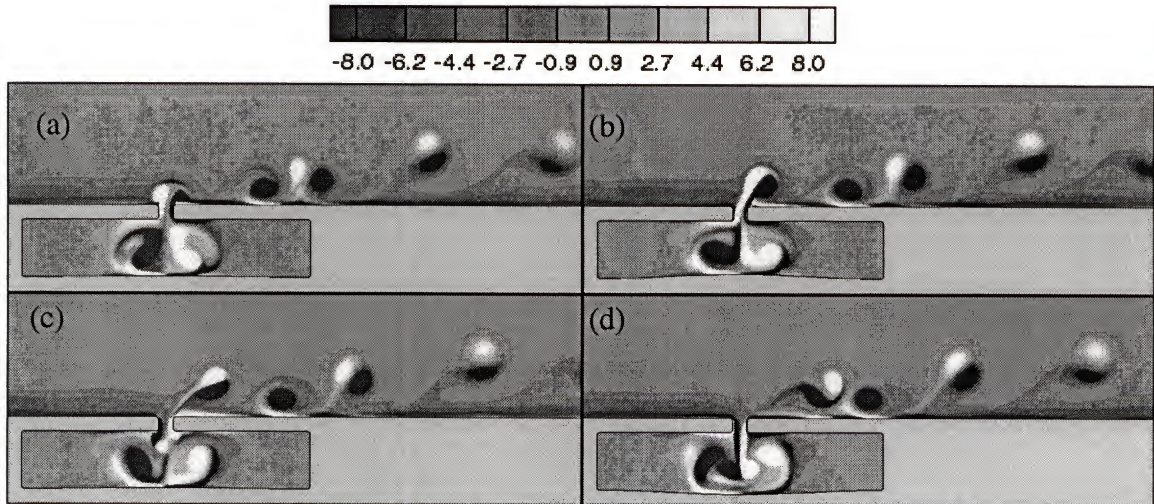


Figure 27. Vorticity contour plots for  $Re_\delta = 254$ ,  $h/d = 1$  and  $Re_d = 187$  ( $A/H = 0.075$ ).  
a) Maximum expulsion; b) Minimum volume; c) Maximum ingestion; d) Maximum volume.



complete disruption of the boundary layer will be desirable. However, this simulation is useful in that it demonstrates the typical scenario observed for a crossflow interacting with a synthetic jet.

Finally Figure 28 shows the sequence of vorticity plots for  $Re_d = 250$  ( $A/H = 0.1$ ) case for which  $V_{ave}^{inv}/U_\infty = 2.0$ . Interestingly, the vortex dynamics, particularly the cross pairing of vortices from different cycles, is similar to that obtained in the previous case indicating that this is a somewhat robust phenomenon. In addition, for this case, we also observe additional pairing occurring further downstream.

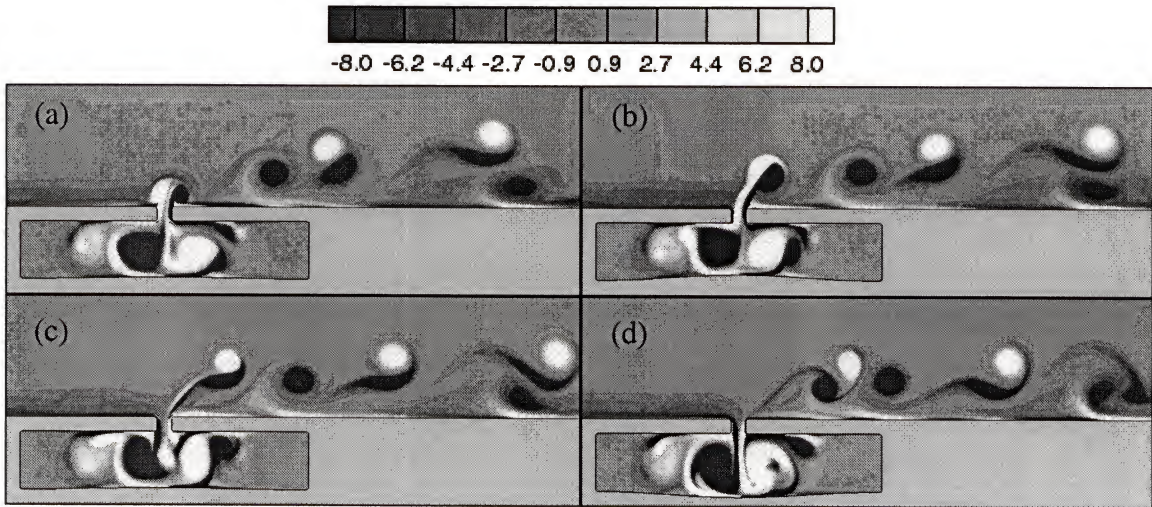


Figure 28. Vorticity contour plots for  $Re_\delta = 254$ ,  $h/d = 1$  and  $Re_d = 250$  ( $A/H = 0.1$ ). a) Maximum expulsion; b) Minimum volume; c) Maximum ingestion; d) Maximum volume.

#### 4.2.2.2 Effect of $h/d$

Figure 29 shows the vorticity plot for  $Re_d = 250$ , ( $A/H = 0.1$ ) case but with  $h/d = 3$ . Comparison with Figure 28 with  $h/d = 1$  Indicates that the difference in the initial development of the vortex structures is not significant. However, further downstream the vortex dynamics is slightly different. In particular for the  $h/d = 1$  case, the vortex pairs



reapproach the wall at a distance of about  $25d$  downstream of the slot, whereas for the  $h/d = 3$  case, this occurs at a distance of about  $30d$  downstream.

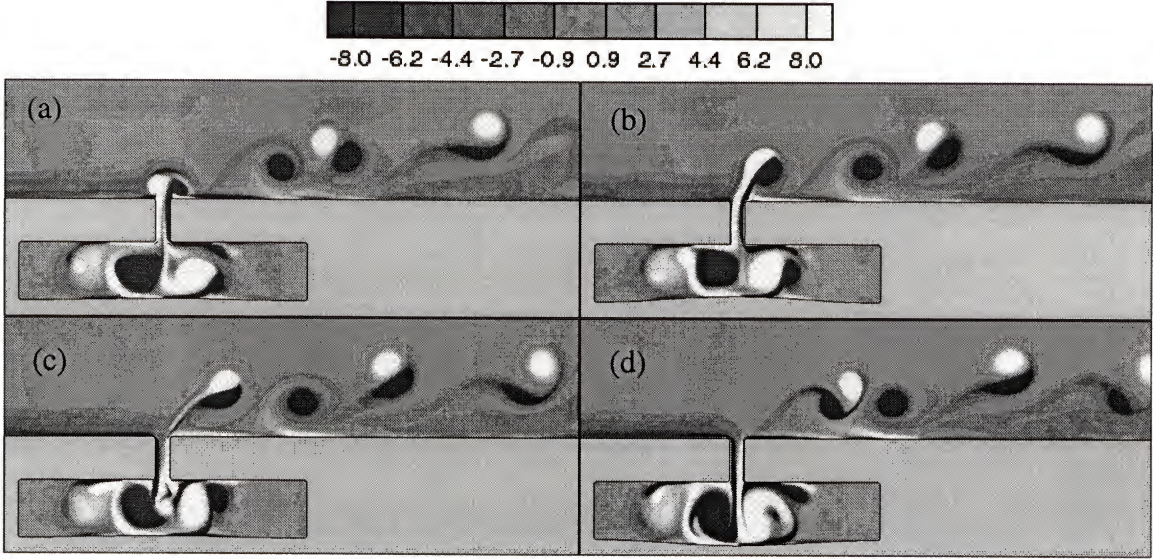


Figure 29. Vorticity contour plots for  $Re_\delta = 254$ ,  $h/d = 3$  and  $Re_d = 250$  ( $A/H = 0.1$ ). a) Maximum expulsion; b) Minimum volume; c) Maximum ingestion; d) Maximum volume.

#### 4.2.2.3 Effect of crossflow Reynolds number

In Section 4.2.2.1, we examined the vortex dynamics by fixing  $Re_\delta$  and varying  $Re_d$ . In this section, we fix  $Re_d$  to 250 and investigate the effect of varying  $Re_\delta$  on the vortex dynamics. The parameter  $h/d$  is equal to unity for all cases here. The lowest boundary layer Reynolds number case has  $Re_\delta = 254$  and this has already been described in Section 4.2.2.1 (Figure 28). In this section we show and describe the vortex dynamics for  $Re_\delta = 400, 800, 1200$  and  $2600$ . Thus  $Re_\delta$  is varied over about a ten fold range of values.

Figure 30 shows the plots for  $Re_\delta = 400$  for which  $V_{ave}^{inv} / U_\infty = 1.25$ . It is observed that due to the increased crossflow velocity, the vortex structures of the jet do not



penetrate as far into the freestream as in the  $Re_\delta = 254$  case. However, this case also exhibits the cross pairing of vortex structure.

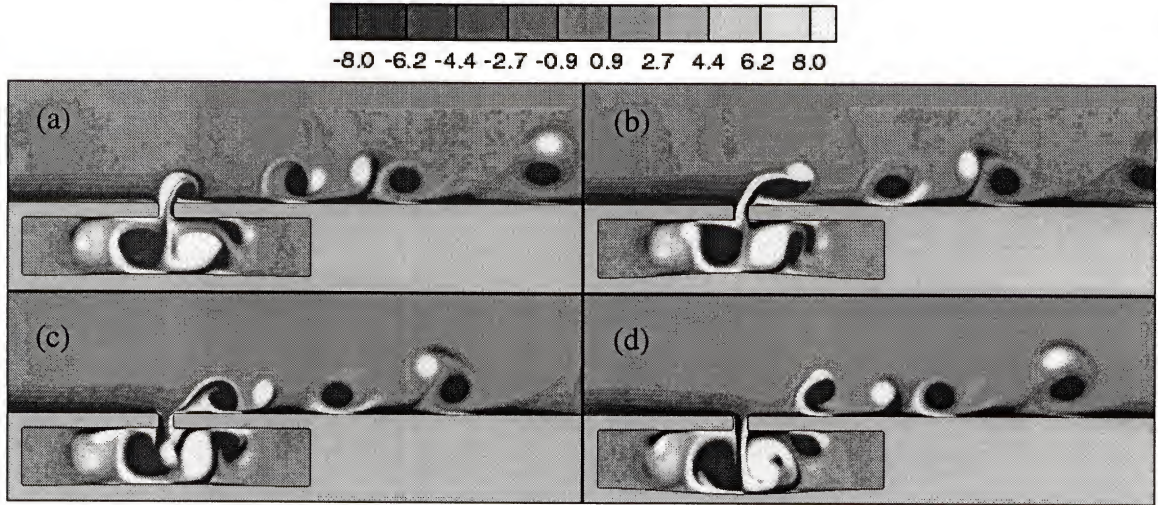


Figure 30. Vorticity contour plots for  $Re_\delta = 400$ ,  $h/d = 1$  and  $Re_d = 250$  ( $A/H = 0.1$ ). a) Maximum expulsion; b) Minimum volume; c) Maximum ingestion; d) Maximum volume.

The next sequence correspond to  $Re_\delta = 800$  and  $1200$ . Since the vortex dynamics for these two cases are quite similar, we show the plots for both cases (Figure 31 and Figure 32, respectively) but discuss only the  $Re_\delta = 1200$  case.

For this case, the freestream velocity is increased such that  $V_{ave}^{inv}/U_\infty = 0.42$ . Figure 32 shows the sequence of vorticity contour plots for this case and significant differences between this case and the previous cases are observed. First unlike the previous cases, the flow in the cavity is highly non-symmetric about the vertical centerline. Furthermore, the vortical structure formed inside the cavity is stronger and consequently the region of almost-stagnant fluid is smaller. During expulsion, two sets of counter-rotating vortices are produced. Due to the lower relative jet velocity, the vortices generated during expulsion do not penetrate out into the freestream.

Furthermore, no cross pairing of vortices is observed. Instead, the CCW vortex is cancelled out by the boundary layer, which is comprised of clockwise vorticity. In contrast, the CW vortex entrains fluid from the boundary layer and from the freestream and grows in size as it convects downstream. In addition, another smaller CW vortex is formed which trails behind the primary vortex. The expanded vorticity sequence shown in Figure 33 clearly shows that the secondary vortex forms due to the instability of the clockwise shear layer. In contrast to the previous case, the boundary layer is not completely disrupted by the jet and the vortex structures are found not to penetrate through to the freestream side. However, the vortex structures are large enough to directly entrain freestream fluid into the boundary layer. The entrainment of high momentum freestream fluid into the boundary layer by these vortices is an important feature since it has been hypothesized that this makes the resulting boundary layer more resistant to separation.

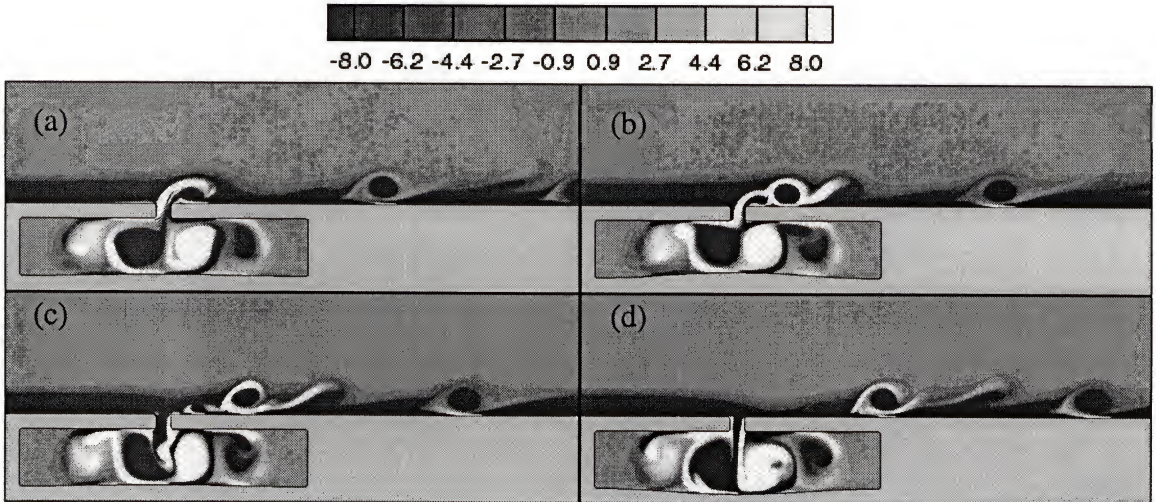


Figure 31. Vorticity contour plots for  $Re_g = 800$ ,  $h/d = 1$  and  $Re_d = 250$  ( $A/H = 0.1$ ). a) Maximum expulsion; b) Minimum volume; c) Maximum ingestion; d) Maximum volume.



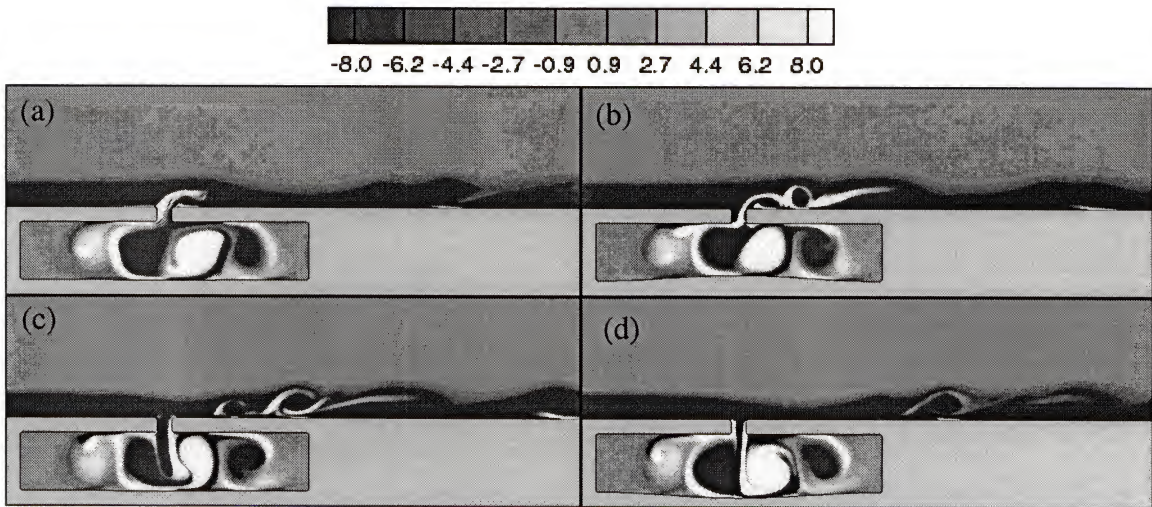


Figure 32. Vorticity contour plots for  $Re_\delta = 1200$ ,  $h/d = 1$  and  $Re_d = 250$  ( $A/H = 0.1$ ). a) Maximum expulsion; b) Minimum volume; c) Maximum ingestion; d) Maximum volume

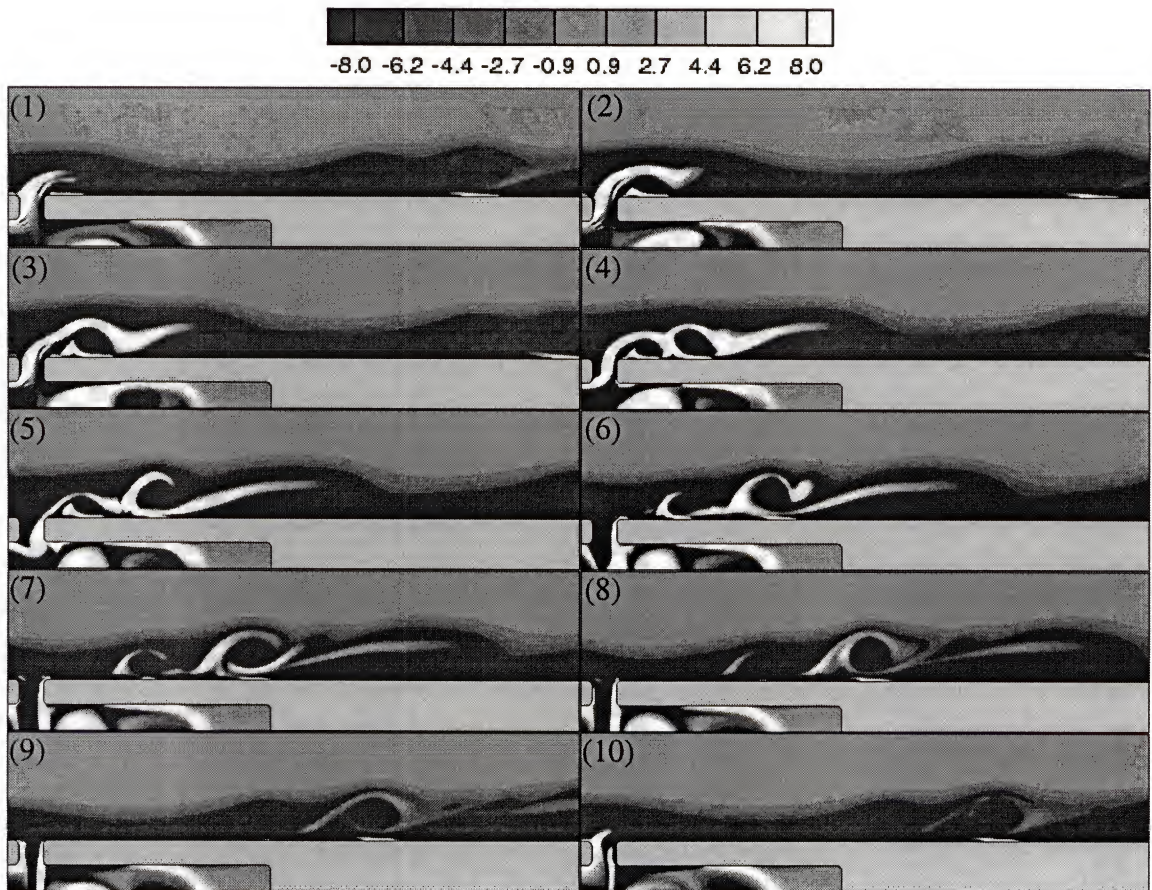


Figure 33. Series of the vorticity contour plots for  $Re_\delta = 1200$ ,  $h/d = 1$  and  $Re_d = 250$  ( $A/H = 0.1$ ).



The last case corresponds to the highest Reynolds number exterior flow simulated and for this simulation,  $V_{inv}^{ave}/U_{\infty} = 0.19$ . Figure 34 shows the sequence of vorticity contour plots for this case. With the higher exterior velocity, the counter-clockwise vorticity is cancelled quickly. Furthermore, the CW vortices are also found not to penetrate to the freestream side of the boundary layer. Consequently, no direct entrainment of freestream fluid into the boundary layer is observed. However, as in the previous case, the primary CW vortex is followed by a smaller clockwise vortex. It is also observed that the ingestion of higher momentum fluid energizes the fluid inside the cavity and consequently, the size of dead volume inside the cavity decreases. This further underscores the two-way coupling between the external flow and internal flow.

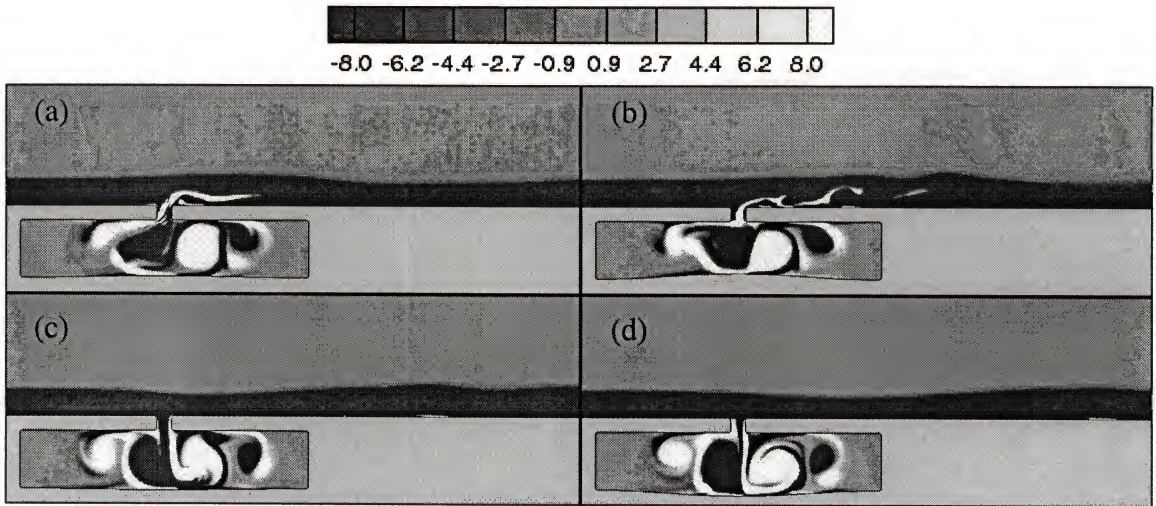


Figure 34. Vorticity contour plots for  $Re_s = 2600$ ,  $h/d = 1$  and  $Re_d = 250$  ( $A/H = 0.1$ ). a) Maximum expulsion; b) Minimum volume; c) Maximum ingestion; d) Maximum volume.

## CHAPTER 5

### VELOCITY PROFILES: COMPARISON AND ANALYSIS

In this chapter, the focus is on analyzing the jet velocity profiles in detail. The objectives here are to understand the effect that various parameters have on the jet exit velocity profiles, and how the integral measures of the jet scale with these parameters. Finally, a simple low-dimensional parametric model of the jet profile is tested. Velocity profiles were extracted at locations lying along the line shown in Figure 35.

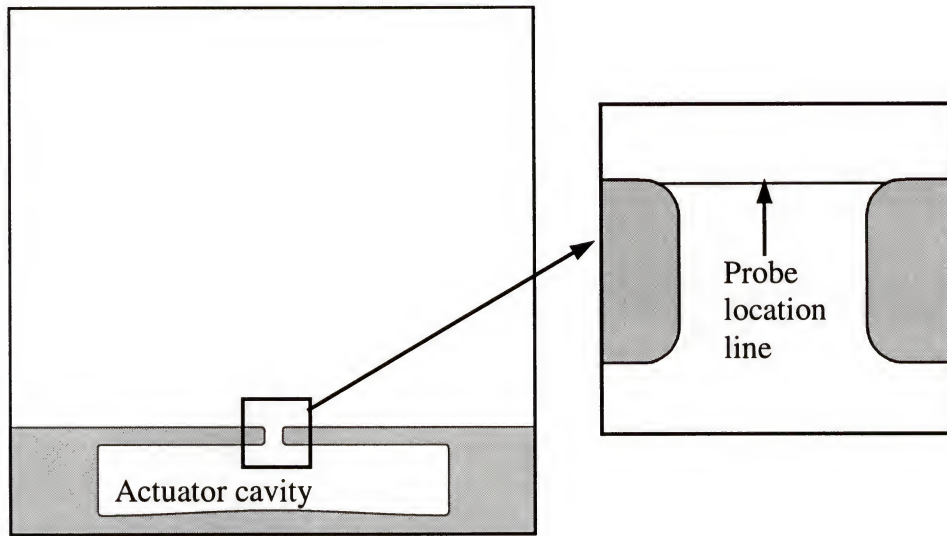


Figure 35. Probe location line along which velocity profiles were extracted.

#### 5.1. Comparison of Jet Velocity Profiles

In this section, we perform a qualitative comparison of the jet velocity profile for many different selected cases. The chronology of this section is similar to section 4.2, and this allows for direct comparison of vortex dynamics and associated changes in the

jet profile. In all the plots presented here, each velocity profile has been normalized by its own  $V_{\max}^{inv}$  to allow for easy comparison of profile shapes among various cases.

### 5.1.1 Quiescent External Flow Cases

First, as in Chapter 4, the quiescent flow cases will be presented, and this will be followed by the cases with external crossflow.

#### 5.1.1.1 Effect of jet Reynolds number

In this subsection, we compare the effects of jet Reynolds number on the jet velocity profile. Figure 36 shows the velocity profiles for different  $Re_d$ . The jet  $Re_d$  is increased by increasing the diaphragm amplitude. For each comparison, four plots are shown. These four plots, (a), (b), (c) and (d), correspond to maximum expulsion, minimum volume, maximum ingestion and maximum volume respectively. The parameter  $h/d$  is equal to one for all cases here.

First comparing the velocity profiles at maximum expulsion, it is observed that as the jet Reynolds number increases, the relative velocity in the core flow also increases. In order to further analyze this behavior, it is useful to make a comparison of the slot flow to flow in a channel due to an oscillatory pressure gradient. For fully developed flow in a channel exposed to an oscillatory pressure gradient, the shape of the velocity profile is only a function of the Stokes number (and not the Reynolds number). However, since for the slot flow, the profile shape changes with  $Re_d$ , this might indicate that flow at the jet exit is not fully developed, and the variation with  $Re_d$  is a manifestation of entrance effects. Also worth pointing out is the significant difference between the peak ingestion and expulsion profiles. In general, the profiles at peak ingestion are fuller and more plug



like and this is because the flow enters the slot at this location and so the flow is similar to the entrance flow in a channel

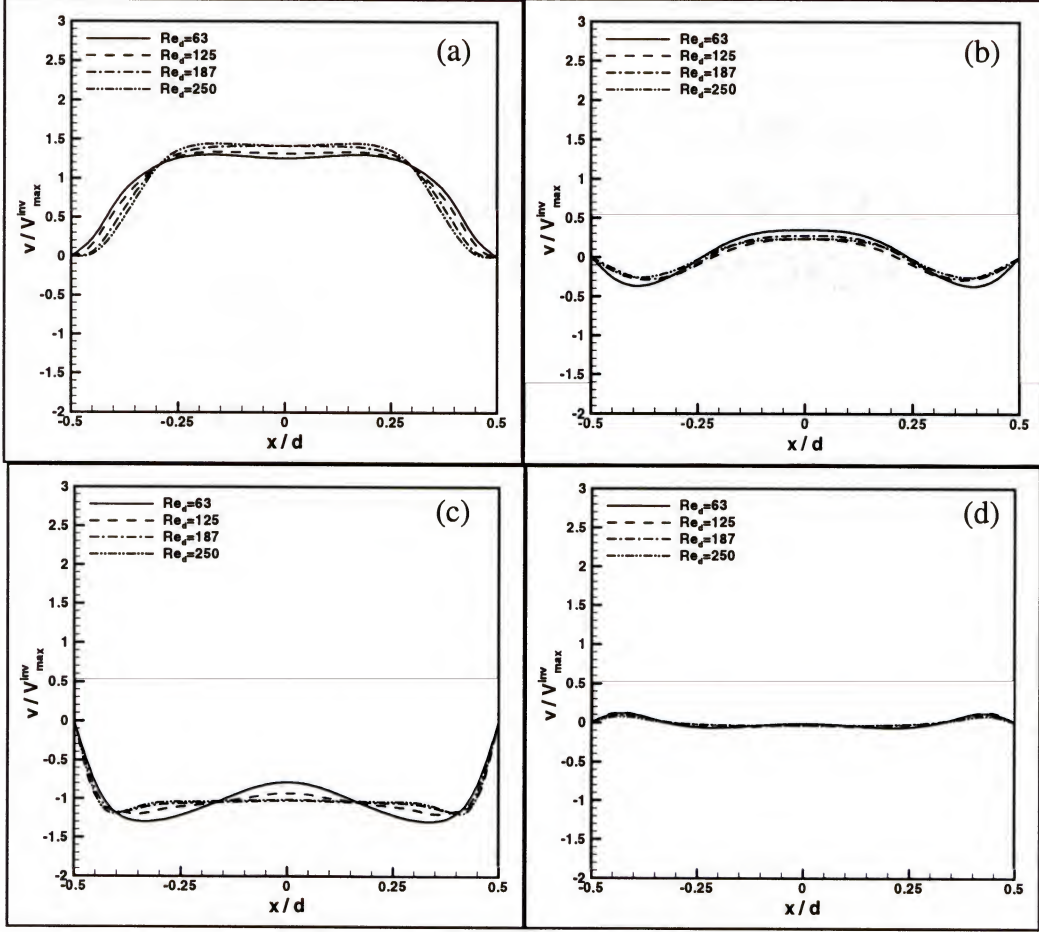


Figure 36. Velocity profiles for quiescent external flow cases with  $h/d = 1$ . a) Maximum expulsion; b) Minimum volume; c) Maximum ingestion; d) Maximum volume.

### 5.1.1.2 Effect of $h/d$

In this subsection, we examine the effect of the parameter  $h/d$  on the velocity profile. All cases chosen for comparison have  $Re_d = 250$  which is the highest jet Reynolds number case. Figure 37 shows the velocity profiles for these cases. In general, it is observed that as  $h/d$  is increased, the expulsion profile goes from having a broader to narrower plateau. This is consistent with the physical reasoning that with fixed  $Re_d$  and

$S$ , flow through a slot with larger  $h/d$  is more fully developed and has a thicker boundary layer. However interestingly, this trend is not monotonic since  $h/d = 1$  and  $5$  show very similar profiles. It is not clear at this time what physical mechanism causes this reversal in the behavior. Possible candidates are unsteady effects and modifications in the internal cavity flow. Also interesting to note is the asymmetry in the profile for  $h/d = 1/3$  case. The possible cause and effect of this asymmetry has previously been discussed in Chapter 4. During the ingestion, the flow profiles are quite similar and this is expected since the ingestion profile is not subjected to the development of flow through the slot.

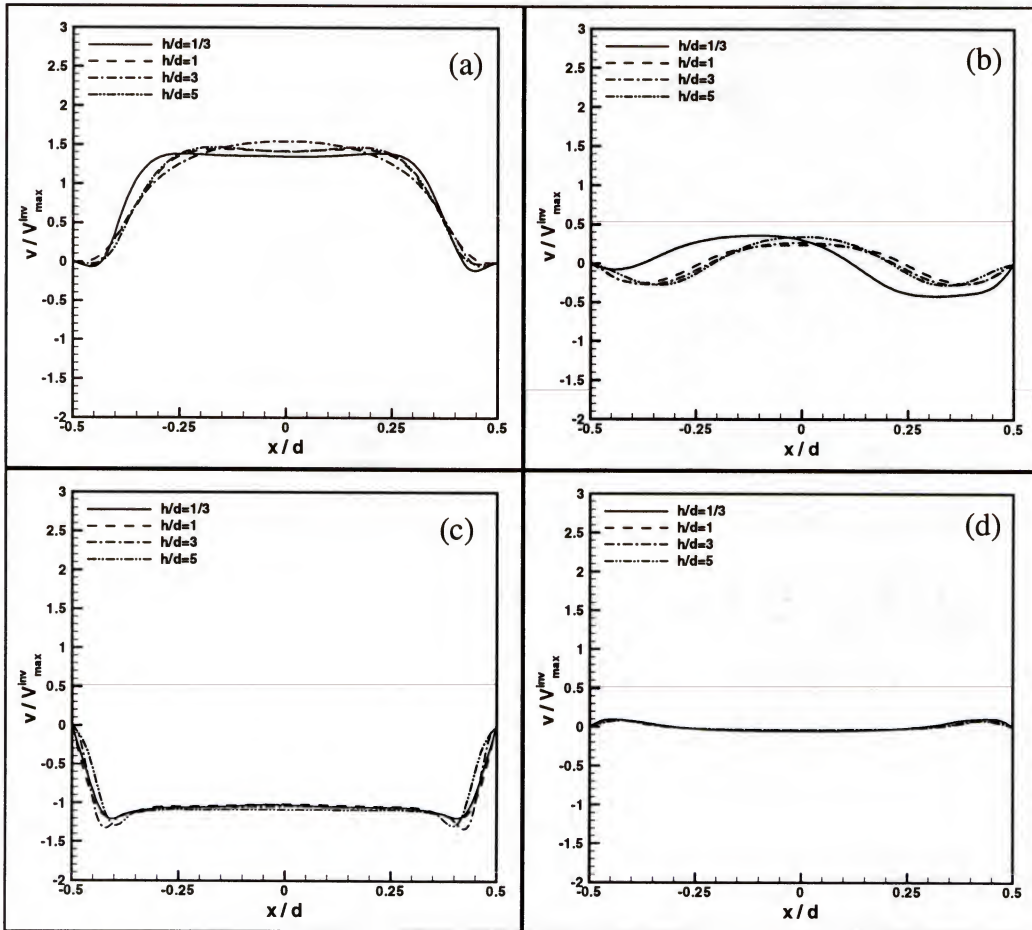


Figure 37. Velocity profiles for quiescent external flow cases with  $Re_d = 250$ . a) Maximum expulsion; b) Minimum volume; c) Maximum ingestion; d) Maximum volume.

### 5.1.2. External Crossflow Cases

In this subsection, we examine the velocity profiles for the cases with external crossflow. Corresponding vorticity plots for the cases examined here can be found in Section 4.2.2.

#### 5.1.2.1 Effect of jet Reynolds number

In this section, four cases with varying jet Reynolds numbers are compared in order to elucidate the effect of this parameter on the jet profile. The velocity profiles are shown in Figure 38. The external flow  $Re_\delta$ ,  $h/d$ , and  $\delta/d$  for all cases here are 254, 1,

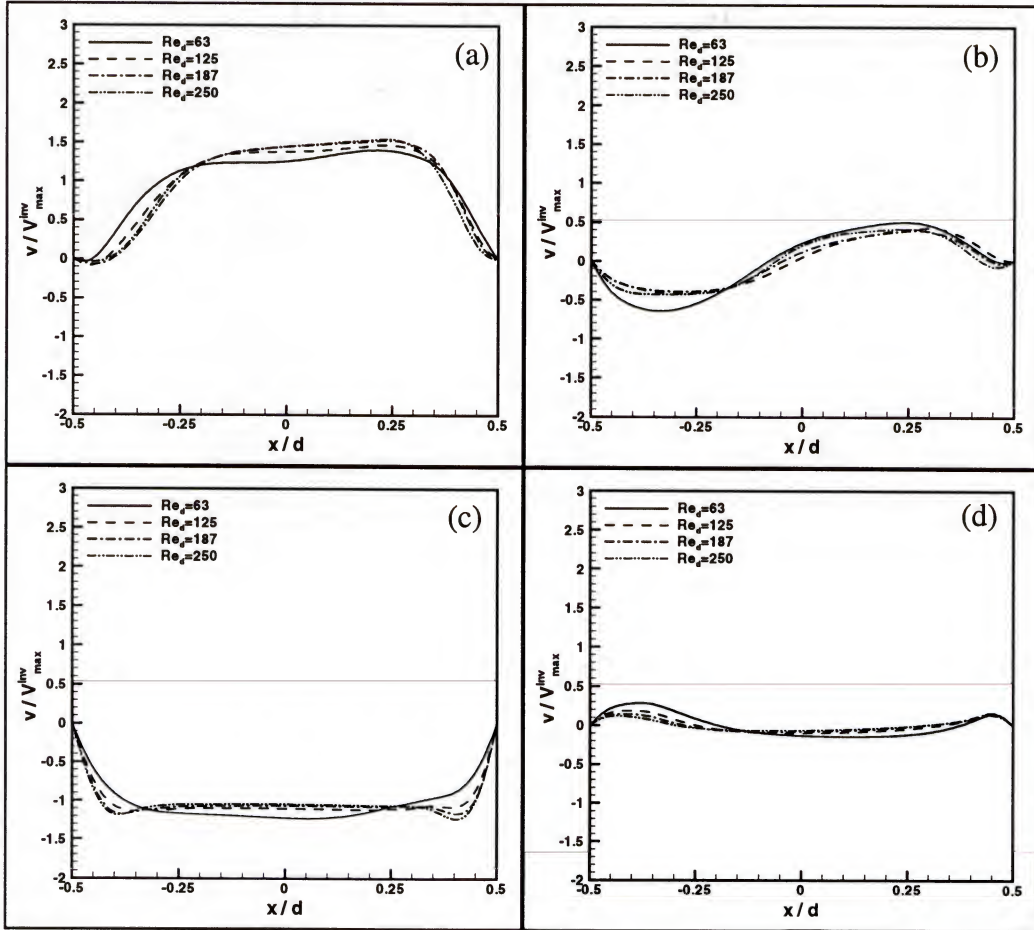


Figure 38. Velocity profiles for boundary-layer cases with  $h/d = 1$  and  $Re_\delta = 254$ . a) Maximum expulsion; b) Minimum volume; c) Maximum ingestion; d) Maximum volume.



and 2 respectively. The most noticeable change is the skewing of the jet profile to the right at maximum expulsion. This is obviously a direct consequence of the presence of the external crossflow. However otherwise, the trend of increasing core flow relative velocity with  $Re_d$  that was observed for the quiescent flow case is also observed here. The profiles are relatively less skewed during maximum ingestion. As will be seen later, even the ingestion profiles become more skewed as the external crossflow velocity is increased.

### 5.1.2.2 Effect of $h/d$

In this subsection we compare in a limited manner the effect of  $h/d$  on the jet profile with external crossflow by comparing case with  $h/d = 1$  and 3. Figure 39 shows the velocity profiles for these cases. The  $Re_d$ ,  $Re_\delta$ , and  $\delta/d$  for these cases are equal to 250, 254, and 2 respectively. No significant differences are observed between the two profiles. In fact, interestingly, it is observed that the  $h/d = 3$  shows a profile with a single maximum near the slot centerline, and this was also observed to be the case for the quiescent external flow cases. Thus, at least for these cases, some of the characteristics of the jet in quiescent flow are preserved in the presence of external crossflow. However, it should be noted that for all cases here, the jet velocity is significantly higher than the crossflow velocity ( $V_{ave}^{inv}/U_\infty = 2.0$ ) and thus the crossflow effect is expected to be small. In later sections, we will find that a higher relative crossflow velocity also has a significant effect of ingestion profile.

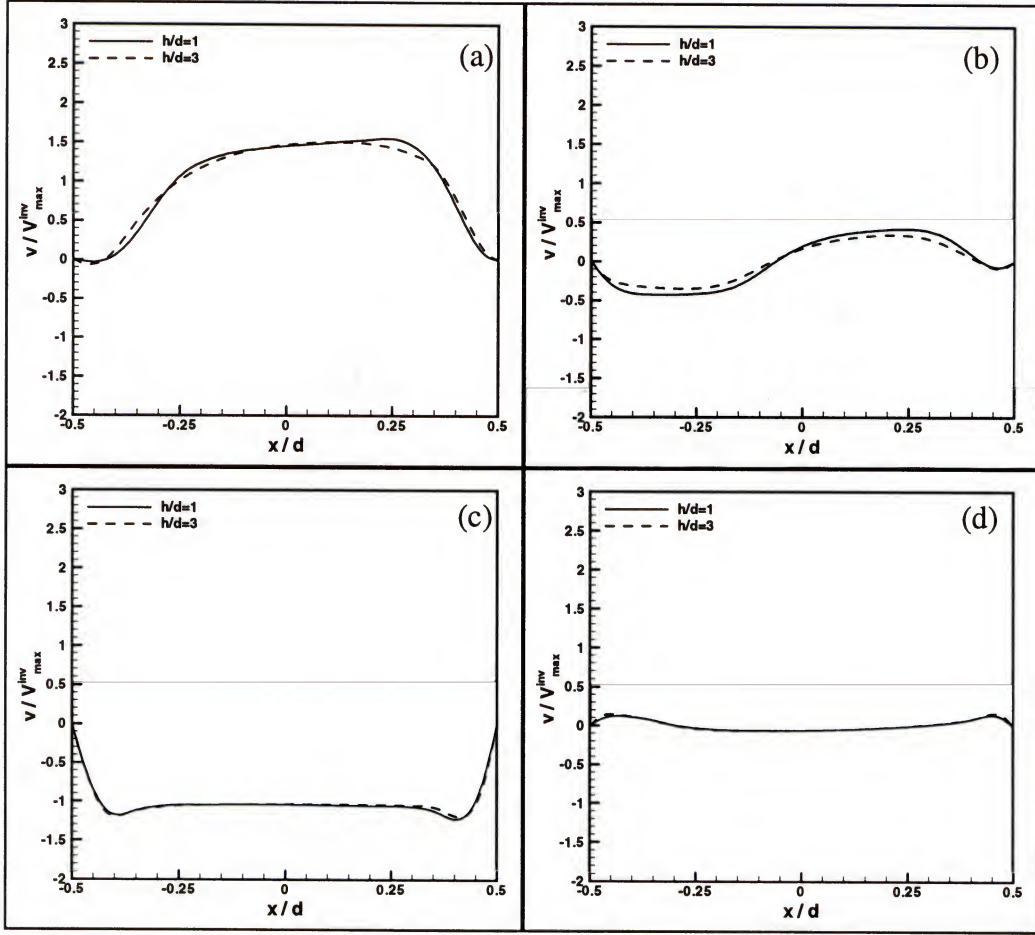


Figure 39. Velocity profiles for boundary-layer cases with  $Re_d = 250$ . a) Maximum expulsion; b) Minimum volume; c) Maximum ingestion; d) Maximum volume.

### 5.1.2.3 Effect of crossflow Reynolds number

The final comparison here is to evaluate the effect of crossflow Reynolds number on the jet profiles. For all the cases compared here,  $Re_d = 250$ ,  $h/d = 1$  and  $\delta/d = 2$ . The crossflow Reynolds number is increased systematically from 0 to 2600 by increasing the crossflow velocity  $U_\infty$ . Figure 40 shows the velocity profile at maximum expulsion and a clear trend in the profile with increasing  $Re_d$  is observed. In particular, it is found that the profile gets increasingly skewed to the right as  $Re_\delta$  is increased. In fact, at

higher  $Re_\delta$ , a significant portion of the jet profile indicates an inflow during expulsion. Due to mass conservation, this then implies that the jet exit velocity has to increase and this is indeed what is observed. For  $Re_d = 2600$ , it is found that the peak jet velocity is almost three times the maximum inviscid velocity of the jet. A similar trend of increasing skewness is also observed in the profiles at maximum ingestion.

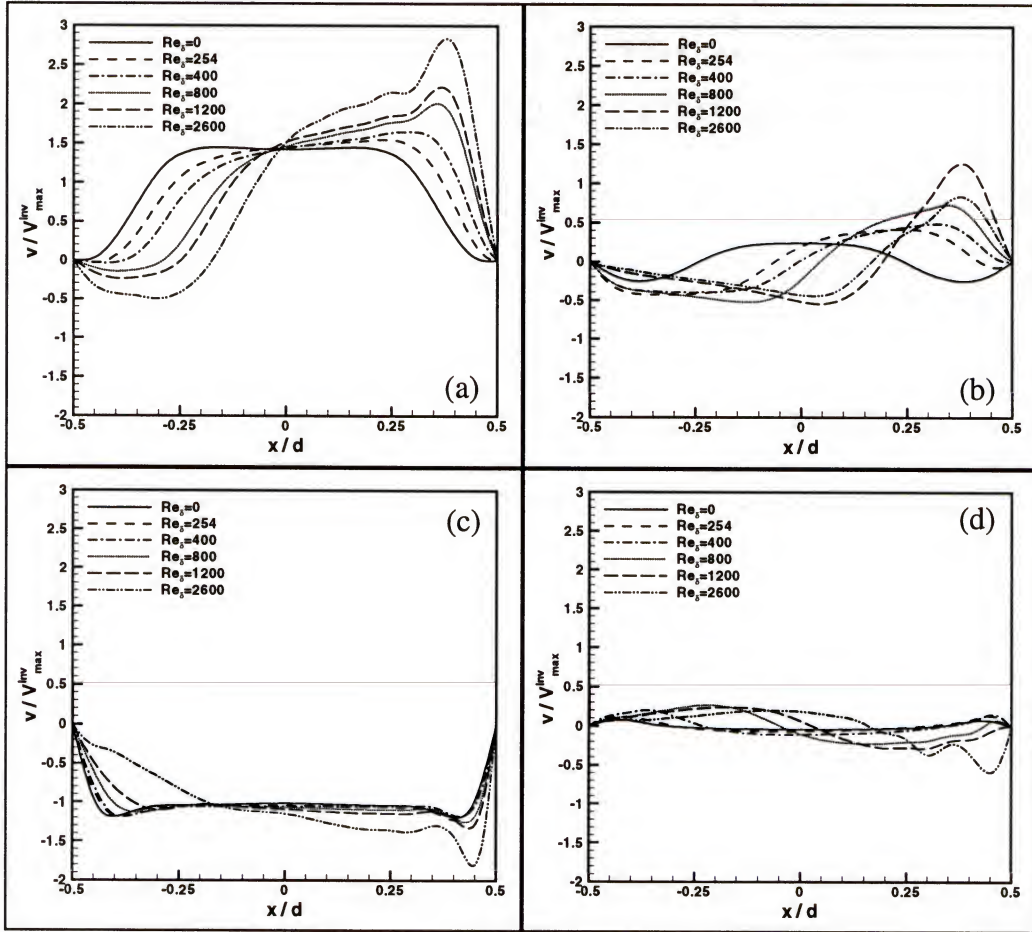


Figure 40. Velocity profiles for boundary-layer cases with  $Re_d = 250$  and  $h/d = 1$ . a) Maximum expulsion; b) Minimum volume; c) Maximum ingestion; d) Maximum volume.



## 5.2 Integral Measures of the Jet

The effect of various parameters on the jet profiles has been qualitatively studied in the previous section. In this section, we examine this effect quantitatively by computing the various integral measures of the jet profile as discussed in chapter 4.

### 5.2.1 Jet Momentum Coefficients

First, we compare the momentum coefficient of various jets since this is the first non-zero moment of a synthetic jet. In examining the profiles in the previous section, it was concluded that profiles during expulsion and ingestion were quite different and it was therefore decided to compute all integral parameters separately for the expulsion and ingestion phases. Furthermore, the computed moment is normalized by the moment corresponding to inviscid flow over the expulsion (and ingestion) phase, which allows us to easily examine how close the profile is to an inviscid flow.

#### 5.2.1.1 Quiescent external flow cases

First, we look at the variation of momentum coefficient with  $Re_d$  and  $h/d$  for the quiescent external flow as shown in Figure 41. First, for all cases, it is found that momentum coefficient of the expulsion phase is noticeably higher than that of the ingestion phase. Typical values of normalized momentum coefficient during ingestion are about 1.1 whereas during expulsion they are about 1.3. This is because, as shown by the comparison of jet profiles, the profile during expulsion has higher peak velocity than during ingestion. Furthermore for all cases except for  $h/d = 1/3$ , the ingestion momentum coefficient is observed to decrease monotonically with  $Re_d$ . This is also consistent with the fact that with increasing jet Reynolds number, the ingestion profile becomes more “plug-like” and the momentum coefficient approaches that of a uniform inviscid profile.

In contrast, the momentum coefficient during expulsion is observed to increase (though not monotonically) with  $Re_d$  for all cases. Again, this is consistent with an increase in peak jet velocity with  $Re_d$  observed before. The different scaling behavior observed for the ingestion and expulsion phases validates the rationale for splitting up the analysis into these two phases.

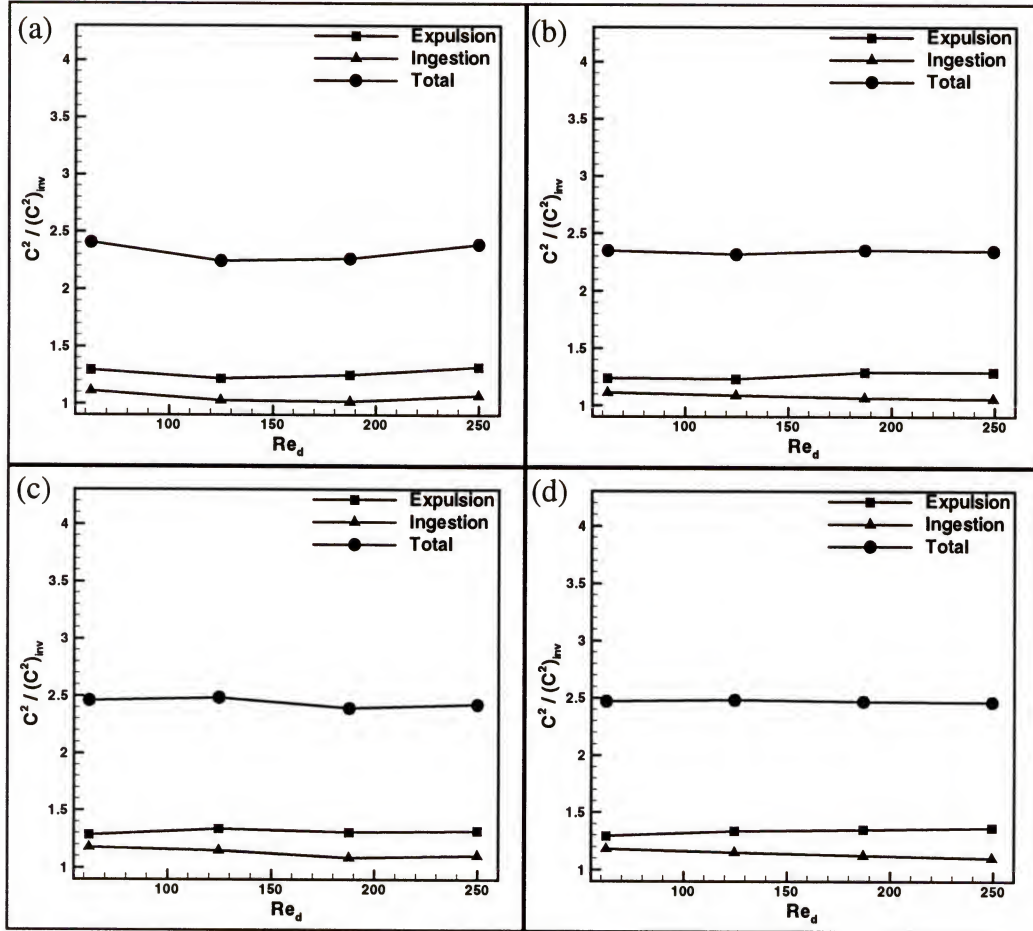


Figure 41. Momentum coefficient for quiescent external flow cases. a)  $h/d = 1/3$ ; b)  $h/d = 1$ ; c)  $h/d = 3$ ; d)  $h/d = 5$ .

The  $h/d = 1/3$  case also exhibits a shallow minimum for both the ingestion and expulsion moments and this behavior can be explained based on our previous observation of the jet exit velocity profile for these cases. It was found for these cases that as  $Re_d$  is

increased, the profile starts to exhibit skewness. Thus, the profile does not move monotonically towards a plug profile with increasing  $Re_d$ . Consequently, after an initial decrease, the momentum coefficient starts to rise slowly at higher  $Re_d$ .

### 5.2.1.2 External crossflow cases

In this section, we consider the effect of  $Re_d$  and  $Re_\delta$  on the momentum coefficient of the cases with external crossflow. Figure 42(a) corresponds to  $Re_\delta = 254$  which is the lowest external crossflow case presented here. As shown in section 4.2, the vortex dynamics for this case are quite different from that of the quiescent external flow case. However, a comparison of the momentum coefficient does not reveal any significant difference. The ingestion coefficient slowly decreases with increasing  $Re_d$  and expulsion coefficient increases slowly and monotonically. The only noticeable difference between this case and the corresponding quiescent flow case is the slightly increases level of momentum coefficient which can be attributed primarily to the change in jet expulsion profile.

With increasing  $Re_\delta$ , the variation of the momentum coefficient with  $Re_d$  departs significantly from the quiescent flow case and this is quite obvious from Figure 42(b) and (c) which correspond to  $Re_\delta = 1200$  and  $2600$  respectively. For these higher external velocity cases, it is found that the magnitude of the normalized momentum coefficient even at low jet velocities is quite high. For instance, for  $Re_\delta = 254$  the ingestion and expulsion momentum coefficients are equal to 1.2 and 1.3 respectively at  $Re_d = 63$  whereas the corresponding value are both equal to about 1.55 for  $Re_\delta = 1200$ . As  $Re_d$  is increased, the momentum coefficient for ingestion phase decreases



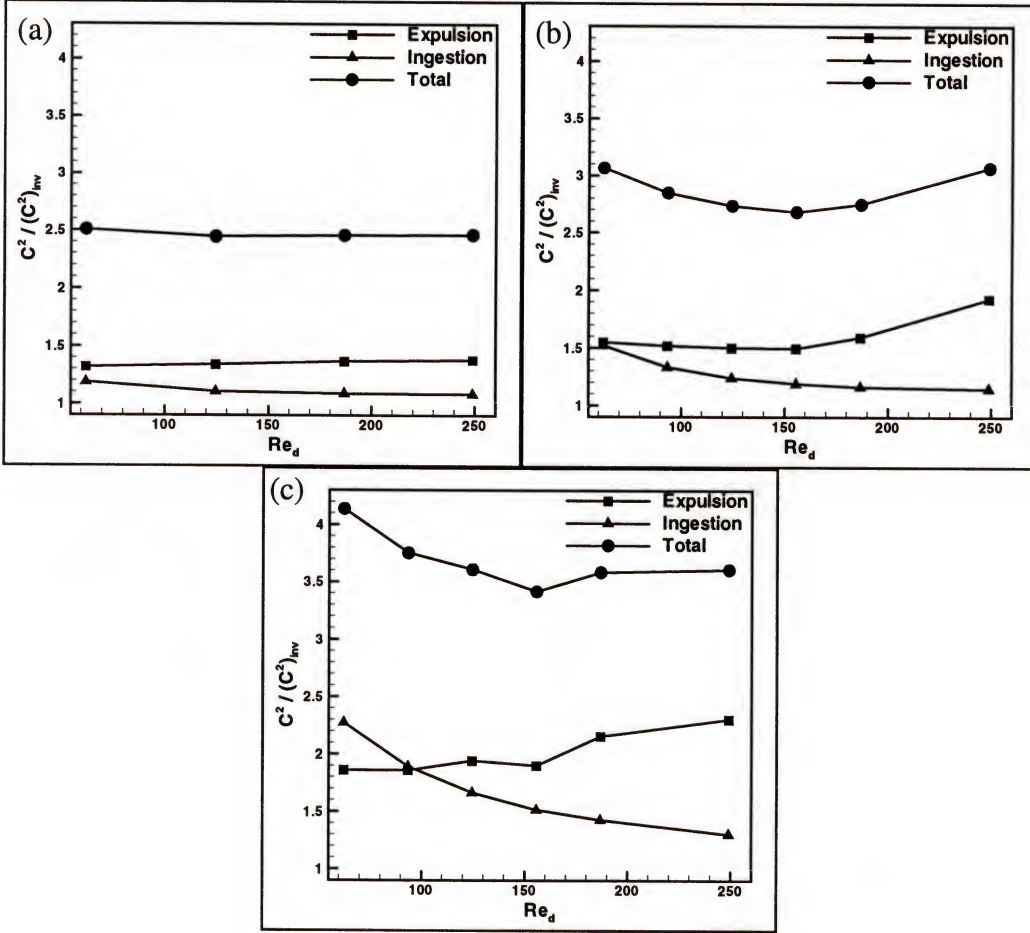


Figure 42. Momentum coefficient for boundary-layer cases. a)  $Re_\delta = 254, \delta/d = 2$ ; b)  $Re_\delta = 1200, \delta/d = 2$ ; d)  $Re_\delta = 2600, \delta/d = 2$ .

monotonically for both  $Re_\delta = 1200$  and  $2600$ , and the expulsion momentum coefficient is found to increase, though not monotonically. Both the increase and decrease is much more rapid than the quiescent flow cases and this is due to the increasing skewness and peakiness of the profile with increasing jet velocity. The higher external flow Reynolds also shows some unique behavior. For this case, it is found that at the lowest jet velocity, the ingestion momentum coefficient is higher than the expulsion momentum coefficient. This is because at low jet velocities, the fluid ingested has high velocity associated with the high-speed freestream and this speed is higher than the speed during expulsion. As

the jet  $Re_d$  (and velocity) is increased, the effect of the external flow diminishes and the behavior becomes more in line with the other cases.

### 5.2.2 Energy Flux

Another integral parameter that merits some attention is the energy flux coefficient, which is the third moment of the jet velocity profile. Note that in the case where the ingestion and expulsion profiles are the same, this parameter will be identically equal to zero. Therefore, this parameter cannot only be considered a measure of the flux of kinetic energy but also of the mismatch between the ingestion and expulsion phases of the jet. Here we examine the variation of this quantity with the various key parameters.

#### 5.2.2.1 Quiescent external flow cases

First, we examine the effect of  $h/d$  and  $Re_d$  on this parameter for the quiescent flow cases and the discussion here is based on Figure 43. The key observation to be made is that this parameter does not show any significant variation with either of these parameters. For all cases studied here,  $C^3/(C^3)_{inv}$  is roughly about 1.7 and  $-1.3$  for the expulsion and ingestion phases, resulting in a fairly universal value of about 0.4 for the total flux coefficients. This observation is useful from the point of view of dynamical modeling of the jet (as discussed later in this chapter) since this parameter could be matched quite easily in a modeled profile.

#### 5.2.2.2 External crossflow cases

The energy flux coefficient in the presence of external crossflow is examined. The results are shown in Figure 44. As for the momentum coefficient, it was found that a low external flow  $Re_\delta$  of 254 does not significantly affect the behavior of this parameter. However, much more complex behavior emerges at higher  $Re_\delta$  of 1200 and 2600. First,

the overall magnitude of the ingestion and expulsion energy flux coefficients are much higher for these cases. Furthermore, both cases show a much larger variation in energy coefficient with jet Reynolds number. In particular if we focus on the  $Re_\delta = 2600$  case we find that there is a significant increase in the energy coefficient for both the ingestion and expulsion phases. Furthermore, for this case, it is even found that at low jet velocities, the net energy flux is negative, indicating that the jet in fact acts as a sink of kinetic energy.

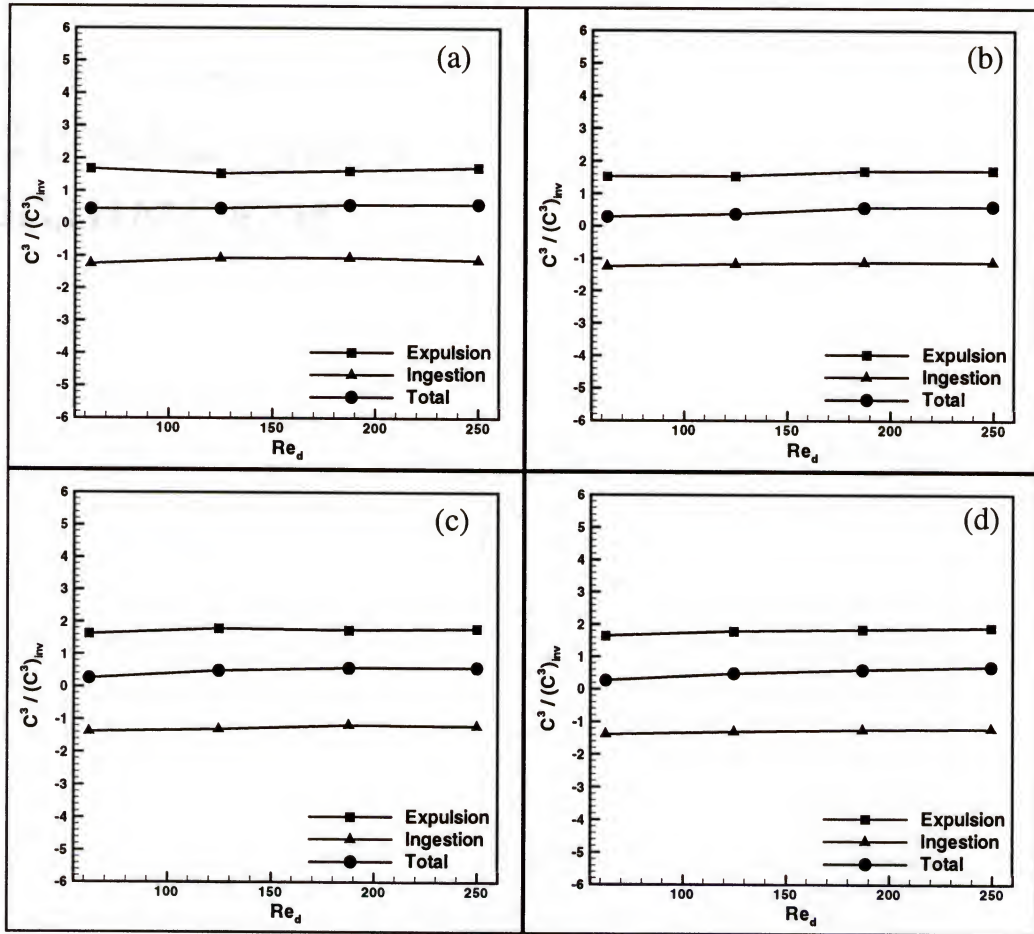


Figure 43. Energy flux coefficient for quiescent external flow cases. a)  $h/d = 1/3$ ; b)  $h/d = 1$ ; c)  $h/d = 3$ ; d)  $h/d = 5$ .



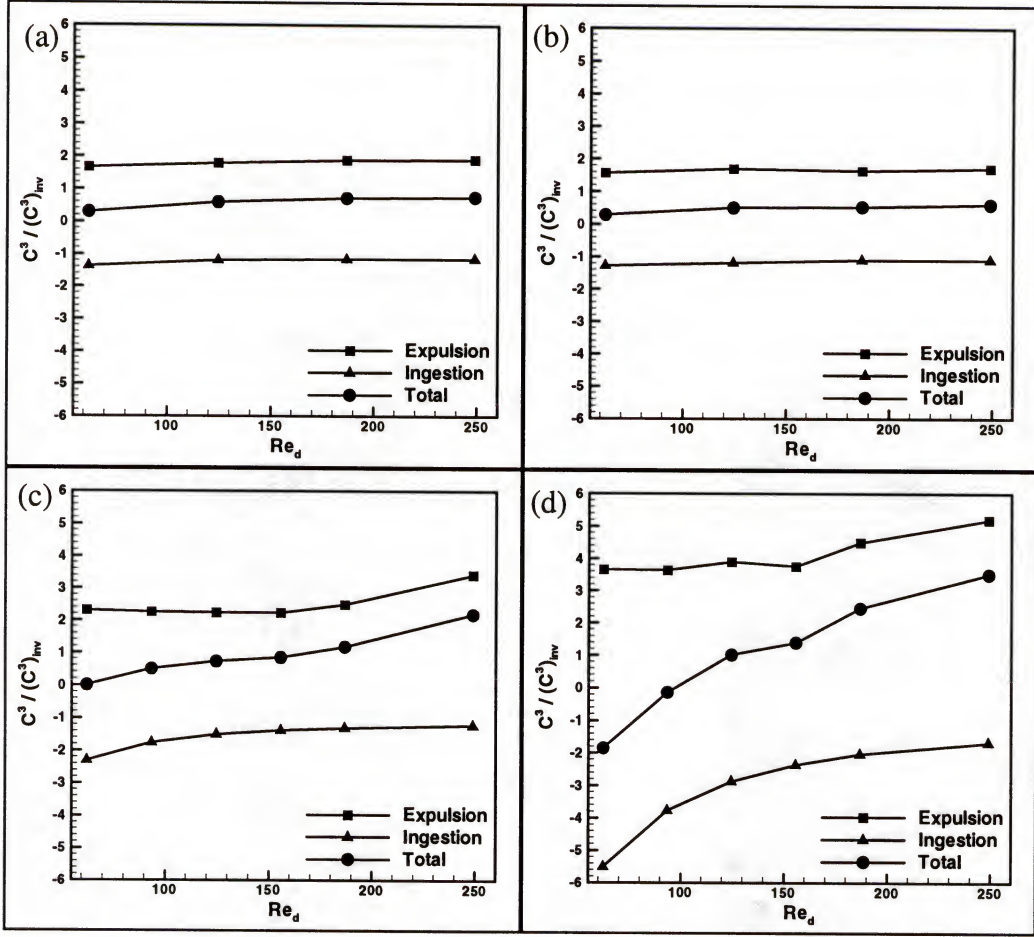


Figure 44. Energy flux coefficient for boundary-layer cases. a)  $Re_\delta = 254, \delta/d = 2$ ; b)  $Re_\delta = 254, \delta/d = 5$ ; c)  $Re_\delta = 1200, \delta/d = 2$ ; d)  $Re_\delta = 2600, \delta/d = 2$ .

### 5.2.3 Skewness Coefficient

In this section, we examine the skewness in the jet velocity profiles and the effect of  $Re_\delta$  and  $Re_d$  on this parameter. Two series of cases corresponding to low (63) and high (250) values of  $Re_d$  are chosen. As before, we examine this parameter separately for the expulsion and ingestion phases. Figure 45(a) shows the variation of the expulsion skewness coefficient with  $Re_\delta$  for fixed values of  $Re_d$ . The plot indicates that as  $Re_\delta$  is increased, the skewness increases monotonically and shows indication of asymptotically approaching a constant value. The asymptotic approach value is higher for the higher

$Re_d$  case. Since the skewness coefficient is computed by the normalizing by  $V_{ave}^{inv}$ , the increase in skewness with  $Re_d$  cannot be attributed to the increase in nominal jet velocity. Rather it is a reflection of the change in the shape of the velocity profile.

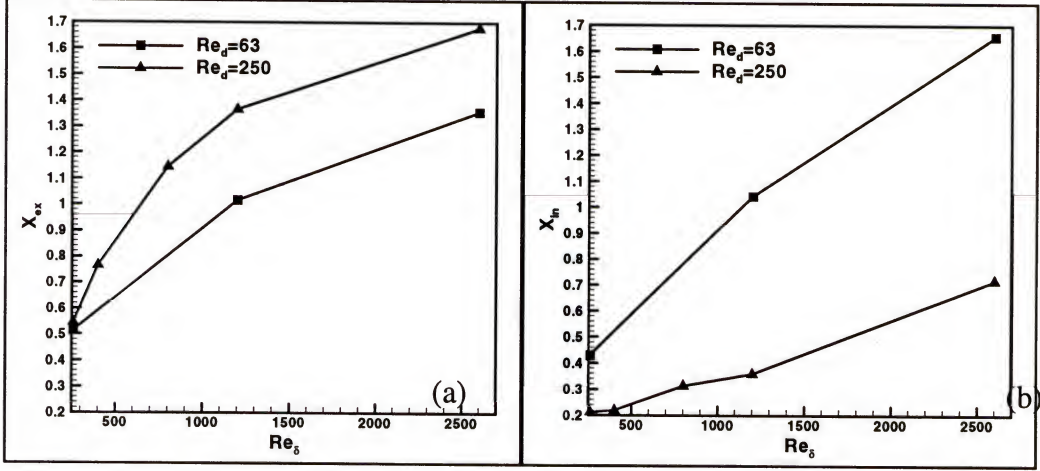


Figure 45. Skewness coefficient versus  $Re_\delta$  for  $Re_d = 63$  and 250. a) Expulsion half; b) Ingestion half.

Focusing now on the ingestion phase we find that here too, the skewness increases monotonically with  $Re_\delta$  for both  $Re_d = 63$  and 250. However interestingly, the skewness is significantly higher for the  $Re_d = 63$  case and this is opposite to our observation for the expulsion phase. In order to explore this unexpected behavior, we plotted the jet profile for the  $Re_d = 63$  case in Figure 46 for different  $Re_\delta$  going from 0 to 2600. Note that for the case with  $Re_d = 63$  and  $Re_\delta = 2600$ , the skewness coefficient is about 1.65 and 1.4 for the ingestion and expulsion phases respectively. Now looking at the corresponding velocity profile it is clear that indeed, the ingestion profile is more skewed than the expulsion profile. At low jet velocity, jet merely acts to redirect the high-speed external flow steam down through the slot during ingestion and this is the primary reason for increased skewness of the ingestion velocity profile.

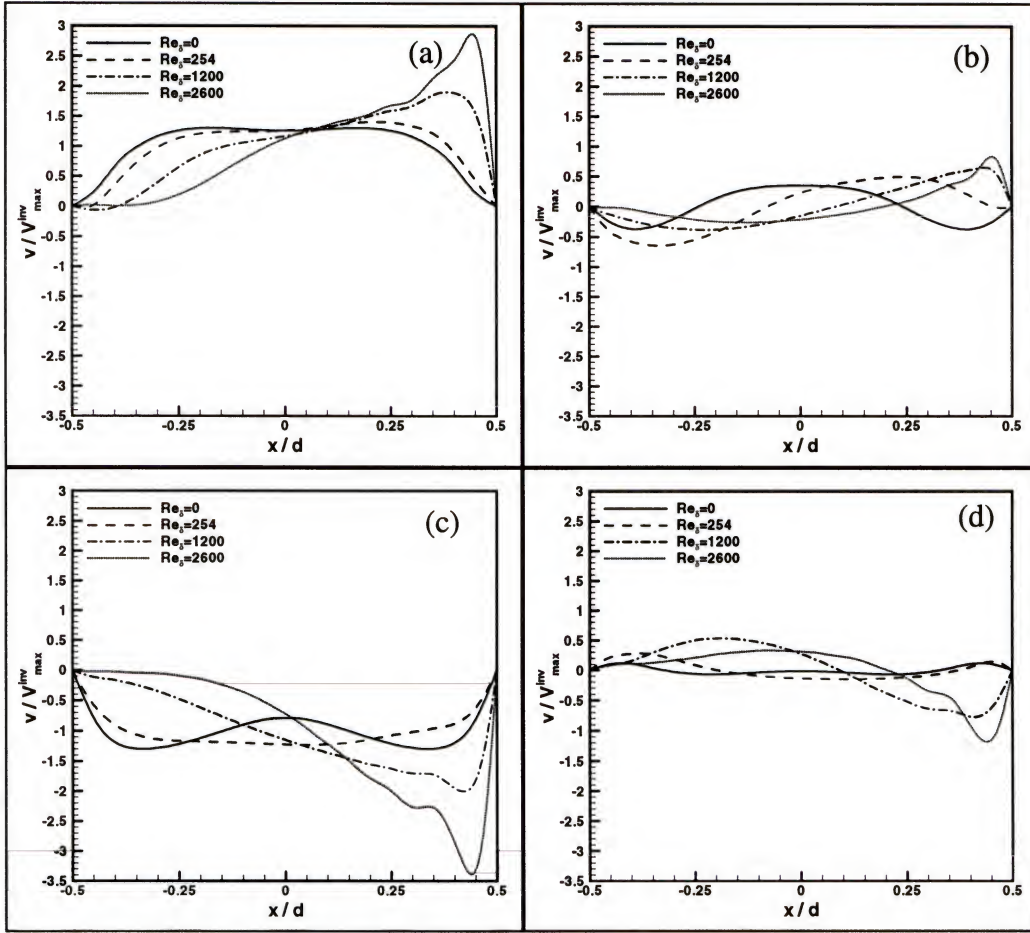


Figure 46. Velocity profiles for boundary-layer cases with  $Re_d = 63$  and  $h/d = 1$ . a) Maximum expulsion; b) Minimum volume; c) Maximum ingestion; d) Maximum volume.

### 5.3 Modeling of Jet Velocity Profiles

The scaling laws and characterization of synthetic jets is also expected to play an important role in the aerodynamic design of wings which, in the future, would use such devices for separation control. The current design paradigm in the aerospace industry relies heavily on RANS (Reynolds-Averaged Navier-Stokes) computations. These computations can be quite expensive and direct inclusion of synthetic jets into these computations is expected to increase this expense considerably since it would require the resolution of the 3-D flow inside the jet cavity as well as the flow through the slot.



Recognizing that the flow inside the cavity is not of direct interest in aerodynamic design of the wing, a viable alternative is to simply apply the jet velocity profile as a time-dependent boundary condition in the RANS computation. This approach essentially decouples the computation of the outer flow from that of the inner cavity flow. One way to obtain the profile is to perform a separate calculation of the flow in the local vicinity of the jet, extract the velocity profile from the simulation, and use it as a time dependence BC in the RANS calculation of the wing.

However, consider now the practical case, where for a given wing profile, RANS computations are being used to select the size, location and other operational parameters of the synthetic jet so as to have the most effective separation control. In such a scenario, the procedure described above, i.e. extracting velocity profiles from corresponding local-level simulations and including it as a boundary condition in the RANS computation, is somewhat impractical since it would require detailed local-level simulations at each test point. In this regard, what is needed is a low-dimensional "model" or description of the jet, i.e. parameterization of the jet in terms of 2-3 parameters that capture the important dynamic and kinematic features of the jet, and scaling laws that relate these parameters to the other flow parameters. Since the number of grid points required across the slot is directly proportional to the dimensionality of the flow profile, keeping the dimensionality of jet profile low is important from the point-of-view of the computational expense of the RANS computation. A number of different candidate profiles can be used. Here we investigate how well one particular candidate profile is able to match the complex jet profile extracted from our simulation.

### 5.3.1 Candidate Jet Profile

The candidate profile chosen should 1) be low dimensional 2) be capable of reasonably matching the observed and measured characteristics of the jet profile. In particular, our simulations indicate that the profile is not parabolic in shape, and can also exhibit significant skewness. These two observations guided the selection of the candidate profile.

As a starting point, the jet exit velocity profile is assumed to have a variation of the form

$$\begin{aligned} V_j(x, t) &= T_{ex}(x) \sin(2\pi F^+ t) \text{ during expulsion} \\ V_j(x, t) &= T_{in}(x) \sin(2\pi F^+ t) \text{ during ingestion} \end{aligned} \quad (31)$$

where  $T(x)$  represents a chosen family of jet profiles. Modeling the jet profile is now an exercise in choosing an appropriate form for  $T(x)$ . Based on our preliminary simulations, some potential approaches to this modeling can be hypothesized. For instance, the simulations indicate that four parameters that might be key characteristics of the jet are the mean jet velocity, maximum jet velocity, jet momentum coefficient and the jet skewness. In addition, the velocity profile should also satisfy the constraint of zero net mass flux. A family of jet profiles can easily be devised that matches any subset of these four parameters and the mass flux constraint. Consider a candidate 3-parameter family for modeling the expulsion or ingestion velocity profile of the form

$$T(x) = (Ax + B) \left\{ 1 - (2x/d)^2 \right\}^{1/m} \quad (32)$$

This profile satisfies the no-slip condition at the slot walls and the three free parameters can be used to match any three jet parameters. In fact, from inspection, it may be noted



Table 2. Maximum jet velocity, momentum coefficient, skewness,  $A$ ,  $B$  and  $m$ .

Case	$V_j^{\max}$		$C_{\varphi_{12}}^2$		$X_{\varphi_{12}}$		$A$		$B$		$m$	
	Ex	In	Ex	In	Ex	In	Ex	In	Ex	In	Ex	In
1	0.66	0.61	0.12	0.10	0.01	0.00	0.05	0.03	0.66	0.61	0.88	1.20
2	1.32	1.06	0.44	0.37	0.02	0.01	0.12	0.03	1.32	1.06	0.80	1.98
3	2.07	1.55	1.01	0.82	0.02	0.01	0.14	0.05	2.07	1.55	0.70	2.28
4	2.87	2.13	1.89	1.53	0.22	0.17	1.89	0.89	2.82	2.08	0.71	2.50
5	0.62	0.59	0.10	0.09	0.00	0.00	0.01	0.01	0.62	0.59	0.96	1.21
6	1.28	1.09	0.44	0.39	0.00	0.00	0.00	0.01	1.28	1.09	0.96	1.94
7	2.01	1.52	0.97	0.80	0.01	0.00	0.05	0.02	2.01	1.52	0.76	2.45
8	2.69	2.01	1.73	1.41	0.00	0.00	0.03	0.02	2.69	2.01	0.74	2.49
9	0.59	0.57	0.09	0.09	0.00	0.00	0.00	0.00	0.59	0.57	0.90	1.13
10	1.27	1.07	0.39	0.33	0.00	0.00	0.01	0.01	1.27	1.07	0.71	1.42
11	2.06	1.58	1.00	0.83	0.00	0.00	0.01	0.00	2.06	1.58	0.70	2.06
12	2.79	2.12	1.80	1.51	0.00	0.00	0.01	0.01	2.79	2.12	0.68	2.06
13	0.59	0.57	0.09	0.09	0.00	0.00	0.00	0.00	0.59	0.57	0.90	1.13
14	1.27	1.07	0.39	0.33	0.00	0.00	0.00	0.01	1.27	1.07	0.73	1.42
15	1.97	1.52	0.88	0.73	0.00	0.00	0.01	0.01	1.97	1.52	0.65	1.72
16	2.69	2.00	1.59	1.28	0.00	0.00	0.01	0.01	2.69	2.00	0.60	1.76
17	0.62	0.60	0.10	0.09	0.04	0.04	0.27	0.33	0.62	0.58	0.95	1.18
18	1.30	1.07	0.42	0.35	0.06	0.07	0.48	0.39	1.29	1.06	0.80	1.78
19	2.00	1.54	0.99	0.82	0.13	0.08	0.99	0.40	1.97	1.53	0.84	2.51
20	2.75	2.03	1.80	1.46	0.27	0.11	2.15	0.57	2.67	2.00	0.81	2.80
21 (wide)	2.78	2.03	1.81	1.45	0.30	0.12	2.45	0.61	2.68	2.00	0.79	2.77
22	0.68	0.65	0.11	0.10	0.13	0.11	0.96	0.80	0.61	0.58	1.00	1.20
23	1.38	1.09	0.44	0.36	0.27	0.12	1.99	0.69	1.22	1.04	0.98	1.95
24	2.11	1.56	1.00	0.80	0.43	0.15	3.20	0.80	1.86	1.50	0.94	2.48
25	2.88	2.06	1.80	1.41	0.56	0.22	4.38	1.10	2.55	1.97	0.84	2.67
26	2.76	2.05	1.76	1.43	0.48	0.18	3.53	0.91	2.51	1.98	0.94	2.81
27	3.01	2.07	1.89	1.41	0.79	0.23	5.69	1.14	2.43	1.97	1.00	2.64
28	3.37	2.17	2.21	1.45	1.17	0.32	7.76	1.67	2.30	2.00	1.24	2.44
29	0.80	0.78	0.13	0.12	0.26	0.27	1.65	1.52	0.55	0.52	1.50	2.00
30	1.17	1.04	0.28	0.24	0.38	0.30	2.32	1.67	0.82	0.77	1.58	2.12
31	1.53	1.27	0.49	0.40	0.49	0.32	2.99	1.71	1.10	1.02	1.55	2.23
32	1.90	1.50	0.76	0.60	0.61	0.33	3.70	1.73	1.37	1.26	1.53	2.34
33	2.40	1.73	1.16	0.85	0.81	0.34	5.02	1.76	1.66	1.51	1.48	2.41
34	3.66	2.25	2.50	1.49	1.40	0.37	9.28	1.97	2.30	2.04	1.23	2.21
35	0.89	1.01	0.15	0.18	0.35	0.43	1.79	2.69	0.51	0.56	2.69	1.43
36	1.32	1.34	0.34	0.35	0.53	0.54	2.59	2.79	0.74	0.75	3.04	2.60
37	1.81	1.64	0.63	0.54	0.74	0.62	3.74	2.97	1.00	0.97	2.68	3.32
38	2.22	1.90	0.96	0.77	0.90	0.67	4.58	3.12	1.25	1.19	2.62	3.66
39	2.90	2.16	1.58	1.04	1.22	0.70	7.28	3.45	1.64	1.47	1.60	2.98
40	4.05	2.62	2.99	1.69	1.72	0.74	11.00	3.59	2.26	1.96	1.34	3.04



that  $B$  controls the centerline velocity,  $A$  controls the skewness of the profile, and  $m$  controls the departure of the profile from a parabolic shape in the absence of skewness.

In this preliminary test which can be considered a proof-of-concept stage,  $V_{ave}^{inv}$ ,  $C^2$ , the momentum coefficient, and  $X$ , the skewness coefficient are chosen separately for the ingestion and expulsion cases. Note that  $V_{ave}^{inv}$  is the same for the ingestion and expulsion phases due to mass conservation and by using this as the one of the matching parameters, the zero net mass-flux condition of the synthetic jet is automatically satisfied.

For each case simulated here, we have taken the computed  $V_{ave}^{inv}$ ,  $C^2$  and  $X$  and using the Secant iterative method, have obtained values of  $A$ ,  $B$  and  $m$  that produce the same values of  $V_{ave}^{inv}$ ,  $C^2$  and  $X$  in the modeled profile. Table 2 shows the computed  $A$ ,  $B$  and  $m$  for all the cases simulated here. In addition, we provide visual comparison for selected actual and modeled profile. Expulsion and ingestion phase are denoted by “Ex” and “In” respectively.

### 5.3.2 Comparison of Actual and Modeled Profile

In this subsection, we compare the modeled and actual profiles for quiescent and external crossflow cases.

#### 5.3.2.1 Quiescent external flow cases

Some comparisons for quiescent external flow cases are shown first. Figure 47 shows four cases with  $Re_d = 63, 125, 187$  and  $250$ . The  $h/d$  for all cases here is unity. Furthermore, we only compare the maximum ingestion and maximum expulsion profiles. It is observed that for all cases the match between the two profiles is reasonable. While the maximum velocity is reasonably close for the two cases, the chosen profile clearly

does not produce the “double-lobed” shape of the actual profile. However, the current profile clearly picks up the difference between the ingestion and expulsion phase and this is one attractive feature of the chosen profile. Note from the table that values of  $m$  are closer to unity for the expulsion phase than they are for the ingestion phase and this is primarily in response to the lower value of  $C^2$  for the ingestion phase.

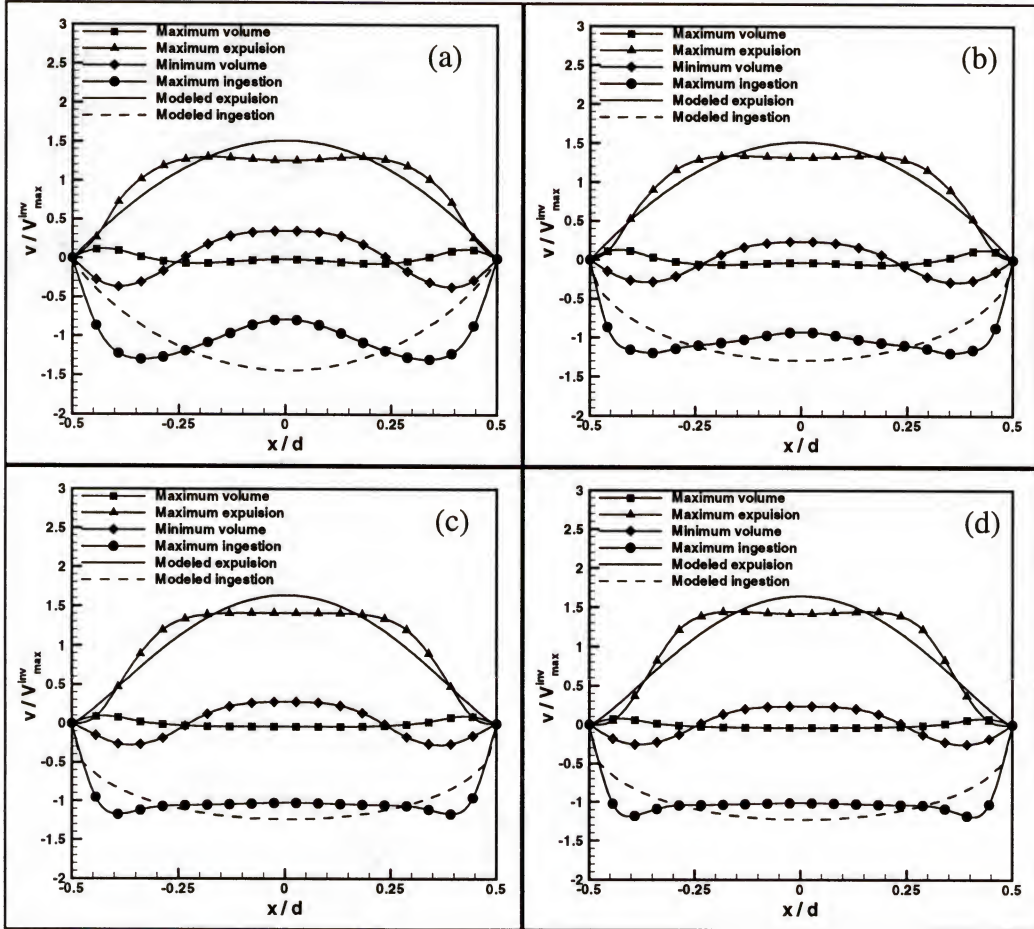


Figure 47. Comparison of actual and modeled profiles with  $h/d = 1$ . a)  $Re_d = 63$ ; b)  $Re_d = 125$ ; c)  $Re_d = 187$ ; d)  $Re_d = 250$ .

Comparison of cases with various  $h/d$  shown in Figure 48 also indicates a similar match between the actual and modeled profile. Interestingly, the matching procedure

picks up the skewness in the jet profile observed for  $h/d = 1/3$  case and produces a noticeably skewed modeled profile.

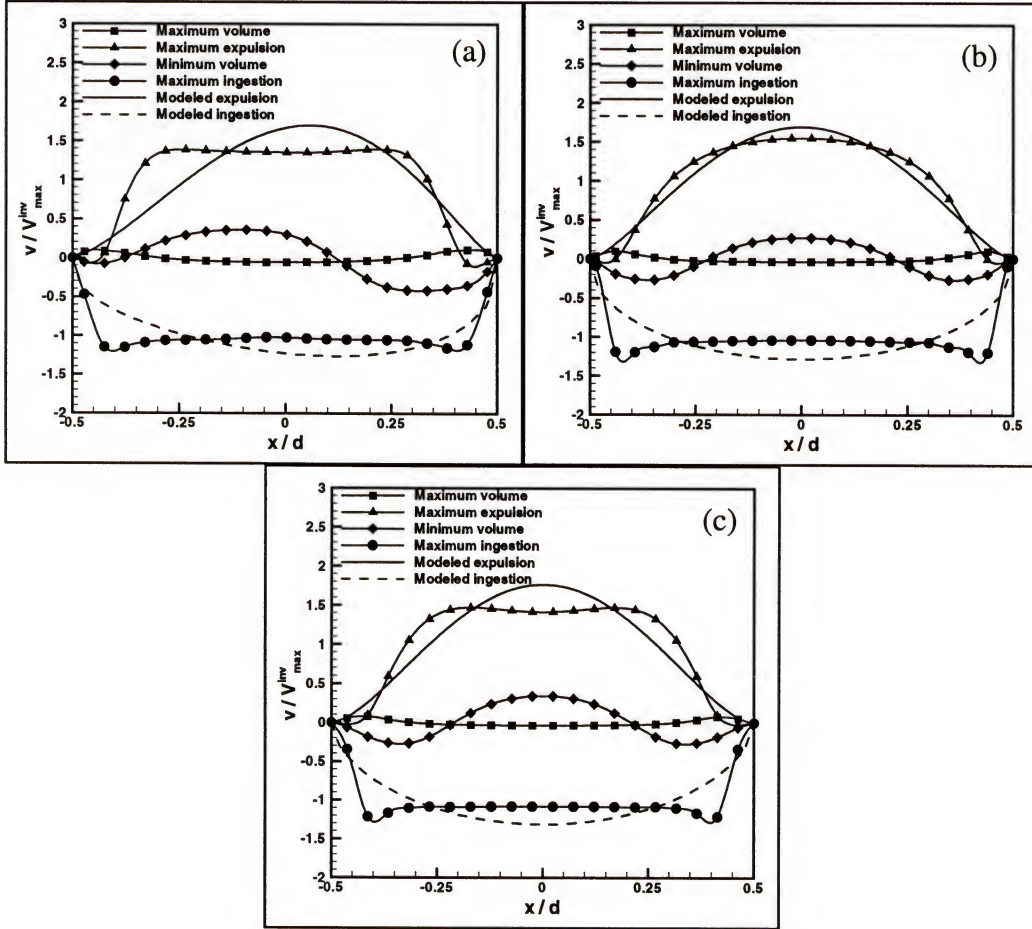


Figure 48. Comparison of actual and modeled profiles with  $Re_d = 250$ . a)  $h/d = 1/3$ ; b)  $h/d = 3$ ; c)  $h/d = 5$ .

### 5.3.2.2 External crossflow cases

Now we turn to comparing the modeled and actual profiles for the external crossflow cases. Figure 49 shows the comparison for four cases, with  $Re_d = 62, 125, 187, 250$ . For all these cases,  $Re_\delta = 254$ , and  $h/d = 1$ . For this relatively low external flow Reynolds number case, the jet velocity profiles have a character similar to case with quiescent external flow consequently the comparison of the modeled and actual profiles



is similar to that observed for the quiescent flow cases. Peak expulsion and ingestion velocity are reasonably matched and profile skewness is visible in the modeled profile.

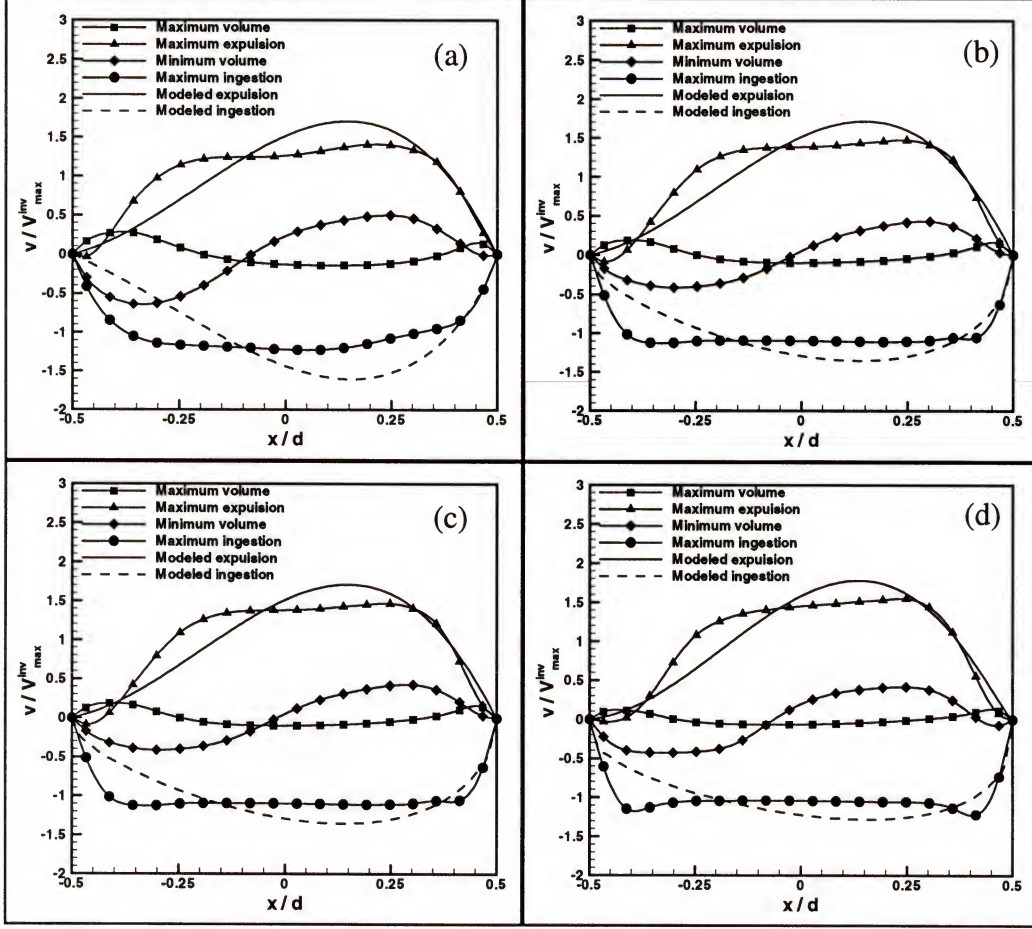


Figure 49. Comparison of actual and modeled profiles for  $h/d = 1$ ,  $\delta/d = 2$ ,  $Re_\delta = 254$ .  
a)  $Re_d = 63$ ; b)  $Re_d = 125$ ; c)  $Re_d = 187$ ; d)  $Re_d = 250$ .

In the final comparison, we look at higher external crossflow cases and these are shown in Figure 50 for  $Re_\delta = 400, 800, 1200$  and  $2600$ . Interestingly it is observed that with increasing external flow Reynolds number, even though the jet profile becomes more complex the modeled profile in fact matches even better (at least visually) to the actual profile than it did so for the quiescent flow cases. In particular, the peak expulsion and ingestion velocities match quite well and the skewness in the profile is also well

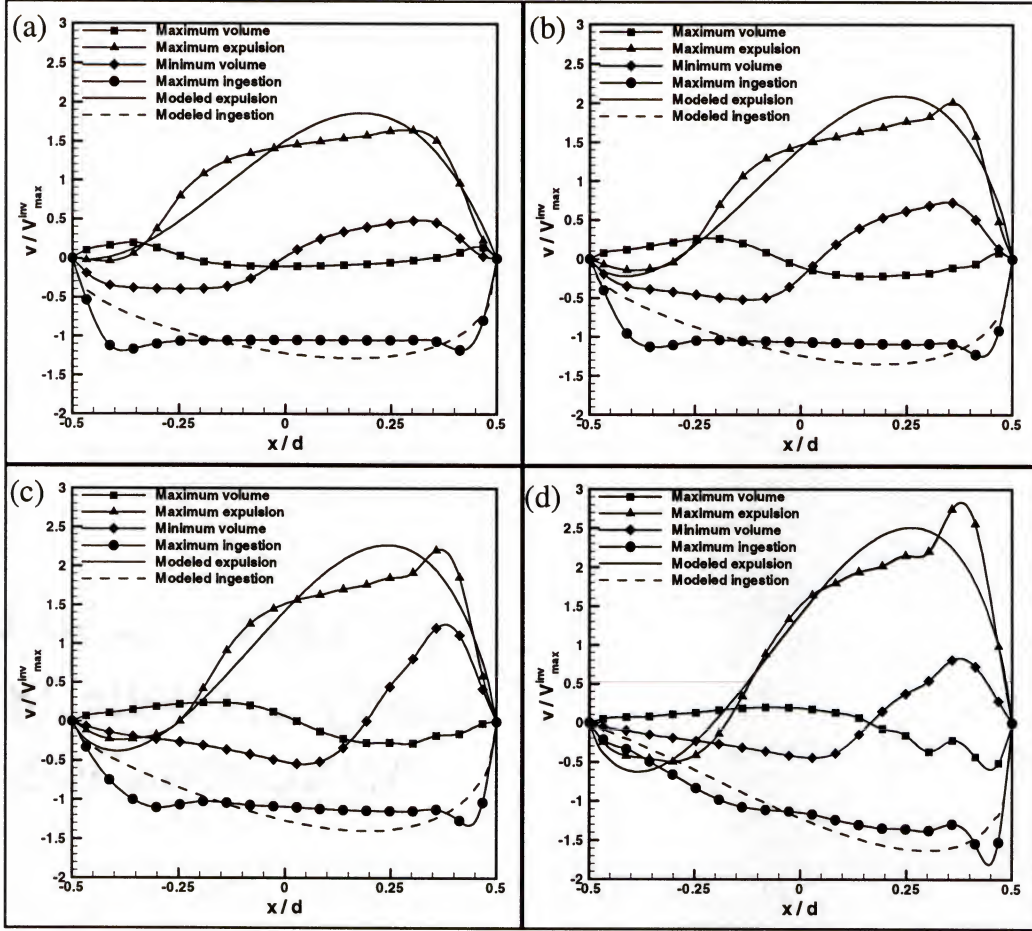


Figure 50. Comparison of actual and modeled profiles for  $h/d = 1$ ,  $\delta/d = 2$ ,  $Re_d = 250$ .  
a)  $Re_\delta = 400$ ; b)  $Re_\delta = 800$ ; c)  $Re_\delta = 1200$ ; d)  $Re_\delta = 2600$ .

represented. Furthermore, the counter flow observed near the left wall, in the actual jet at maximum expulsion is in fact also reproduced quite well in the modeled profile. This probably is due to the fact that as external flow Reynolds number increase the maximum expulsion profile transitions from two maxima (double-lobed) to one maximum and one minimum. The modeled profile is not capable of producing two maxima but can produce one maximum and one minimum. Thus, the chosen candidate profile is topologically better suited to representing higher  $Re_\delta$  cases. Since in separation control application,  $Re_\delta$  is expected to be in the  $10^2$  to  $10^4$  range, it is expected that the chosen profile will

be a viable candidate for modeling the synthetic jet profile. It remains to be seen how well these modeled profile reproduce the dynamics in the external flow. This can be examined by simulating the external flow with the modeled profile as an imposed boundary condition and comparing the external flow characteristics to the actual case with synthetic jet.



## CHAPTER 6

### VIRTUAL AERO-SHAPING EFFECT

Some previous studies (Amitay et al. 1997, Chatlynne et al., 2001) have hypothesized that a synthetic jet is capable of altering the effective shape of a body by forming a mean recirculation zone in the external flow that is significantly larger than the size of the jet. However, no direct support for this hypothesis has been provided in experiments or simulations. Here, this issue is explored by examining the mean flow characteristics of the flow created by the jet. The objective here is to develop some insight into the scaling of this effect vs. flow parameters.

In this study, we take the viewpoint that, in addition to the external flow parameters, the size of the recirculation bubble depends only on the basic characteristics of the jet expulsion profile and not on the details of the flow inside the cavity or of the flow as it travels through the slot. This can be expressed mathematically as

$$\frac{L_r}{d} = fn\left(C_{\text{exp}}^n, S, \text{Re}_\delta, \frac{\delta}{d}\right) \quad (33)$$

If we make a further assumption that the recirculation bubble does not depend strongly on the shape of the jet profile, then, an alternative and simpler scaling law can be used which is of the form

$$\frac{L_r}{d} = fn\left(\frac{V_{\text{inv}}^{\text{ave}}}{U_\infty}, S, \text{Re}_\delta, \frac{\delta}{d}\right) \quad (34)$$

Note that  $V_{\text{ave}}^{\text{inv}}/U_\infty \equiv C_{\text{ex}}^1$  if  $U_\infty$  is used in normalizing the jet velocity. This expression

forms a useful backdrop for the rest of the study.

In this study, the virtual aero-shaping effect will be examined from two different viewpoints, which are practically relevant. First, consider the case where a synthetic jet is mounted on a surface on which develops a boundary layer. The synthetic jet is operated with fixed diaphragm amplitude and frequency and we wish to explore how the virtual aero-shaping effect is modulated as the velocity of the external cross flow is increased. Second, consider the case where the external flow is fixed and the objective is to examine the influence of jet characteristic (e.g., amplitude, slot width) on the virtual aero-shaping effect. It is hoped that by considering both viewpoints, we will be able to develop useful insight into the dynamic scaling of this effect.

### 6.1 Effect of Variation in Crossflow Velocity

In Figure 51, we compare the mean streamline pattern for five cases corresponding to  $Re_\delta = 254, 400, 800, 1200$  and  $2600$  with  $A/H = 0.1$ . Note that as  $U_\infty$  is increased with  $A/H$  held constant, both  $Re_\delta$  and  $V_{ave}^{inv}/U_\infty$  change. Thus in the context of the above scaling expression (Equation 34), two of the parameters on the RHS change simultaneously. From Figure 51(a), we see that the high velocity jet creates a large system of recirculation bubbles on the surface of the flat plate with a length that is roughly  $13d$  and then reduce to  $6d$  for the  $Re_\delta = 400$  case. For the lower velocity jets (Figure 51(d) & (e)), no recirculation zones are formed and the streamlines are just slightly perturbed only in the very near vicinity of jet exit. Thus, the synthetic jet is indeed capable of forming large mean recirculation zones. However, this capability depends on the ratio of the jet to external flow velocity. For  $Re_\delta = 254$ ,  $V_{ave}^{inv}/U_\infty = 2.0$

whereas for  $Re_\delta = 1200$  and  $2600$ , this ratio is equal to  $0.42$  and  $0.19$  respectively. Thus, a large mean recirculation bubble forms only if the jet velocity is significantly higher than the external crossflow velocity.

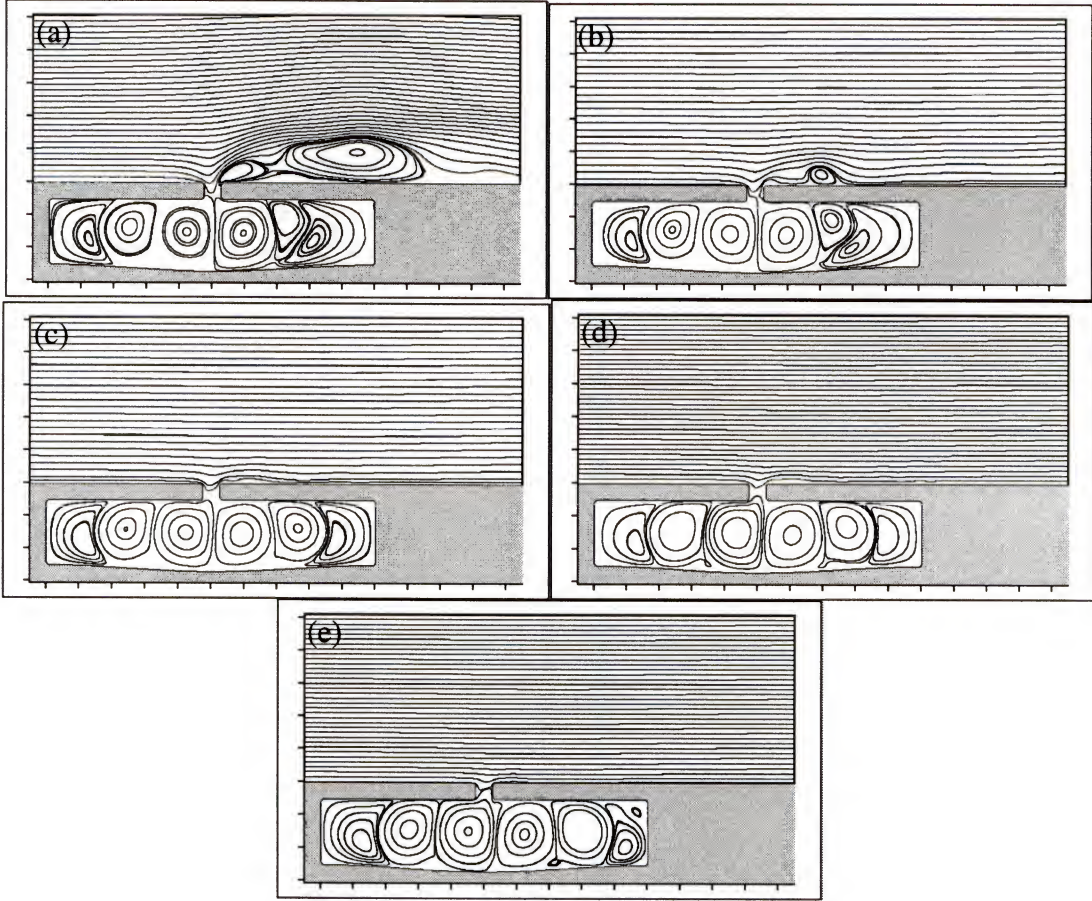


Figure 51. Streamline of the mean flow with  $\delta/d = 2$  and  $Re_d = 250$ . a)  $Re_\delta = 254$ ; (b)  $Re_\delta = 400$ ; c)  $Re_\delta = 800$ ; d)  $Re_\delta = 1200$ ; e)  $Re_\delta = 2600$ . Tick marks on x and y-axis are spaced a distance  $\delta$  apart.

## 6.2 Effect of Variation in Jet Velocity

In this series of simulations,  $\delta/d$ ,  $Re_\delta$  and  $S$  are fixed to  $2$ ,  $254$ , and  $10$  respectively and only  $V_{ave}^{inv}/U_\infty$  is varied by changing the amplitude of the diaphragm.

Figure 52 shows streamline of the mean flow for these cases. It is found that at low  $Re_d$



of 63 and 125, which correspond to  $V_{ave}^{inv}/U_{\infty}$  values of 0.5 and 1.0 respectively, the mean recirculation bubble is barely noticeable. However, as the relative jet velocity is increased, the large recirculation bubbles are observed in the mean flow. These recirculation zones are not simple but contain two recirculation regions, one of which is at the lip of the slot and one further downstream. For the highest jet Reynolds number case, the length of the recirculation region is estimated to be equal to  $13d$  or  $6.5\delta$ .

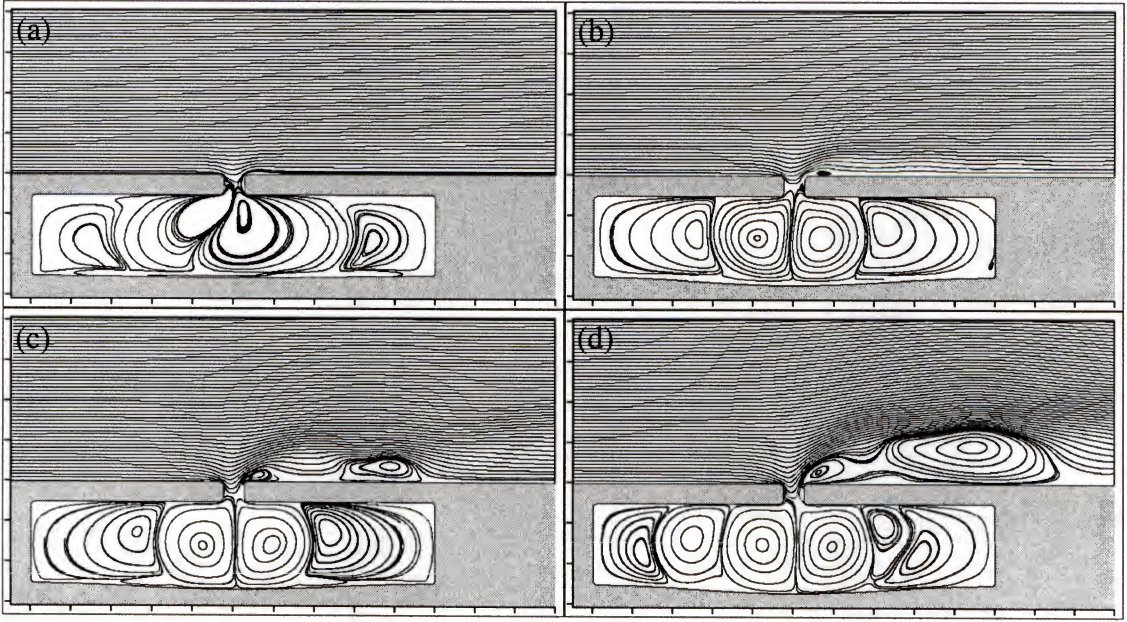


Figure 52. Streamline of the mean flow with  $\delta/d = 2$  and  $Re_{\delta} = 254$ . a)  $Re_d = 63$ ; b)  $Re_d = 125$ ; c)  $Re_d = 187$ ; d)  $Re_d = 250$ .

The same series of calculations have been repeated with  $\delta/d = 5$  since it was believed that the virtual aero-shaping effect might also depend on this parameter. Note that changes in  $\delta/d$  can be achieved by changing  $\delta$  and  $A$  (diaphragm amplitude) simultaneously while still matching  $Re_{\delta}$  and  $Re_d$ . Figure 53 shows the mean streamline pattern for the various cases with  $\delta/d = 5$ . For these cases too, it is found that large mean recirculation zones are formed where the jet velocity relative to external flow



velocity is high. In comparison to the previous  $\delta/d = 2$  case, here we find that for  $Re_d = 250$  case, the length of the recirculation region is about  $35d$  or  $7\delta$ .

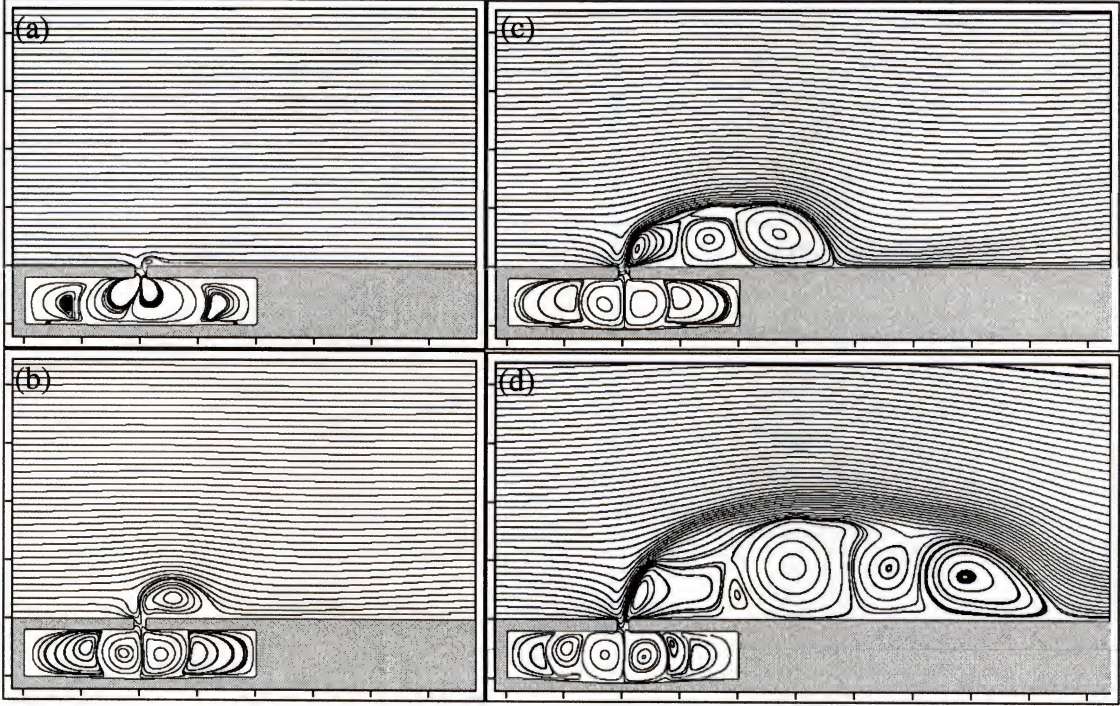


Figure 53. Streamline of the mean flow with  $\delta/d = 5$  and  $Re_\delta = 254$ . a)  $Re_d = 63$ ; b)  $Re_d = 125$ ; c)  $Re_d = 187$ ; d)  $Re_d = 250$ .

### 6.3 Scaling of the Bubble Size with Flow Parameters

Noticing the similarity in the size of the recirculation region relative to the boundary layer thickness for the two sets of cases it was decided to explore the scaling of the bubble length normalized by  $\delta$  with the parameter  $V_{ave}^{inv} d / U_\infty \delta$ , which represents a ratio of jet boundary layer volume flux. In the previous section, it was seen that the recirculation bubble of the last case (Figure 53(d)) is large compared to the distance between the left boundary and the slot. In order to ensure that the upstream length does not affect the size of the recirculation bubble, another simulation was run with the same parameters used in that case except that the domain size in the x-direction was expanded

to have an upstream length of about  $10\delta$ . The result of this case is referred to as Case 21 (wide) in Table 1 & Table 2. This case is also shown in Figure 54 & Figure 55 with the circle symbol. Figure 54 shows a log-log plot of  $L_r/\delta$  versus  $V_{ave}^{inv}d/U_\infty\delta$  where data points from eight different cases are plotted. A least square fit line through the data indicates a line with a slope of 2.09

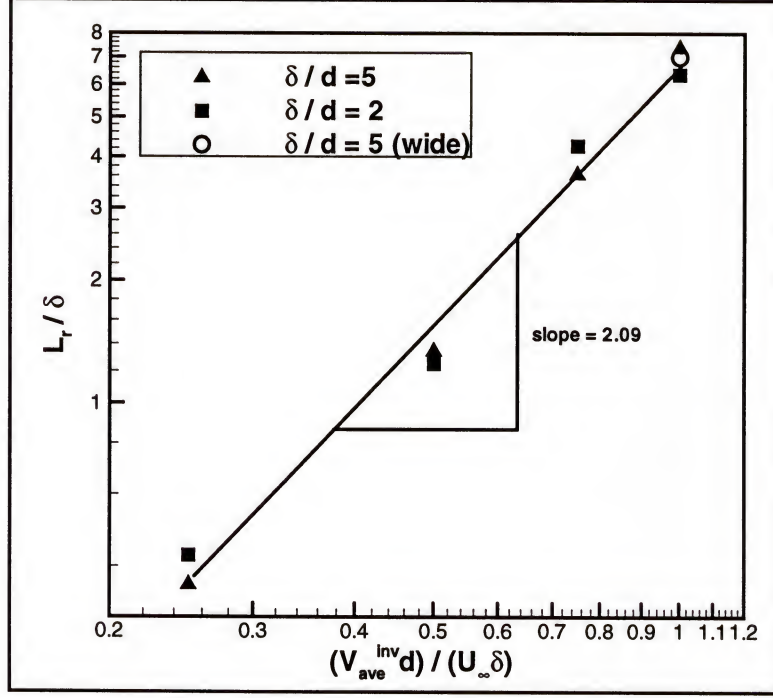


Figure 54. Log scale plot of the ratio  $L_r/\delta$  with the ratio  $V_{ave}^{inv}d/U_\infty\delta$ .

If we assume that this is an indication of a quadratic scaling, that implies that

$$\frac{L_r}{\delta} \propto \left( \frac{V_{ave}^{inv}d}{U_\infty\delta} \right)^2$$

This expression can be rearranged as

$$\frac{L_r}{d} \propto \frac{(V_{ave}^{inv})^2 d}{U_\infty^2 \delta}$$

where the right hand side can be identified as the ratio of jet expulsion to external



boundary layer momentum flux. In Figure 55, the data were replotted on a log-log scale with  $L_r/d$  versus  $(\bar{V}_{ave}^{inv})^2 d/U_\infty^2 \delta$  and the best-fit line has a slope of 1.03 which confirms the linear relationship between  $L_r/d$  and  $(\bar{V}_{ave}^{inv})^2 d/U_\infty^2 \delta$ . Even though a derivation of either of the above scaling from *a-priori* consideration of the dynamics of the flow has not been accomplished, the second scaling is physically more appealing due to the simple and direct involvement of the momentum flux, which is an important and readily identifiable property of the jet. Thus put in words, our simulations indicate that the length of the recirculation zone relative to the slot size is directly proportional to the ratio of jet to external boundary layer momentum flux.

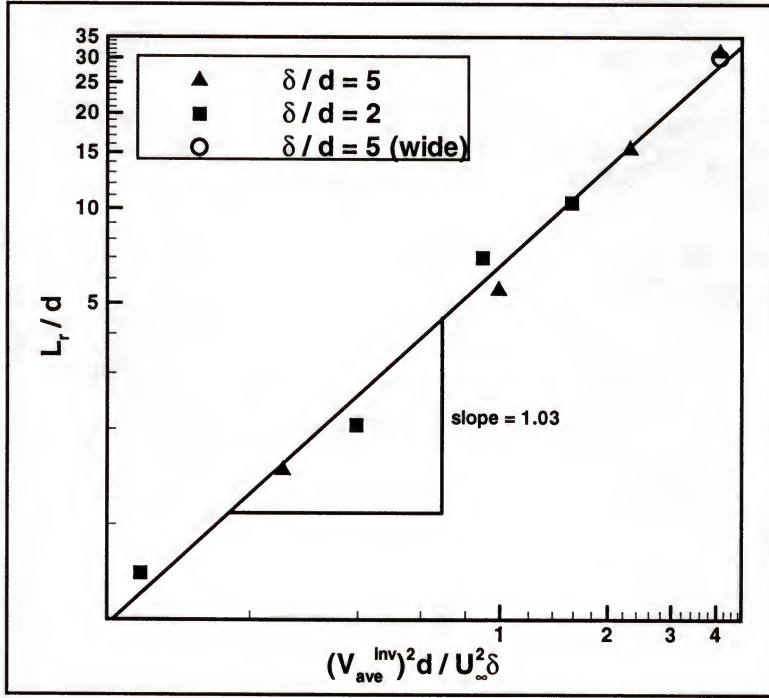


Figure 55. Log scale plot of the ratio  $L_r/d$  with the ratio  $(\bar{V}_{ave}^{inv})^2 d / U_\infty^2 \delta$ .

## CHAPTER 7

### CONCLUSIONS

Numerical simulations have been used to study the interaction of a synthetic jet with a flat plate laminar Blasius boundary layer in a simple, two-dimensional jet configuration. The diaphragm is modeled in a realistic manner as a moving boundary in an effort to compute the internal cavity flow accurately. Flows inside and outside the cavity of the synthetic jet actuator, with and without the presence of the external crossflow, are examined and the following key conclusions have been made:

- A comparison of the various cases indicates that the flow with and without an external crossflow is significantly different. The jet in quiescent external flow is dominated by vortex dipoles that are discharged from the jet slot. Although a firm criterion for the formation of this dipole jet has not been established, it is hypothesized that formation might be governed by the parameter  $(Re_d / S^2)$ .
- A wide range of vortex dynamics is observed in the cases where there is an external cross flow. Cross pairing of vortices from different cycles is observed in a number of cases along with multiple vortex formation due to inherent instability of the shear layer emanating from the slot.
- A systematic framework has been put forth for characterizing the jet in terms of the moments of the jet profiles and an integral measure of the profile skewness. This framework is used in examining the scaling of the jet performance over a wide range of parameters. Furthermore, a separate analysis of the ingestion and expulsion phases of the jet is found useful in that it clearly demonstrated the different behavior of the jet profile in these two phases.
- A simple, low-dimensional model for the jet is proposed and tested. The model allows for matching of three parameters each for the ingestion and expulsion phases. In the current study, we match the average inviscid jet velocity, momentum coefficient and skewness of the actual profile obtained from the simulations. The comparison indicates that the model allows for a reasonable match with the actual profile for the quiescent external flow cases, whereas the match is much better for jets in high-speed external crossflow.

- The so-called virtual aero-shaping effect of the synthetic jet is investigated. It is found that large mean recirculation bubbles are formed in the external boundary layer only if the jet velocity is significantly higher than the crossflow velocity. Furthermore, a simple scaling between the bubble size and the ratio of jet to external flow momentum is suggested.

Although the two-dimensional actuator used in the current study is not physically realizable, the current study is useful in that it sets a baseline for future simulations of a more realistic three-dimensional synthetic jet model. It is also expected that many of the broad conclusions reached here for the 2-D configuration will also apply to the three-dimensional configuration.

Finally, as a continuation of the current study we suggest the following:

- Examination of the vortex dipole jet formation criterion hypothesized in the current study.
- Reevaluation of the scaling of the jet characteristics in a more realistic 3-D jet configuration.
- Further testing of the proposed low-dimensional jet model to examine the fidelity with which a simulation with a modeled profile reproduces the external flow characteristics observed in a simulation with the actual jet.



## LIST OF REFERENCES

- Alcouffe, R. E., Brandt, A., Dendy, J. E., and Painter, J. W. 1981. The Multi-grid Method for the Diffusion Equation with Strongly Discontinuous Coefficients. *SIAM J. Sci. Stat. Comput.* Vol. 2, No. 4, pp. 430-454.
- Amitay, M., Honohan, A., Trautman, M., and Glezer, A. 1997. A Modification of the Aerodynamic Characteristic of Bluff Bodies Using Fluidic Actuators. *AIAA 97-2004*.
- Amitay, M., Kibens, V., Parekh, D., and Glezer, A. 1999. The Dynamics of Flow Reattachment over a Thick Airfoil Controlled by Synthetic Jet Actuators. *AIAA 99-1001*.
- Bayyuk, S. A., Powell, K. G., and van Leer, B. 1993. A Simulation Technique for 2-D Unsteady Inviscid Flows around Arbitrarily Moving and Deforming Bodies of Arbitrary Geometry. *AIAA 93-3391*.
- Beyer, R. P. and Leveque, R. J. 1992. Analysis of a One-dimensional Model for the Immersed Boundary Method. *SUAM J. Num Anal.* Vol. 29, pp. 332-364.
- Braza, M., Chassiang, P., and Ha Minh, H. 1986. Numerical Study and Physical Analysis of the Pressure and Velocity Fields in the Near Wake of a Circular Cylinder. *Journal of Fluid Mechanics.* Vol. 165, pp. 79-130.
- Buckingham, E. 1915. Model Experiments and the Form of Empirical Equations. *Transactions of the ASME.* Vol. 37, pp. 263.
- Chatlynne, E., Rumigny, N., Amitay, M., and Glezer, A. 2001. Virtual Aero-Shaping of a Clark-Y Airfoil Using Synthetic Jet Actuators. *AIAA 2001-0732*.
- Chen, Y., Liang, S., Aung, K., Glezer, A., and Jagoda, J. 1999. Enhanced Mixing in a Simulated Combustor Using Synthetic Jet Actuators. *AIAA 99-0449*.
- Chorin, A. J. 1968. Numerical Solution of the Navier-Stokes Equations. *Math. Comput.* Vol. 22, 745.
- Crook, A., Sadri, A. M., and Wood, N. J. 1999. The Development and Implementation of Synthetic Jets for the Control of Separated Flow. *AIAA 99-3176*.

- Davis, S. A. and Glezer, A. 1999. Mixing Control of Fuel Jets Using Synthetic Jet Technology: Velocity Field Measurement. *AIAA 99-0447*.
- Ferziger, J. H. and Peric, M. 1996. *Computational Methods for Fluid Dynamics*. Springer-Verlag. Berlin, Germany.
- Gad-el-Hak, M. and Bushnell, D. M. 1991. Separation Control: Review. *Journal of Fluids Engineering*. Vol. 113, pp. 5-30
- Griffin, O. M. and Hall, M. S. 1995. Vortex Shedding Lock-on in a Circular Cylinder Wake. *Flow-induced Vibration*. Balkeman, Rotterdam.
- Ho, C. H. and Tai, Y. C. 1996. Review: MEMS and Its Application for Flow Control. *Journal of Fluids Engineering*. Vol. 118.
- Hou, T. Y., Li, Z., Osher, S., and Zhao, H. 1997. A Hybrid Method for Moving Interface Problems with Application to the Hele-Shaw Flow. *J. Comp. Phys.* Vol. 134, No.2, pp. 236-247.
- Hsiao, F. B., Liu, C. F., and Shyu, J. Y. 1990. Control of Wall-Separated Flow by Internale Acoustic Excitations. *AIAA Journal*. Vol. 28(8), pp. 1440-1446.
- Huang, L. S., and Maestrello, L. 1987. Separation Control over an Airfoil at High Angles of Attack by Sound Emanating from the Surface. *AIAA 87-1261*.
- James, R. D., Jacobs, J. W., and Glezer, A. 1994. Experimental Investigation of a Turbulent Jet Produced by an Oscillating Surface Actuator. *Appl Mech Rev.* Vol. 47, No. 6.
- James, R. D., Jacobs, J. W., and Glezer, A. 1996. A Round Turbulent Jet Produced by an Oscillating Diaphragm. *Phys. Fluids*. Vol. 8, No. 9.
- Jayaraman, V., Udaykumar, H. S., and W. Shyy. 1997. Adaptive Unstructured Grid for Three-dimensional Interface Representation. *Numerical Heat Transfer B*. Vol. 32, No. 3, pp. 247-265.
- Khanna, A. 2000. Three-dimensional Representation of Evolving Interfaces in Computational Fluid Dynamics. MS Thesis, University of Florida, Gainesville, FL.
- Koopmann, G. H. 1967. The Vortex Wakes of Vibrating Cylinders at low Reynolds Numbers. *Journal of Fluid Mechanics*. Vol. 28(3), pp. 501-512.
- Kral, L. D., Donovan, J. F., Cain, A. B., and Cary, A. W. 1997. Numerical Simulation of Synthetic Jet Actuators. *AIAA 97-1824*.



- Lee, C. Y. and Goldstein, D.B. 2001. DNS of Microjets for Turbulent Boundary Layer Control. *AIAA* 2001-1013.
- Leveque, R. J. and Li, Z. 1994. The Immersed Interface Method for Elliptic Equations with Discontinuous Coefficients and Singular Sources. *SIAM J. Numer. Anal.* Vol. 31, No. 4, pp. 1019-1044.
- Meningini, J. R. and Bearman, P. W. 1993. Numerical Simulation of High Amplitude Oscillatory Flow About a Circular Cylinder Using the Discrete Vortex Method. *AIAA Shear Flow Conf. Paper AIAA 93-3288*.
- Mittal, R. and Balachandar, S. 1996. Direct Numerical Simulation of Flow Past Elliptic Cylinders. *J. Comput. Phys.* Vol. 124, pp. 351-367.
- Mittal, S. and Kumar, V. 1999. Finite Element Study of Vortex-induced Cross-flow and In-line Oscillations of a Circular at Low Reynolds Numbers. *International Journal for Numerical Methods in Fluids*. Vol. 31, pp. 1087-1120.
- Moretti, P. M. 1993. Flow-Induced Vibrations in Arrays of Cylinders. *Ann. Rev. Fluid Mech.* Vol. 25, pp. 99-114.
- Rhie, C. M. and Chow, W. L. 1983. Numerical Study of the Turbulent Flow Past an Airfoil with Trailing Edge Separation. *AIAA J.* Vol. 21(11), 1525.
- Rizzetta, D. P., Visbal, M. R., and Stanek, M. J. 1998. Numerical Investigation of Synthetic Jet Flowfields. *AIAA 98-2910*.
- Schlichting, H. and Gersten, K. 1996. *Boundary Layer Theory*. Springer. New York.
- Seifert, A., Bachar, T., Koss, D., Shepselovich, M., and Wygnanski, I. 1993. Oscillatory Blowing: A Tool to delay Boundary-Layer Separation. *AIAA Journal*. Vol. 31, No. 11.
- Seifert, A., Bachar, T., and Wygnanski, I. 1998a. Application of Active Separation Control to a Small Unmanned Air Vehicle. *Journal of Aircraft*. Vol. 36, No. 2.
- Seifert, A., Darabi, A., and Wygnanski, I. 1996. Delay of Airfoil Stall by Periodic Excitation. *Journal of Aircraft*. Vol. 33, No. 4.
- Seifert, A., Eliahu, S., and Greenblatt, D. 1998b. Use of Piezoelectric Actuators for Airfoil Separation Control. *AIAA Journal*. Vol. 36, No. 8.
- Seifert, A. and Pack, L. G. 1999. Oscillatory Control of Separation at High Reynolds Numbers. *AIAA Journal*. Vol. 37, No. 9.



- Smith, B.L. and Glezer, A. 1997. Vectoring and Small-scale Motions Effected in Free Shear Flows Using Synthetic Jet Actuators. *AIAA 97-0213*.
- Smith, B. L., Trautman, M. A., and Glezer, A. 1999a. Controlled Interactions of Adjacent Synthetic Jets. *AIAA 99-0669*.
- Smith, D., Amitay, M., Kibens, V., Parekh, D., and Glezer, A. 1998. Modification of Lifting Body Aerodynamics Using Synthetic Jet Actuators. *AIAA 98-0209*.
- Smith, D. R., Kibens, V., Pitt, D. M., and Hopkins, M. A. 1999b. Effect of Synthetic Jet Arrays on Boundary Layer Control. *SPIE*. Vol. 3674.
- Stansby, P. K. 1976. The Locking-on of Vortex Shedding due to the Cross-Stream Vibration of Circular Cylinders in Uniform and Shear Flows. *Journal of Fluid Mechanics*. Vol. 74, pp. 641-665.
- Temam, R. 1991. Remarks on the Pressure Boundary Condition for the Projection Method. *Theor. Comput. Fluid Dyn.* Vol. 3, pp. 181-184.
- Tu, C. and Peskin, C. S. 1992. Stability and Instability in the Computation of Flows with Moving Immersed Boundaries: A Comparison of Three Methods. *SIAM J. Sci. Stat. Comput.* Vol. 13, pp. 1361.
- Udaykumar, H. S., Mittal, R., and Rampunggoon, P. 2000. Simulation of Solid-Fluid Interactions on Cartesian Grids. *Proc. of 2000 ASME Winter Annual Meeting*.
- Udaykumar, H. S., Mittal, R., and Shyy, W. 1999. Solid-Liquid Phase Front Computations in the Sharp Interface Limit on Fixed Grids. *J. Comput. Phys.* Vol. 18, pp. 535-574.
- Wesseling, P. 1992. *Introduction to Multigrid Methods*. John Wiley & Sons, New York.
- Williams, D., Acharya, M., and Yang, B.P. 1991. The Mechanism of Flow Control on a Cylinder with the Unsteady Bleed Technique. *AIAA 91-0039*.
- Williamson, C. H. K. 1996. Vortex Dynamics in the Cylinder Wake. *Ann. Rev. Fluid Mech.* Vol. 28, 479-539.
- Wood, N. B. 1999. Aspect of Fluid Dynamics Applied to the Larger Arteries. *J. Theor. Biol.* Vol. 199, pp. 137-161.
- Ye, T., Mittal, R., Udaykumar, H. S., and Shyy, W. 1999. An Accurate Cartesian Grid Method for Viscous Incompressible Flows with Complex Immersed Boundaries, *J. Comp. Phys.* Vol. 156, pp. 209-240.


Zang, Y., Street, R. L., and Koseff, J. R. 1994. A Non-staggered Grid, Fractional Step Method for Time-dependent Incompressible Navier-Stokes Equations in Curvilinear Coordinates. *J. Comput. Phys.* Vol. 114, 18.

## BIOGRAPHICAL SKETCH

Prakit Rampunggoon graduated from the Royal Thai Naval Academy, Thailand, with a Bachelor's degree in Marine Engineering in 1995. After graduation, he worked as an engineering officer in the Royal Thai Navy for 1 year. In 1996, he was granted a scholarship to study in the United States. He completed his Master's degree in Mechanical Engineering from the University of Michigan in 1998. In August 1998, he enrolled in a PhD. program in Mechanical Engineering at the University of Florida. He expects to graduate in December 2001 and resume his work in the Royal Thai Navy.



I certify that I have read this study and that in my opinion it conforms to acceptable standards of scholarly presentation and is fully adequate, in scope and quality, as a dissertation for the degree of Doctor of Philosophy.



---

Rajat Mittal, Chairman  
Assistant Professor of Mechanical  
Engineering

I certify that I have read this study and that in my opinion it conforms to acceptable standards of scholarly presentation and is fully adequate, in scope and quality, as a dissertation for the degree of Doctor of Philosophy.



---

William E. Lear, Jr.  
Associate Professor of Mechanical  
Engineering

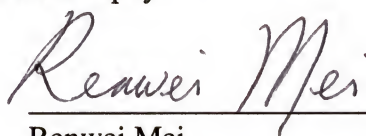
I certify that I have read this study and that in my opinion it conforms to acceptable standards of scholarly presentation and is fully adequate, in scope and quality, as a dissertation for the degree of Doctor of Philosophy.



---

Zhuomin Zhang  
Associate Professor of Mechanical  
Engineering

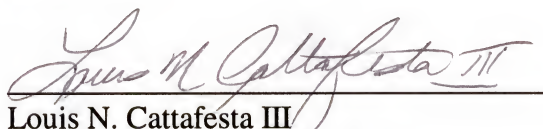
I certify that I have read this study and that in my opinion it conforms to acceptable standards of scholarly presentation and is fully adequate, in scope and quality, as a dissertation for the degree of Doctor of Philosophy.



---

Renwei Mei  
Professor of Aerospace Engineering,  
Mechanics & Engineering Science

I certify that I have read this study and that in my opinion it conforms to acceptable standards of scholarly presentation and is fully adequate, in scope and quality, as a dissertation for the degree of Doctor of Philosophy.





Louis N. Cattafesta III

Assistant Professor of Aerospace  
Engineering, Mechanics & Engineering  
Science

This dissertation was submitted to the Graduate Faculty of the College of Engineering and to the Graduate School and was accepted as partial fulfillment of the requirements for the degree of Doctor of Philosophy.

December 2001

  
Pramod P. Khargonekar  
Dean, College of Engineering  
Winfred M. Phillips  
Dean, Graduate School